Univerzita Karlova v Praze
Matematicko-fyzikální fakulta

DIPLOMOVÁ PRÁCE

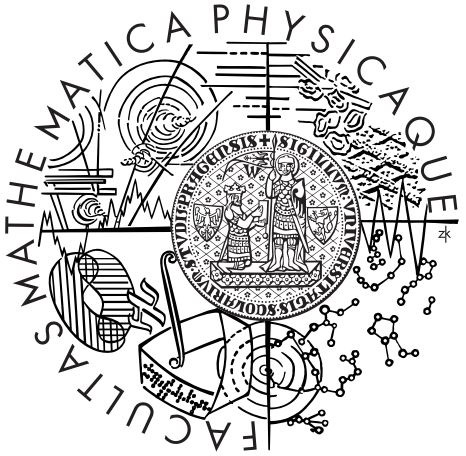

Veronika Klevarová

Materiály pro fúzní aplikace a jejich interakce s tokamakovým plazmatem

Katedra fyziky materálů

Vedoucí diplomové práce: doc. RNDr. Miloš Janeček, CSc.

Studijní program: Fyzika

Studijní obor: Fyzika kondenzovaných soustav a materiálů

Praha 2015

Charles University in Prague
Faculty of Mathematics and Physics

MASTER THESIS

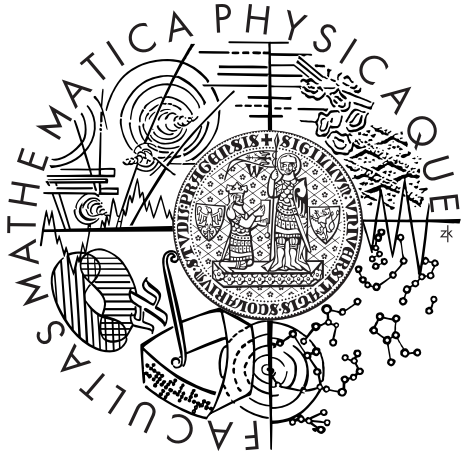

Veronika Klevarová

Materials for fusion applications and their interaction with tokamak plasma

Department of Physics of Materials

Supervisor of the master thesis: doc. RNDr. Miloš Janeček, CSc.
Study programme: Physics
Specialization: Physics of Condensed Matter and Materials

Prague 2015

Acknowledgements

Hereby I would like to express gratitude both to supervisor and consultant of my work, doc. RNDr. Miloš Janeček, CSc. and Ing. Jiří Matějíček, Ph.D., respectively, for their support and advice.

I would like to thank all colleagues from the distinct laboratories/departments for providing me with a necessary assistance during the collection of the experimental data. I am thankful for the advice and guidance in the subsequent data analysis that was provided to me, in case of need. Beside that, I would like to thank:
Ing. Zdeněk Dlabáček for preparation of the set of W-SPS and introduction to this fabrication technique;
Dr. rer. nat Marius Wirtz and his colleagues from Forschungszentrum Juelich to letting me participate on the exposure of W-SPS samples to combined plasma and transient-like heat loads and providing me with necessary information concerning the exposure;
doc. RNDr. Jan Mlynář, Ph.D., doc. RNDr. Miloš Janeček, CSc. and Ing. Jiří Matějíček, Ph.D. for supporting my stay at Forschungszentrum Juelich during the samples exposure;
Marta Čepová that helped me with the optical metallography and measurement of Vickers microhardness of the irradiated samples;
RNDr. Petr Harcuba for introducing me to EBSD measurements, and providing me with advice important in the subsequent analysis;
Mgr. Jozef Veselý, Ph.D. for giving me an introduction to AFM and providing me important literature for the further analysis of the experimental results;
Martin Husák for preparation of samples for cross-sectional metallography;
RNDr. František Lukáč for performineg the XRD measurements and analysis;
Ing. Leoš Polívka for performing the FIB analysis and introducing me to this experimental technique;
Ing. Pavel Psota for providing me the introduction to optical profilometry;
RNDr. Vladimír Havránek, CSc. and his colleagues for performing the ERDA measurements and introducing me to the analysis of collected data;
Mgr. Vladimír Weinzettl, Ph.D. for introduction to PSI experiments at COMPASS-D, proposing the topic to analyse and providing me with all necessary materials and advice;
M.S. Miglena Dimitrova, Ph.D. for providing me with outcomes of the measurements of divertor Langmuir probes installed at COMPASS-D.

Finally, I would like to thank my family for supporting me during the full period of my Master studies.

I declare that I carried out this master thesis independently, and only with the cited sources, literature and other professional sources.

I understand that my work relates to the rights and obligations under the Act No. 121/2000 Coll., the Copyright Act, as amended, in particular the fact that the Charles University in Prague has the right to conclude a license agreement on the use of this work as a school work pursuant to Section 60 paragraph 1 of the Copyright Act.

In Prague date ..... Veronika Klevarová .....

Název práce: Materiály pro fúzní aplikace a jejich interakce s tokamakovým plazmatem

Autor: Veronika Klevarová

Katedra: Katedra fyziky materiálů

Vedoucí diplomové práce: doc. RNDr. Miloš Janeček, CSc., Katedra fyziky materiálů

Abstrakt: Wolfram představuje perspektivní materiál pro aplikace v první stěně fúzních zařízení. V rámci první části této práce byla metodou spark plasma sintering připravena sada wolframových vzorků s proměnlivou velikostí zrna. Vzorky byly vystaveny simultánnímu ozáření deuteriovým plazmatem a vysokoenergetickými tepelnými toky. Tyto podmínky simulují běžný provoz tokamaku. V důsledku ozáření byly povrchy vzorků zdrsněny, původně připravená zrna byla zotavena a v některých případech byl povrch vzorků popraskán. Dále pak analýza poškozených vzorků poukázala na aktivaci skluzových systémů v rámci ozářených povrchů. Limitní velikost zrna pro aktivaci skluzu byla stanovena, při daných ozařovacích podmínkách, na $\sim 5.5 - 6.6$ μm. Nicméně spíše než velikost zrn, se ukázaly dùležité výrobní parametry vzorkù v kontextu interpretace poškození povrchů. Synergistické efekty simultánní expozice se projevily ve snížené tepelné vodivosti od povrchu vzorků směrem k jejich středu. V rámci úvodu druhé části této práce byly popsány experimenty zaměřené na studium interakce plazmatu s materiály v tokamaku COMPASS-D. Představeny byly výsledky prvních experimentů zaměřených na erozi testovaných vzorků. Nejednoznačná analýza spektroskopických dat naznačuje, že tepelné a částicové namáhání vzorků v tomto tokamaku pro účely studia eroze nejsou dostatečně vysoké.

Klíčová slova: termojaderná fúze, tokamak, materiály první stěny, spark plasma sintrování, eroze

Title: Materials for fusion applications and their interaction with tokamak plasma

Author: Veronika Klevarová

Department: Department of Physics of Materials

Supervisor: doc. RNDr. Miloš Janeček, CSc., Department of Physics of Materials

Abstract:

Tungsten represents a perspective option in the context of fusion devices first-wall materials. In the first part of this work, set of tungsten samples with variable grain size was prepared by spark plasma sintering. Specimens were exposed to steady state deuterium plasma beam and high energy heat pulses, simulating thus the normal operation in the tokamak. As a consequence of the exposure, samples surfaces were roughened, as-prepared grains were recovered and in some cases cracks were formed. Moreover, post-irradiation analysis of the damaged samples revealed activation of in-grain slip systems within the loaded surfaces. Threshold grain diameter for this mechanism was determined to be between $\sim 5.5-6.6$ μm at the particular loading conditions. However, damaged features showed to depend more on the fabrication parameters than on the grain diameter. Synergistic effects of simultaneous loading were proven to be important since those reduced the heat propagation within the volume of the tested samples. In the second part of this thesis, introduction to plasma-surface interaction studies at tokamak COMPASS-D was given, including the outcomes of the first erosive experiments. It was shown that erosion monitoring by spectroscopic means is ambiguous and ineffective due to rather low heat and particle fluxes causing only a slight erosion of the tested materials.

Keywords: thermonuclear fusion, tokamak, first wall materials, spark plasma sintering, erosion

Contents

List of Abbreviations

AFM	atomic force microscopy
APS	atmospheric plasma spraying
ASDEX	Axially Symmetric Divertor Experiment
BSE	back-scattered electrons
BT	base temperature
CB	cassette body
CCD	charge-coupled device
CFC	carbon fibre composite
CMSII	combined magnetron sputtering and ion implantation
COMPASS	COMPAct ASSembly
CVD	chemical vapour deposition
DBTT	ductile-to-brittle transition temperature
DPM CU	Department of Physics of Materials, Charles University
D-T	deuterium-tritium
EBSD	electron backscatter diffraction
ECCI	electron channelling contrast imaging
ECRH	electron cyclotron resonance heating
ERDA	elastic recoil detection analysis
FEG	field emission gun
FG	functionally graded
FIB	focused ion beam
FWHM	full width at half maximum
FZ-J	Forschungszentrum Juelich
GB	grain boundary
GDC	DC glow discharge
GIS	gas injection system
HFS	high-field side
HIP	hot isostatic pressing
HPPS	high pressure plasma spraying
HRP	hot radial pressing
ICRH	ion cyclotron resonance heating
IP CAS	Institute of Physics of the Czech Academy of Science
IPP CAS	Institute of Plasma Physics, Czech Academy of Science
ITER	Internation Thermonuclear Experimental Reactor
IVT	inner vertical target
IVVS	in vessel viewing system
JET	Joint European Torus
JT-60	Japan Torus
LDP	Langmuir double probe
LPPS	low pressure plasma spraying
K-HI	Kelvin-Helmholtz instabilities
NBI	neutral beam injection
NIC	Nomarski interference contrast
NPI CAS	Nuclear Physics Institute of Czech Academy of Science

OVT	outer vertical target
PFC	plasma facing component
PS	plasma spraying
PSI	plasma-surface interaction
RBS	Rutherford back-scattering
ROI	region of interest
RT	room temperature
SEM	scanning electron microscopy
SE	secondary electrons
SND	single null X-point
SPS	spark plasma sintering
TEAC	target exchange and analysis chamber
VPS	vacuum plasma spraying

1. Introduction

1.1 Basic principles of fusion

Constantly increasing global energy consumption per capita necessarily implies a higher demand for power supplies. Current estimations of the natural resources foresee depletion of sources of fuels in a relatively short time scale (of the order of tens to hundreds of years in case of the fossil fuels [1]). Since coal, oil and natural gas represent more than 80% of the worldwide primary energy supplies (Fig. 1.1), it is in a focus of current research to design large scale power plants whose fuel would be, in an ideal scenario, inexhaustible. Moreover, a public demand for environmentally acceptable design of power plant has raised during the last decades. Practically all current energy supplies face specific problems related to their service - as for example production of greenhouse gases, large surface land requirements for either growing the biofuels or construction of the solar panels/wind turbines or production of radioactive waste in case of the nuclear fission power plants. The latter also raises concerns regarding their safety operation.

All requirements - large scale energy supply with inexhaustible fuel source, environmentally-friendly concept and safe operation - might be fulfilled through achievement of *ignition* in a *thermonuclear fusion reactor*.

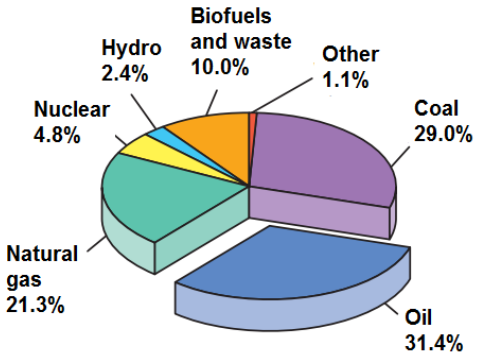

Figure 1.1: Total primary energy supplies, global percentage contribution in 2012 [2].

During the nuclear fusion nuclei merge together and form a heavier nucleus. Following the liquid drop model of nucleus, the energy needed to separate nucleus into the nucleons (the binding energy of a nucleus, B) can be calculated through the so called semi-empirical mass equation, whose formulation can be found for example in [3]. Particularly important is the dependence of binding energy per nucleon, B/A, as a function of the mass number of nucleus, A, that reaches its maximum for the element ^{62}Ni (Fig. 1.2). Since the sum of masses of protons and neutrons forming a nucleus does not equal its total mass, the mass defect, Δm, can be calculated as:

$$\Delta m = Z m_{proton} + (A - Z) m_{neutron} - m_{nucleus}, \tag{1.1}$$

where Z stands for the proton number of the isotope. Equally the Δm_{fusion}, mass defect between two reactants of fusion reaction of masses m_1 and m_2 and

the mass of the final product M, can be calculated:

$$\Delta m_{fusion} = m_1 + m_2 - M, \tag{1.2}$$

with $m_1 + m_2 > M$ implicating that Δm_{fusion} is positive. Using the Einstein's mass-energy equivalence formula, the energy released/supplied during the fusion reaction, ΔE_f, can be obtained:

$$\Delta E_f = \Delta m_{fusion} c^2, \tag{1.3}$$

In terms of the binding energies per nucleon, the nuclei of interest for the case of an exothermic fusion reaction are to be found at the Fig. 1.2, $A < 62$. As an example, the fusion reaction of two deuterium nuclei leading to formation of tritium and proton can be considered:

$$\mathrm{D} + \mathrm{D} \rightarrow \mathrm{T} + \mathrm{p} + \Delta \mathrm{E_f}.$$

Since $B/A_D \sim 1.1$ MeV and $B/A_T \sim 2.8$ MeV, the energy balance of this reaction can be estimated:

$$2 \cdot 1.1\,\mathrm{MeV} + 2 \cdot 1.1\,\mathrm{MeV} - 3 \cdot 2.8\,\mathrm{MeV} \sim -4\,\mathrm{MeV},$$

where the -4 MeV stands for a net energy gain from this particular reaction scenario.

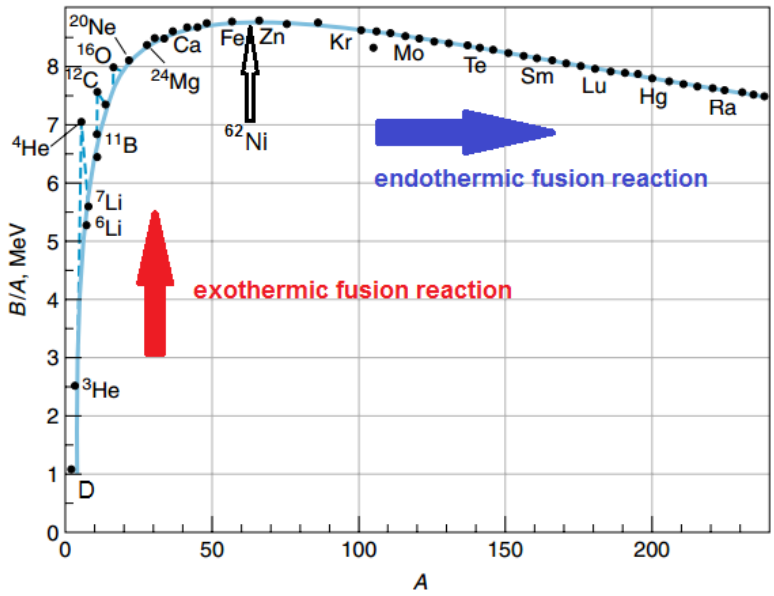

Figure 1.2: Binding energy per nucleon, B/A in MeV [3]. Depicted are the areas of exothermic/endothermic fusion reactions and the maximum of the curve at $A = 62$.

Reactions yielding the highest energy gain - those with significant difference between $B/A_{reactancts}$ and $B/A_{products}$ - are naturally in particular interest. Among favorable reactions, the fusion of deuterium and tritium has the highest estimated cross-section for a significant range of deuterium energies [4]. The reaction is described as follows:

$$\mathrm{D} + \mathrm{T} \rightarrow {}^{5}\mathrm{He}\,(17.59\,\mathrm{MeV}) \rightarrow {}^{4}\mathrm{He}\,(3.56\,\mathrm{MeV}) + \mathrm{n}\,(14.03\,\mathrm{MeV}). \tag{1.4}$$

The unstable intermediate product, ^{5}He, decays immediately into the final products of the reaction, an alpha particle and a neutron. Unlike the sources of deuterium, which are practically inexhaustible (since deuterium is naturally present in seawater), tritium supplies are scarce, and nowadays of the order of tens of kilograms. In practice, however, tritium can be produced within the fusion reactor itself, through the reactions:

$$\mathrm{n} + {}^6\mathrm{Li} \rightarrow {}^4\mathrm{He} + {}^3\mathrm{T} + 4.8\,\mathrm{MeV}, \tag{1.5}$$

$$\mathrm{n} + {}^7\mathrm{Li} \rightarrow {}^4\mathrm{He} + {}^3\mathrm{T} + \mathrm{n} - 2.5\,\mathrm{MeV}. \tag{1.6}$$

Lithium represents an element whose supplies might not be exhausted within several hundreds of years.

Regarding the environmental and safety eligibility of a potential fusion reactor, the advantages are self-evident:

- no greenhouse gases emission (Eq. 1.4),
- fusion is not a chain reaction, melt-down event is thus in principle impossible,
- final product of D-T reaction is not radioactive, since ^{4}He is a stable isotope,
- tritium, a radioactive element (through a beta decay with half-time of 12.32 years), will be kept in a closed circuit within the reactor in the amount not exceeding several kilograms.

During the life-time of the reactor, its walls will become activated under the impact of neutrons resulting from the D-T fusion. Nevertheless current material research for fusion applications is focused on development of low-level activated materials whose activity above hands-on level shall not exceed significantly hundred years.

In order to fuse two nuclei, the Coulomb repulsion that they mutually exert must be overcome by their high energy (temperature), under relevant collision conditions (density). Reactants are thus in a *plasma* state. John D. Lawson in 1955 formulated a criterion under which the ignition - independence of the process on external power supply - of the fusion reaction is achieved. For practical reasons it is usually stated as a triple product of plasma density, n, temperature, T and confinement time τ_E, the latter being defined as a measure of loss of energy of the system to 1/e of its initial value. For the D-T fusion reaction to ignite, the triple product must fulfil the following condition [5]:

$$nT\tau_E > 3 \cdot 10^{21}\,\mathrm{m}^{-3}\mathrm{keVs}. \tag{1.7}$$

1.2 Magnetic confinement - concept of tokamak

Typical order of magnitudes of the plasma parameters for a D-T reaction to ignite are $n \sim 10^{20}$ m^{-3} and $T \sim 10$ keV[1] . Such high temperatures require that the plasma is not in direct contact with walls of the thermonuclear fusion

[1] 1 eV = 11605 K

reactor. Since plasma consists of charged particles, these can be confined within the reactor vessel by the use of magnetic fields.

Nowadays the most promising design of such magnetically confining reactor is the *tokamak*, with its typical torus shape (Fig. 1.3). Charged particles are moving along the field lines whose configuration is given by a superposition of two independent components: coils surrounding vacuum vessel produce a toroidal magnetic field and the second component, poloidal, is produced by the plasma current. The latter is induced by a transformer, whose secondary winding is the plasma column. The resulting field lines are said to be helical. Plasma species can be heated through the ohmic heating, nevertheless resistivity of plasma decreases with increasing temperature as $T^{-3/2}$ and is thus ineffective at high temperatures. To bring the plasma to the temperatures required for the ignition, auxiliary heating systems must be used, such as heating through injection of neutral particles (neutral beam injection, NBI) or through interaction of plasma particles with the electromagnetic waves (at electron and ion cyclotron resonance frequencies, ECRH and ICRH, respectively) [7]. Under certain circumstances (typically at high temperatures), confined plasma can pass to a high confinement mode (H-mode), characterised by longer confinement time and steep gradients of plasma parameters such as pressure, density and temperature [8]. This particular operational mode has an important consequences on the heat and particle release from the plasma volume towards the reactor wall (see below). For more extensive description of the tokamak design see for example [9].

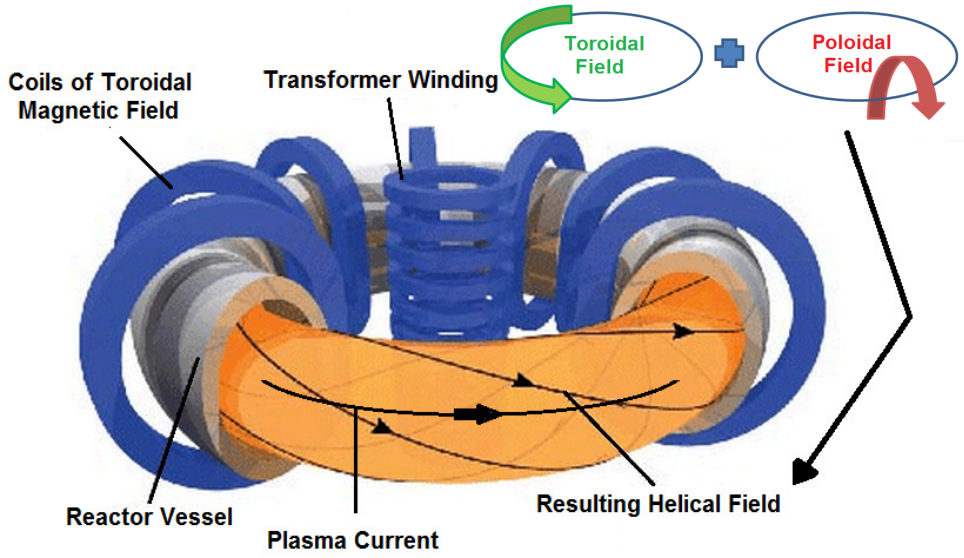

Figure 1.3: Schematic design of tokamak. Drawing at right upper corner shows a superposition of toroidal and poloidal magnetic fields [6].

An experimental tokamak reactor, largest of its kind, is currently under construction in Cadarache, France. This International Thermonuclear Experimental Reactor (ITER, Fig. 1.4) shall mainly demonstrate the possibility of achieving $Q = 10$, Q being defined as a ratio of produced fusion power to the power externally supplied to maintain the plasma in a steady state. Main parameters of ITER reactor are summarised and compared with values corresponding to the

largest tokamak in operation so far, JET (Joint European Torus), in Tab. 1.1. The full D-T campaign at ITER is foreseen to begin around 2026 [10].

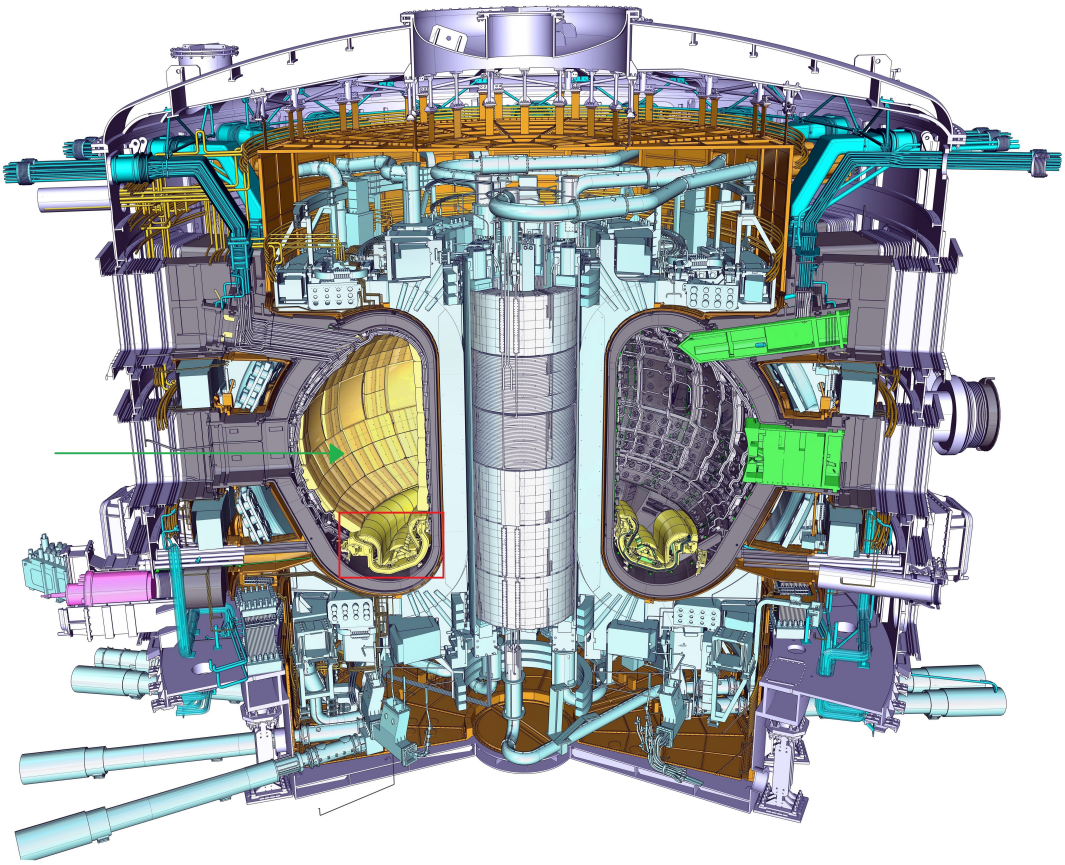

Figure 1.4: Schematic overview of ITER [11]. Region for the waste removal from the volume of the reactor, the so called divertor, is indicated by the red rectangle. Reactor's first wall is marked by the green arrow.

1.3 Plasma facing materials

Important part of the ongoing fusion research is focused on the selection of appropriate materials constituting the reactor. Those can be divided into three following categories:

- materials of the reactor first wall, directly facing the plasma,
- structural materials,
- functional materials (of electrical insulation etc.).

Materials studied in the scope of this work belong to the first category, the following discussion will therefore focus on the plasma facing components, PFCs.

1.3.1 Expected thermal loads

Components of the tokamak's first wall will be exposed to significant thermal and thermally induced mechanical loads during the operational lifetime of the reactor.

	JET	ITER
Total fusion power [MW]	~ 16	500
Plasma current [MA]	≤ 6	15
Pulse duration [s]	20-60	> 400
Toroidal magnetic field (at plasma axis) [T]	3.5	5.3
Plasma volume [m^3]	90	837
Plasma major/minor radius [m]	3.0/1.3-2.1	6.2/2.0
Q	0.65	10

Table 1.1: Main parameters of JET and ITER tokamaks [12, 13].

Beside the normal loading of the first wall and divertor plates (see Fig. 1.4 for their localisation in the reactor's vessel), off-normal events are expected to occur. Steady state heat loads are supposed to not to exceed $\sim 2 - 20$ MW/m^2 (or < 1 MW/m^2 in case of the first wall), while during the so called *transient* events the energy deposited on the PFCs can be of the order of tens of GW/m^2 (Fig. 1.5). Three different types of transient events can be distinguished [14, 15]:

- *Vertical Displacement Events, VDEs*, are caused by loss of the plasma control in the vertical direction. Consequently, plasma column can collide with the vessel wall, causing the plasma current to flow towards the PFCs. Typically, these events last for $0.1-1$ s and the energy deposited on the material is of the order of hundreds of MW/m^2. Elongated (or D-shaped) plasma configurations are more sensitive to VDEs. Such plasma shape is expected in ITER, and due to both high storage of the energy and relatively long duration of these events resulting in a severe PFCs damage, number of VDEs that can take place during the ITER's operation is strongly limited.

- *Disruptions* represent abrupt terminations of the plasma discharges, with the highest energy release towards the PFCs within $\sim 10^{-3} - 10^{-1}$ s. Disruptions can be caused by plasma instabilities that lead to modification of the plasma shape, alteration of the magnetic field configuration and finally loss of the plasma confinement.

- *Edge Localised Modes, ELMs*, are associated with the steep plasma pressure gradients, typical for tokamak operation in H-mode. Since ITER will operate mainly in the high confinement mode, ELMs shall be thus considered as normal events. It is assumed that the steep gradients might lead to formation of plasma edge instabilities, which are relaxed via partial particle and energy release through ELMs. These events occur regularly with typical frequency > 1 Hz.

In conclusion, materials constituting the PFCs must sustain during the required operational time both heat and particle loads originating from normal and off-normal events. Since tokamak represents a pulsed device, candidate plasma facing materials are standardly exposed to cyclic loading by heat fluxes in order to study their thermal fatigue. Typically, candidate divertor materials are

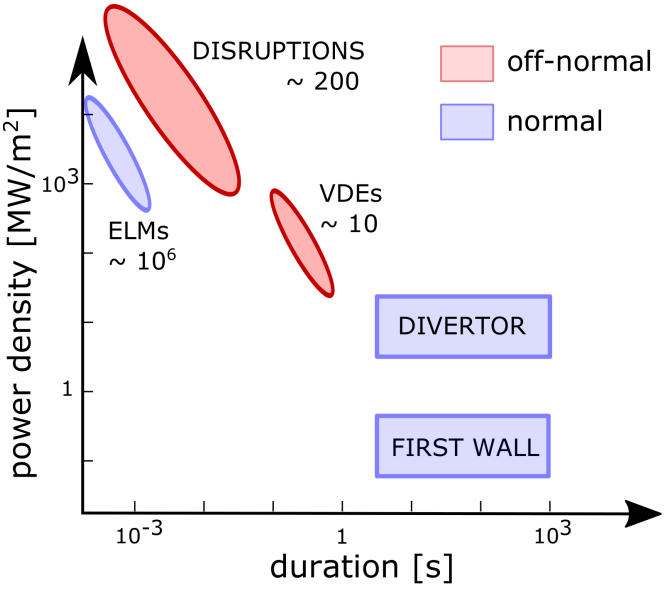

Figure 1.5: Typical order of magnitudes of power density deposited on PFCs during the various events in ITER [14]. Expected numbers of transient events are included in the graphic.

exposed to heat fluxes of magnitude ~ 10 MW/m^2, first wall materials to fluxes of < 1 MW/m^2. Under such conditions the performance under the normal operation is tested. Number of exposure cycles corresponds to the expected lifetime of the component (usually of the order of $10^3 - 10^4$ cycles) [16]. Loading conditions comparable to transient events can be simulated for example through sample exposure to high energy laser or electron beam pulses, with number of loading cycles ranging between $10^2 - 10^3$ [17].

1.3.2 Plasma-material interaction processes

Interaction of high energy plasma species with the plasma facing materials might lead to irreversible surface modifications (such as crack formation, melting, roughening) and other effects having as a consequence a deterioration of the plasma confinement. Typically, plasma interacts with the surrounding surfaces through the following processes:

- implantation of the impacting ions into the volume of the PFCs,
- erosion of the surface layers through particles impact, eroded material might be further re-deposited (or co-deposited, see Fig. 1.6) on the vessel wall,
- formation of alloys or chemical compounds with modified mechanical properties,
- mobilization of dust during the transient events,
- elastic or inelastic collisions with the high energy fusion products, namely neutrons, with the vessel materials, having as a consequence degradation of thermal and mechanical properties, and generation of new elements through transmutation.

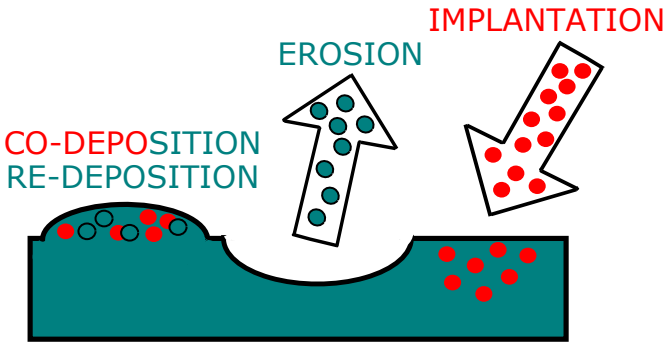

Figure 1.6: Illustration of plasma-material interaction processes, here depicted processes of implantation, material erosion, re-deposition and co-deposition.

1.3.3 Candidate materials

In general, the following requirements are applied to candidate plasma facing materials [14, 18]:

- low level of activation and high resistance against degradation under 14 MeV neutrons irradiation,
- high thermal conductivity,
- compatibility with plasma (and low plasma contamination),
- high melting/sublimation point,
- low fuel retention,
- good resistance against chemical and physical sputtering/erosion,
- appropriate mechanical properties (tolerance to high thermal loads, resistance to damages etc.),
- tolerable cost.

Regarding the resistance against sputtering, high-Z elements are typically preferred. On the other hand, atoms released from the PFCs dilute the plasma and might cause its cooling through enhanced bremsstrahlung. Tolerable concentration of impurities in this context increases with decreasing Z, therefore low-Z materials are desired. These contradicting requirements, together with other arguments, have lead to decision to cover distinct parts of ITER vacuum vessel by different materials. Lately, three materials have been considered and tested as possible PFC material for ITER: beryllium, carbon either in the composite form (CFC, carbon fibre composite) or in the form of fine grain graphite and tungsten.

Beryllium

This element has been chosen to cover the ITER's first wall (of surface $\sim 620\text{m}^2$) due to favourable combination of its properties. Firstly as a low-Z material ($Z = 4$) it does not cool plasma significantly through radiation when present in the

plasma. Beryllium has a good thermal conductivity and it will also serve as an oxygen getter, improving thus the vacuum conditions in the reactor vessel.

In principle, beryllium might serve as a multiplier of neutrons within the so called breeding blanket surrounding the PFCs [19], in which the tritium shall be produced through the reaction with lithium (see Eqs. 1.5, 1.6) and in some concepts it was considered as a potential coolant in the form of a molten salt $LiBe_2F_4$ [20].

Nevertheless there are several drawbacks due to which Be is highly unlikely to serve as a plasma facing material in the next step fusion devices. Mainly it is its toxicity (with the consequent safety regulations to be applied) and significant embrittlement under neutron impact. Moreover, due to its relatively low melting temperature ($T_m = 1287$ °C) it would not sustain the highest heat fluxes during the off-normal events. Relatively low melting point (in comparison with other candidate materials) combined with the low-Z nature of this element and the consequent high erosion/sputtering yields, led to a decision that Be cannot be used as a coating material for the divertor plates, due to direct impact of the particles on these plates and expected operational temperature rising up to 1500 °C. Concerning the fuel implantation, this material shows a saturation when the crystal lattice defects are occupied by hydrogen (or its isotopes). The diffusion of tritium through Be is slow, potential in-situ release of implanted tritium (limited to amount of 700 g in case of ITER) might thus, due to this slow kinetics, represent a potential problem.

Carbon

Carbon is another representative of the low-Z material group ($Z = 6$). Moreover, it does not melt but sublimates at high temperatures ($T_s = 3915\ K$, [21]), which limits a possible deformation, due to formation of molten layers, of originally fabricated components. In addition, laboratory tests revealed that the thickness of the evaporated layer during the simulated transient events was about ten times smaller than that of tungsten [18], the last PFC candidate material that will be presented in this section. Combined with its good thermomechanical properties, carbon was for a long time considered as a candidate material for the ITER divertor plates for the pre-D-T phase of its operation. Divertor graphite tiles were installed on several tokamaks (for example on tokamak ASDEX - Axially Symmetric Divertor Experiment or tokamak JT-60, Japan Torus) and it has been proven that this material configuration is compatible with a variety of plasma confinement modes [22].

In analogy with the previous case of beryllium, there are several drawbacks that limit the application of carbon as a plasma facing material. Thermal conductivity of CFCs degrade significantly when exposed to neutron fluxes [23, 24]. As a low-Z material, carbon is more vulnerable to undergo physical sputtering. Moreover, this element reacts easily with oxygen and hydrogen isotopes which leads consequently to chemical erosion of the surface layers. Eroded material can co-deposit on the vessel wall and it has been shown during the D-T campaigns at JET that co-deposition of tritium with carbon represents the main tritium retention mechanism. Moreover, scaling up the results obtained at JET to the long-pulses expected during the ITER operation, it has been estimated that the

limiting amount of retained tritium would be reached in less than approximately 100 pulses if the divertor would be covered by graphite/CFCs [25]. Original concept of ITER thus contained a replacement of carbon divertor tiles by another material before start-up of the D-T operational phase. In addition, it has been found by conducting a post-mortem analysis of graphite divertor tiles mounted at ASDEX and JT-60 (for a period of time exceeded several months), that the main hydrogen retention was governed by in-depth diffusion and significant amount of hydrogen was found in depths up to several millimetres [26, 27].

Large tritium retention as a consequence of its co-deposition with carbon was the main argument why recently it has been decided that ITER will be from the early stage of its operation designed with an all-tungsten divertor instead of the carbon/tungsten divertor variant [28].

Tungsten

In the context of high temperature environment, tungsten represents a natural PFC candidate material, since it has the highest melting temperature of all metals ($T_m = 3695\ K$). Another favourable property is its low vapour pressure, good thermal conductivity and high-Z nature, which implies low level of sputtering/erosion under particles impact. Tungsten exhibits low retention of hydrogen isotopes, high temperature strength and good thermal resistance under cycling heat loading and thermal shocks. A main disadvantage of this metal lies in his high-Z nature, meaning a necessity of keeping its concentration within the plasma at a low level, and its relatively high ductile-to-brittle transition temperature (DBTT, $DBTT_W \sim 300 - 600$ °C) [29]. Tungsten is brittle at room temperature and must be thus heated above DBTT in order to be machined. Under neutron irradiation the brittle nature of this metal is enhanced. Furthermore, it becomes activated.

Tungsten and its PFC-relevant properties represent the most investigated subject of the ongoing fusion material-oriented research. The current state of art of several aspects of the problematic, important in the context of this paper, will be discussed in further details in the following subsections.

Conceptual design of the ITER divertor

Divertor's main purpose within the tokamak is to remove the impurity atoms from the plasma volume. This is achieved through interception of the magnetic field lines (i.e. the plasma particles) with the so called striking areas, or plasma-facing units, located at the bottom of the inner and outer divertor vertical targets (see Fig. 1.7). After recombining, the neutrals are pumped from the volume of the vessel. Due to the direct impact of the plasma species, divertor plates will be subjected to the highest steady state loading, as was mentioned in the previous sections.

ITER's divertor will consist of 54 divertor cassettes, each of them composed of a cassette body and the PFCs (inner and outer vertical targets, IVT and OVT, and a dome). Beside providing a support for the other components, cassette bodies (CB) will serve as a water guides to the actively cooled divertor pieces. Moreover, CB will also serve as a shield against neutrons for the surrounding tokamak components. Each CB will weight about 4.7 tonnes and will be made

of stainless steel 316 L(N) ITER-grade [30]. Due to a high risk of melting of leading edges during the transient events (namely the most severe ones for this particular component, VDEs) the shape of the OVT will adapt a roof-like form by introducing a chamfer at the OVT edges. In the plasma-facing units the PFCs will be fabricated with the so called fish-scale design, with a 0.5 mm chamfer in the toroidal direction. Such design shall avoid melting of the component edges during ELMs and disruptions [31, 32].

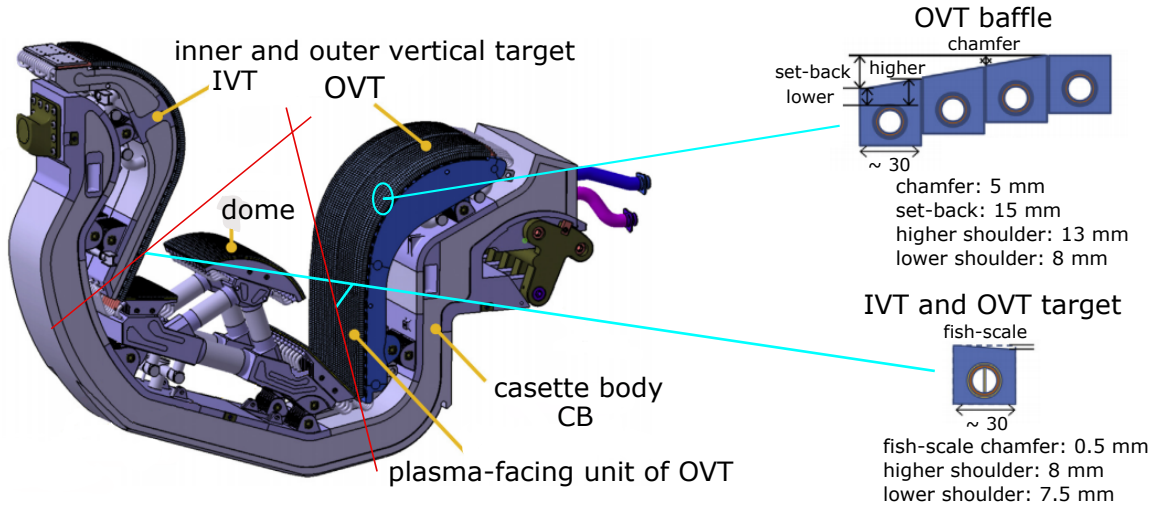

Figure 1.7: 3D drawing of the ITER divertor, detailed design of the vertical components is on the right side [31]. Note the magnetic field lines (red solid lines), intercepting the striking areas.

PFCs constituting the ITER divertor will be actively cooled by water, guided through pipes fabricated from Cu-based alloys. The most considered designs of the divertor units are either in the form of a monoblock (for the IVTs and OVTs) or a flat-tile unit (for the dome), Fig. 1.8. Concerning the flat tile design, in general for the divertor units a high heat removal efficiency is required, thin armour layers are thus favourable. Nevertheless a rather thick armour is preferable from the erosion point of view. At this moment an armour layer of 8 mm has been chosen as a compromise between the two arguments. This layer will be in contact with the material constituting the heat sink, Cu-based alloy (in particular a CuCrZr alloy for ITER tokamak).

Tungsten processing techniques

In order to test the performance of tokamak plasma confinement when equipped with a W-armoured divertor (*ITER-like* configuration), divertor tiles of tokamaks JET and ASDEX were coated with a tungsten layer, deposited on a CFC and graphite substrates, respectively. This configuration was chosen in order to reduce the weight of the components and the occurrence of eddy and halo currents [35]. Various deposition and joining techniques were used when fabricating the mock-ups for this purpose and resistance of the components against thermal fatigue, erosion, hydrogen retention and overall other degradation processes was evaluated [36]. Potential problems related to the usage of a component composed of several different materials might originate for example from a mismatch of their thermal

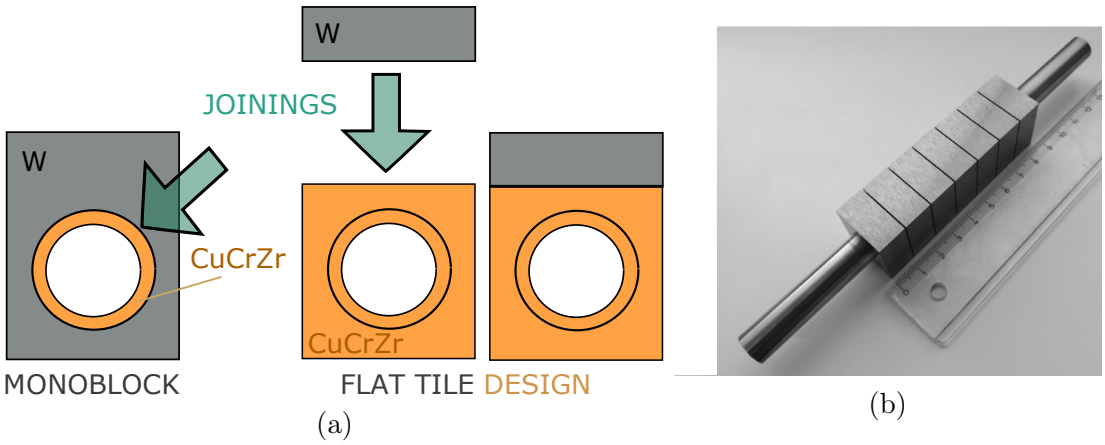

Figure 1.8: (a) Schematic drawing of monoblock and flat tile design of W-armoured ITER actively-cooled divertor unit; (b) fabricated tungsten monoblock mock-up [34].

expansion coefficients (and the consequent residual stresses originating from the manufacturing process) or insufficient adhesion of the coated layer [37].

Nowadays the most investigated material processing techniques in ITER-relevant fusion research are naturally related to preparation of W/Be-Cu components. Tungsten elements shall in principle be prepared according to the so called ITER-grade tungsten model, which comprises a W polycrystalline material that has an improved thermal conductivity along a certain direction [38] (enhancing thus a heat conduction towards the heat sink).

In general, two types of material structures can be distinguished: a dense, *bulk* material, with no apparent as-received internal structure, and deposited/coated one, that reflects characteristic features of the deposition method when inspected with the conventional metallographic methods. In principle, bulk material can be coated by a thin protective layer that provides additional protection of the component.

Tungsten coating techniques

Following tungsten deposition/coating techniques are under consideration for fusion applications:

- **Plasma spraying, PS** - technique that melts and accelerates the material to be coated, supplied in a form of μm-scale powder, by a plasma jet of typical temperature exceeding 10 000 °C. Such temperature range allows deposition of majority of conventionally used materials.

  Principle of the method is illustrated on Fig. 1.9a. Working gas (such as argon, nitrogen etc.) is ionized through an electric arc generated between the cathode and anode of the plasma torch. Molten material, transported by plasma jet towards the substrate, is deposited in the form of flattened liquid droplets. Droplets solidify within a very short time range and the final structure of the coating is thus lamellar, typically highly porous (Fig. 1.9b). In order to reduce the stress between the substrate and the coated layer, it is convenient to supply gradually powders both of the substrate and of the material to be deposited and produce thus the so called functionally graded

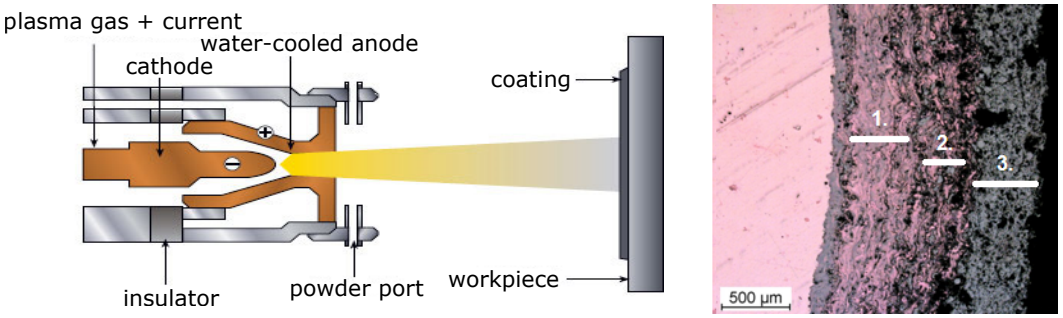

(a) (b)

Figure 1.9: (a) Schematic drawing of apparatus used for PS [39]; (b) FG layer of Cu (region numbered 1) on W (region 3) prepared by APS [40] (note the Cu-W interlayer, region 2).

(FG) deposited layer.

This technique allows deposition of layers of thickness up to several millimetres on large, uneven surfaces. Another advantageous aspect of this method is the possibility of in-situ repairs of damaged layers within the tokamak vessel and its high deposition rate.

Depending on the pressure in which the material is coated, several variants of PS can be distinguished: spraying at ambient atmosphere (APS - atmospheric PS), at low/high pressure (LPPS and HPPS, respectively) or spraying in vacuum (VPS - vacuum PS).

Due to high porosity of the deposited layers, thermal and electrical conductivities of PS coatings are lower in comparison with those of a bulk material (up to a factor of 5 in case of W and Cu [40]). This might be even enhanced when oxide layers are produced during the manufacture of the component (suppressed in case of VPS). Performance of the PS coatings depends also on the level of its adhesion on the substrate. In [41] and [43] it was shown that adhesion could be enhanced through roughening of the substrate surface (for example by grit blasting), by depositing an interlayer between the substrate and the coating and by preheat of the substrate.

Under cyclic heat loading coatings prepared by PS showed a good performance for loads not exceeding ~ 5 MW/m^2 (see for example [37]). Nevertheless under loadings comparable to that of the tokamak transient events the PS coatings exhibited severe melting or even evaporation, probably due to their lower thermal conductivity [42]. PS coatings are also more vulnerable to degradation under neutron irradiation [44].

- **Chemical vapour deposition, CVD** - principle of this method relies on chemical reaction among originally cold reactants, having as a product the compound to be coated and optionally other gaseous products, that are pumped away from the reaction chamber. Reaction takes place on a heated surface serving as a substrate for the deposited layer (Fig. 1.10a). In order to produce CVD-W coatings, following reaction scenario is realized:

$$\mathrm{WF_6} + 3\,\mathrm{H_2} \rightarrow \mathrm{W} + 6\,\mathrm{HF}.$$

Temperature range for this reaction is between $300 - 800$ °C [45]. Main disadvantage of this coating technique is its low deposition rate (< 1 mm/h) even at the highest substrate temperature. It would be also potentially difficult to coat large and curved surfaces. On the other hand, coatings prepared by this method are highly dense, and have thus mechanical properties similar to those of a bulk tungsten (such as the thermal conductivity, hardness etc.). Similarly to PS, CVD can be realized in ambient atmosphere, low/high pressure or in vacuum. Control of the working pressure and of the velocity of the reactants represents another mean to adjust the deposition rate [45]. Resulting W grains within the deposited layer are typically columnar, oriented perpendicularly to the substrate (see an example on Fig. 1.10b). Coatings of width of several millimetres can be prepared by this technique and the as-prepared surfaces are rather rough.

As is the case of PS deposited layers, adhesion of the CVD-W layer to substrate can be enhanced through introduction of an interlayer. The latter also serves as a reducer of the interlayer stress [46]. Performance of CVD-W layer deposited on bulk CuCrZr, with a Cu interlayer, was evaluated after cycling loading by heat fluxes corresponding to normal loading expected in ITER (Fig. 1.5) and no failure of the mock-up was found in the post mortem analysis (component was actively cooled by water during the experiment) [45]. In [47] CVD-W coating was tested under ELMs and disruption-like conditions and two types of crack failures were identified, shallow microcracks and macrocracks along the grain boundaries (GBs) of depth of several hundreds of micrometers. In general, crack formation under heat loading is associated with induced thermal stress that is able to surpass the tensile strength of the material. Appearance of major cracks is explained by high DBTT (compared to bulk material) of the CVD-W coatings that is explained by presence of fluorine impurities in the GBs and the consequent brittleness of the material [48]. Once the tested sample was heated above certain threshold temperature, formation of macrocracks was suppressed. Only the microcracks were formed, and these are supposed to be related to the plastic deformation being a consequence of a thermal fatigue of the material.

Ren et al. [49] proposed recently to replace traditionally used source reactant WF_6 by tungsten carbonyl $W(CO)_6$. Main arguments used in this proposal are such that the reaction temperature is lower (about 400 °C) and unlike WF_6, tungsten carbonyl is an un-corrosive gas, which implies protection of the fabrication facilities. Research in this direction is ongoing.

- **Physical vapour deposition, PVD** - this term comprises a variety of coating methods (performed in vacuum). Nevertheless the basic principle is common for all of them - physical process (sputtering, heating) is required to mobilize material from a target (= to produce a vapor) that is then deposited on a substrate. This method is suitable to produce thin layers (of several tenths of micrometers) of practically any organic or inorganic compound. In [50] fine grain graphite substrate was coated by W using three different PVD techniques, specifically by electron beam evaporation,

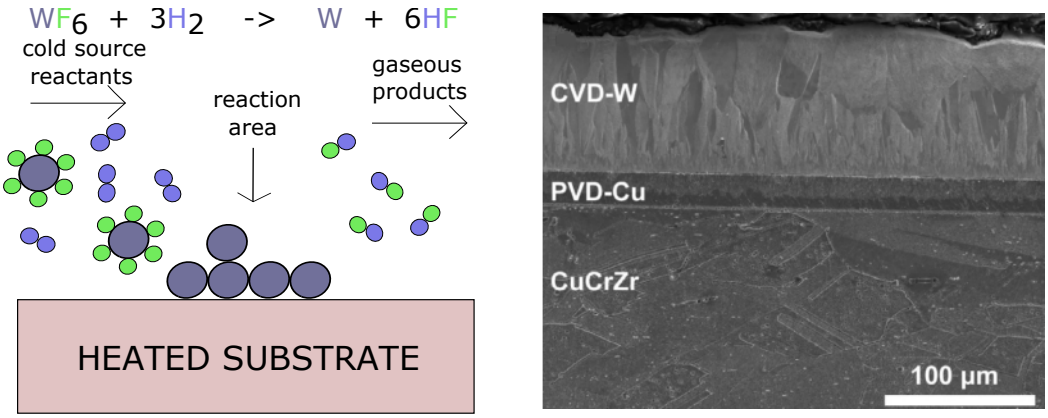

(a) (b)

Figure 1.10: (a) Schematic drawing of apparatus used for PS [39]; (b) example of CVD-W layer deposited on CuCrZr, with a Cu interlayer prepared by physical vapour deposition (note the columnar structure, perpendicular to substrate, of the CVD-W layer) [45].

magnetron sputtering and arc deposition and their adhesion properties were evaluated. It turned out that the sample coated by magnetron sputtering suffered from delamination of the coated layer and this was explained by high level of initial residual stresses.

A campaign launched in 2005 had as goal to find the most suitable coating technique for W deposition on CFC substrate. Such configuration was foreseen to be used in the divertor of the JET-like wall project. Coating CFCs with techniques previously tested on manufacture of W-fine grain graphite components turned out to be problematic due to irregular surface of CFC substrate [51]. Based on the results of the loading tests, it was decided to use as a deposition technique a magnetron sputtering combined with implantation of ions, since samples prepared by this method showed the highest performance during the tests and an industrial large-scale production of these coatings was achieved [52]. A Mo interlayer was produced between the PVD-W coating and the CFC substrate in order to reduce the interface stresses and enhance the adhesive properties of the coating. Resulting layers showed, just as was the case of the CVD deposition method, a columnar grain structure. The highest achieved deposition rate did not exceed 10 μm/h.

Combined magnetron sputtering and ion implantation, CMSII - target fabricated from the material to be deposited is enclosed with the substrate within a vacuum chamber. Working gas (typically Ar) is then introduced in the chamber and further ionized trough glow discharge by applying a high voltage. Ions are accelerated towards the target from which the atoms are sputtered and further deposited on the substrate. Magnetic field lines introduced in the configuration assure that the charged particles are kept in the proximity of the targets, intensifying thus the ion bombardment of the target [53]. CMSII technique introduces a high energy ion bombardment in the deposition process through application of high voltage pulse discharge. Accelerated ions strike firstly the substrate and then the deposited layer

itself. As a consequence of this bombardment, the surface mobility of the deposited atoms is enhanced (leading thus to higher density of the deposited layer), the structure is pore free, with the final size of the crystallites within the nano-meter scale [54].

Up to this date no experimental campaign focused on evaluation of CMSII-W coating performance with Cu as a substrate has been reported. Nevertheless this option might be investigated in the future.

Bulk-tungsten preparation techniques

Concerning the bulk material preparation techniques, those typically consist of powder metallurgical processes, followed, if desired, by hot working. Authors of [55, 56] investigated performance of ITER-grade bulk tungsten under transient-like heat loading. Samples tested in the scope of these experiments were prepared by Plansee AG [57] and the fabrication process consisted of the following steps: firstly the homogenized powder underwent cold iso-static pressing in order to form the so called green compact; secondly the compact was sintered at temperatures ranging between $2000 - 2500$ °C; finally, in order to achieve the preferential grain orientation (fulfilling the ITER-grade requirements), the specimens were deformed by forging, swaging or by rolling. In both sets of samples major cracks of depth of several hundreds of micrometers, propagating along the GBs of the elongated grains, appeared when the samples were not heated above their DBTT during the exposure. This was again explained by brittleness of the material, mostly pronounced in the region of GBs. Above DBTT, network of shallow cracks, surrounding the grains along the GBs in the plane perpendicular to the heat load propagation, developed under certain range of heat loads. These were formed as a consequence of plastic deformation occurring at the highest temperature of the sample, followed by rupture during the cooling phase. Moreover, in [55] melting and resolidification of the surface layer was observed.

Sintering, in its most general form, represents a material processing technique in which the material, in the form of powder, is heated and pressed in such a way that a compact is formed, but without achieving the point of the material's complete melting. Through control of the sintering parameters (temperature, pressure and sintering time), grains are thus bound together through atomic diffusion. Typically the temperature to be applied shall be at least half of the melting temperature of the sintered material, so that the diffusion is sufficient to form bounds that are reflected in required mechanical properties of the fabricated specimen. In case of inappropriate adjustment of the sintering parameters, diffusion might lead to excessive grain growth or even disappearance of the grain structure [58]. It is thus evident that through adjustment of the fabrication parameters this method provides a possibility to control grain size of the prepared component.

In experiments reported in [59, 60] sintered W samples underwent transient-like heat loadings and it was found that under comparable experimental conditions, sintered samples were more vulnerable to crack formation and loss of grains during the subsequent transient loadings than the deformed samples.

Among sintering techniques, the variant entitled as **Spark Plasma Sintering (SPS)** is of particular interest in the context of this work.

Particularity of this method lies in simultaneous pressing (within a graphite die, for example, Fig. 1.11) of the powder and application of pulsed or steady direct current. The ohmic heating is responsible for increase of the powder's temperature up to the predefined point. Electrically conductive sample is thus heated, diffusion is enhanced thanks to the applied electric field (theoretically of magnitude $\sim$ kV/m between the individual grains). Main advantage of this technique is a very high heating rate (up to 800 °C/min), which is favourable when specimens of small grains are to be prepared [61]. Moreover, the sintering time is shortened down to few minutes, supporting thus a potential industrial-scale component fabrication. SPS technique provides possibility of porosity control through interruption of the fabrication process before full densification of the component is achieved. Samples are typically fabricated in vacuum (to avoid oxidation and enhance the purity of the prepared component) or, if the sample is to be heated above certain threshold temperature, in a protective atmosphere so that the heat radiating on the walls of the preparation chamber is partially dissipated.

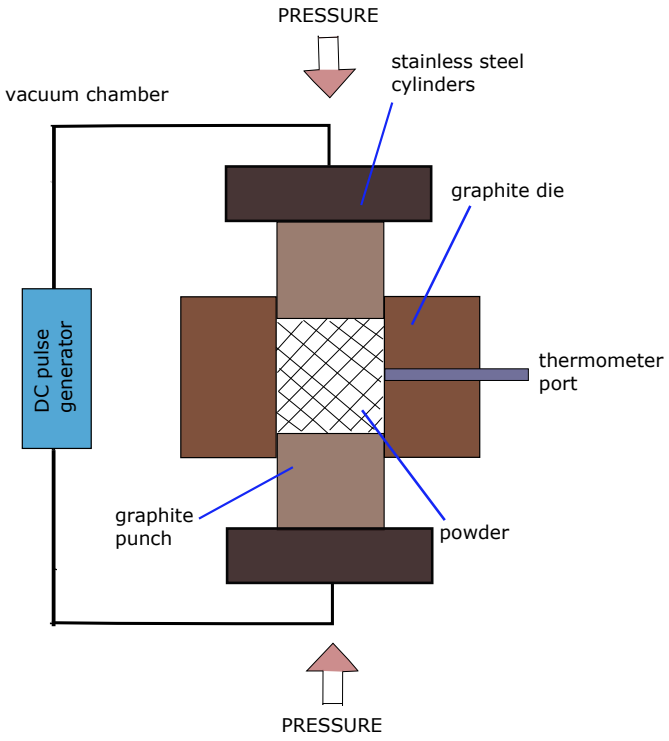

Figure 1.11: Sample preparation with SPS technique.

SPS provides possibility of fabricating FG materials in a very simple way, which consists just of mixing the different powders in the required ratio. For example in [62] samples of varying volume ratio of steel P91 and W were successfully prepared, which provided possibility of evaluation of the mechanical and thermal properties (hardness, thermal conductivity) of the individual phases in the composites. Such information represents an important step in preparation of SPS FG layers in the future.

Moreover, with SPS, doped materials can be prepared. Advantage of dop-

ing lies in the limitation of the grains growth and possibly strengthening of the GBs. Lemahieu in the scope of his work [58] evaluated performance of series of Y-doped tungsten (of $Y0.25 - 1$ wt%) prepared by SPS under thermal shock loading. Addition of yttrium improved the sample's thermal shock resistance at room temperature (RT). It is worth mentioning that other advantageous aspects of W-doped materials (studied on samples prepared by other methods than SPS), such as higher recrystallization temperature, resistance to creep and lower DBTT (implying thus possibility to machine the material at lower temperatures) are under investigation and the simplicity of preparation of these materials by SPS represents an attractive option to investigate.

W-CuCrZr joints

According to [63], the flat tile joints will be realized through brazing and the monoblock ones either with the use of the hot isostatic pressing or the hot radial pressing. An important aspect while optimizing the joining methods must be a requirement of not affecting the thermochemical properties of the CuCrZr alloy. In order to compensate the mismatching thermal expansions of the two components to be joined, a Cu interlayer is envisaged to be included in the design. Performance of the joints is tested, as is the case of the W coatings and W bulks, under cyclic heat flux loading. For example, large-scale flat tile W-CuCrZr mock-ups joined with brazing (and using Cu-Mn as a filler) withstand steady state heat fluxes of 7 MW/m^2, as reported in [64], small-scale mock-ups could withstand fluxes up to 20 MW/m^2 with no failure of the joint. Optimization of the joints is ongoing.

Performance of tungsten under thermal and particle loading

In the previous section various tungsten processing methods were described and as it has been recently pointed out in [65], methods for fabrication of ITER divertor components are in principle available. This means that at this point W-CuCrZr monoblocks/flat tile components can be manufactured and sustain, with certain level of damage, required number of heat loads by fluxes not exceeding 20 MW/m^2, corresponding to expected normal loading during the ITER operation. Nevertheless some design modification might be considered in future (e.g. reduction of the tungsten layer thickness from 8 to 6 mm) in order to reduce typical failure modes, such as appearance of cracks in the tube axis direction (the so called self-castellation failure).

An important concern related to adopting tungsten as a material for the divertor's armour lies in the fact that tungsten can *melt* under transient heat fluxes (recall the carbon, which sublimates). Melting and the subsequent degradation processes might in the end lead to macroscopic erosion of the armour material. Eroded, high-Z particles diluting the plasma might degrade its confinement through enhanced cooling via radiation and in the worst case, eroded material can trigger the plasma disruption. Although some of the failure modes were mentioned in the previous parts when evaluating performance of coatings/bulk W specimens under normal/transient loadings, progressive damage steps (so far reported) that a tungsten armour can experience, will be summarized (in a simplified scenarios) in the following text, with the help of Fig. 1.12.

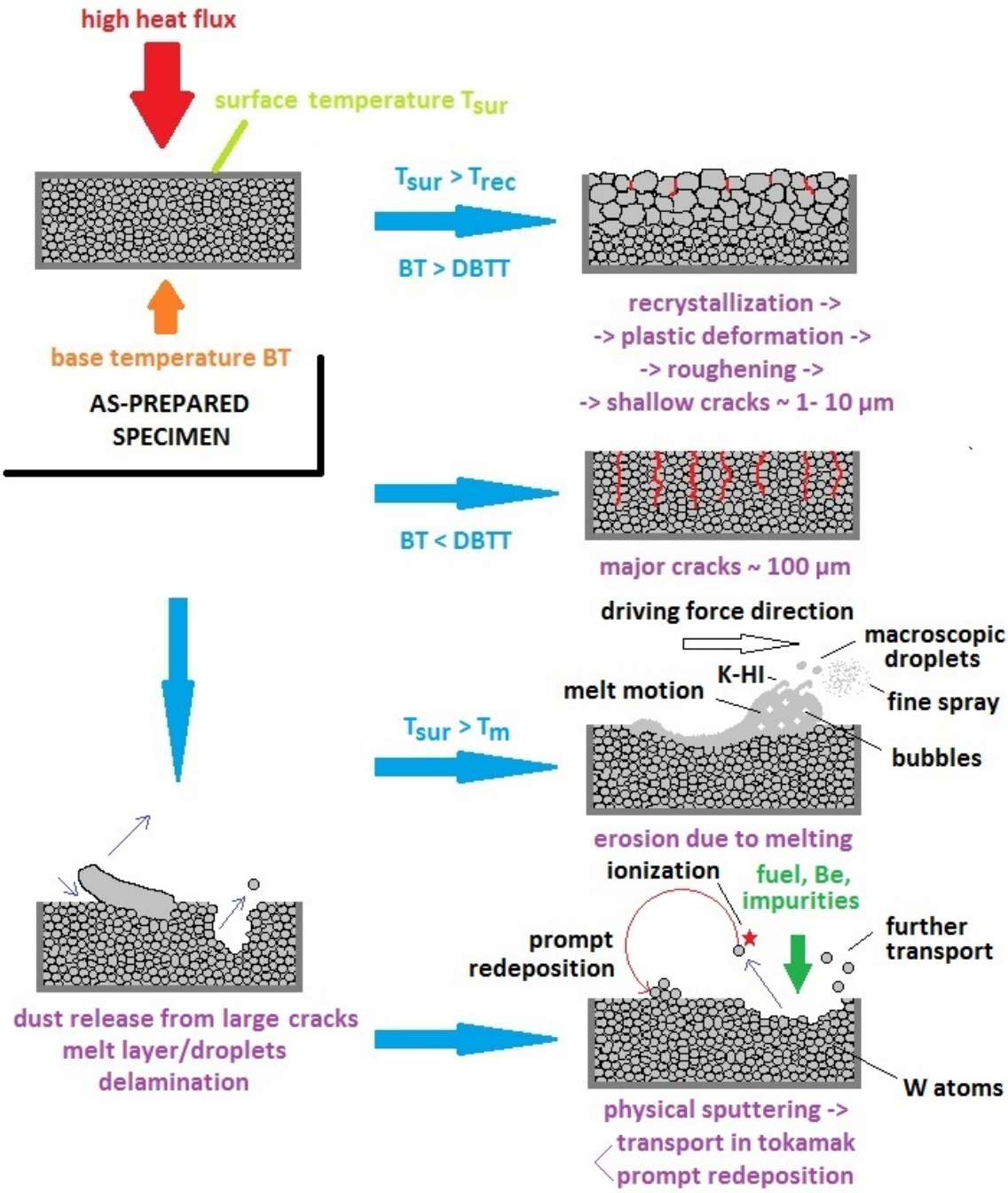

Figure 1.12: Simplified scenarios of W-armour damage.

As a starting point a specimen with defined grain size and texture (if desired) shall be considered. Due to thermal loading of the sample the surface temperature T_{sur} can exceed the recrystallization temperature of the particular tungsten grade, varying typically between $1300 - 1600$ °C [34]. Due to recrystallization, yield and tensile strength might be decreased as a consequence of increased grain size. Hardness of the material decreases as well. The lower the yield strength, the more probable it is that the following high temperature gradients, inducing thermal stresses (since the hot part of the sample would be expanding and the cold one contracting) would be such that the material would start to deform plastically. Plastic deformation would be reflected as an increase of the surface roughness.

When the tensile stresses overcome the tensile strength, rather shallow cracks are formed along the GBs [56]. In this scenario a base temperature (BT) of the sample is above the DBTT.

When the BT of the loaded sample is below its DBTT, major cracks of depth of several hundred micrometers might be formed due to the brittle nature of the material.

In order to generalize conditions under which tungsten layer can melt, the so called heat flux factor, F_{HF}, was introduced in the fusion community, with

$$F_{HF} = q_{\perp} t_{trans}^{-1/2}, \tag{1.8}$$

where $q_{\perp}$ stands for the energy density impacting the target in a perpendicular direction and t_{trans} is the duration of the heat pulse [28]. Condition for a tungsten melting is such that:

$$F_{HF} \gtrsim 50 \text{ MJm}^{-2}\text{s}^{-1/2} = 50 \text{ MWm}^{-2}\text{s}^{1/2}. \tag{1.9}$$

In the presence of sharp edges, with decreased thermal conduction towards the substrate, lower F_{HF} than given by Eq. 1.9 is enough to cause the melting of this region. In any case, temperature must exceed the melting point of tungsten during the heat load. Once the material is molten, it might be mobilized due to application of a driving force, which can be a consequence of gravity, pressure of the plasma or Lorentz-forces $F_{j\times B}$ (when present in tokamak, B is the toroidal magnetic field and j the thermionic emission current of the W sample, perpendicular to the surface) [66]. Motion of the molten layer represents one mechanism of loss of molten material, another one is formation of droplets that are splashed away either in a form of a fine spray or as rather μm-large liquid droplets. Development of Kelvin-Helmholtz instabilities (K-HI) might explain the formation of droplets [67]. This kind of instability is formed when there is a difference of velocities across the interface of two fluids [68]. Droplets splashing might be also explained by formation of vapour above the melt layer and consequent increased pressure above it. Formation of bubbles within the molten layer was observed too. These were explained by boiling of the liquid phase [14]. Note that in some experimental campaigns bubbles were also found at GBs within the recrystallized bulk material and those were explained by defects migration and accumulation at the GBs [70].

Another erosion scenario to consider is the physical sputtering (by fuel atoms, first wall materials such as Be, impurity ions or even by self-atoms) of the surface layer. As a high-Z material, tungsten atoms are less sputtered from the surface layers in comparison with previously considered PFC material, carbon. Moreover, it has been shown that large fraction of the sputtered atoms ($\sim$ 50 % [71]) are promptly redeposited back on the surface in tokamaks, limiting thus the dilution of the plasma. This is a consequence of the fact that ionization length of tungsten is typically much smaller than its Larmor radius, r_L (m being mass of the charged particle, $v_{\perp}$ component of its velocity in direction perpendicular to the direction of the magnetic field, q electric charge of the particle [9]),

$$r_L = \frac{m v_{\perp}}{|q|B}, \tag{1.10}$$

when considering ionization scheme W I $\rightarrow$ W II. In case that the sputtered atoms are not redeposited promptly, they might be ionized, transported along the

magnetic field lines and redeposited in distant areas. Or the atoms might travel within tokamak, avoid ionization and redeposit on areas on which no magnetic field lines are intercepting (see Fig. 1.13).

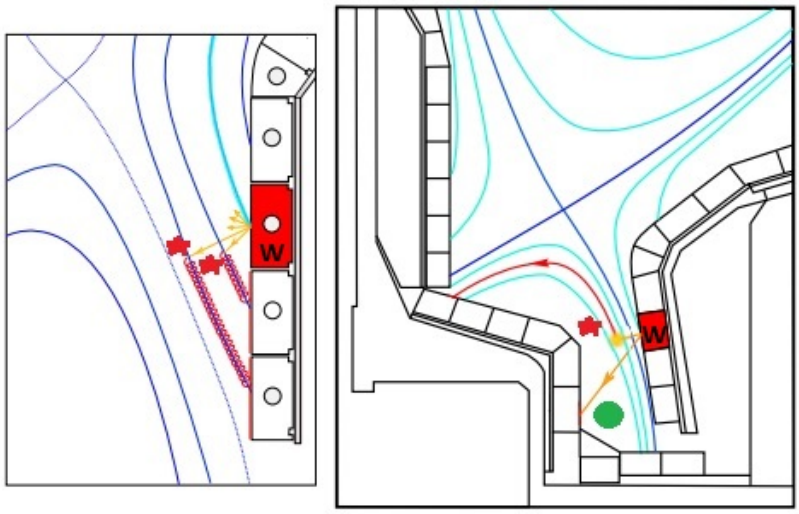

Figure 1.13: Transport of sputtered tungsten atoms within the tokamak vessel [72].

Since the magnetic field lines show often repetitive configuration in between the tokamak discharges, erosion-dominant and redeposition-dominant regions within the vessel wall can be typically distinguished. For example experimental investigation of set of tungsten poloidal tiles of ASDEX tokamak divertor showed that the inner divertor targets are mainly subjected to erosion and outer ones to redeposition [73].

Another significant source of erosion can be the ignition of arcing on tungsten plates. Arcs are mainly ignited during the transient events, in areas of higher neutral pressure. During arcing, layers of material of thickness of several micrometers can be removed [74, 75].

Finally, resolidified layers, craters with sharp edges, redeposited and resolidified splashed droplets and other macro-scale objects might be mobilized during the transient events. Their transport within the tokamak vessel represents a potential risk of plasma disruption. Moreover, thick, open cracks might serve as a source of dust as well.

Of course, the real situation becomes much more complicated when the above mentioned scenarios superpose. W-armour damage represents thus a complex problematic and will be in a focus of further investigation.

As it was mentioned previously, the highest risk related to dust/particles release within the tokamak vessel is the possible triggering of plasma disruption. Nevertheless safety (and from the plasma control point of view, practical) regulations applied to ITER limit the maximum acceptable amounts of dust to total 18 kg [76]. Some parts of the tokamak vessel will be preferentially eroded (see above) and it is thus important to evaluate both the overall erosion of the surface layers (and decide eventually about renewing the coatings) and to measure the erosion rate in-situ, in real time (= "online"), during the discharge, so that the potential risk related to excessive erosion rate would be revealed. It is therefore necessary

to equip ITER with a set of diagnostics offering the possibility of online erosion monitoring. Requirements for ITER concerning the time and spatial resolution of the diagnostics are as follows: to monitor the erosion range up to 3 mm with an accuracy of 50 μm per discharge; resolve erosion rate of $1 - 10$ μm/s with a 30 % accuracy and time resolution of 2 s. Candidate diagnostic methods are the following ones [77]:

Visible-UV spectroscopy - spectroscopy as a plasma diagnostic method relies on collection of photons radiated from the plasma volume. Radiation intensity is typically plotted as a function of the wavelength in the so called spectrum. Energies of emitted photons depend on the atomic processes that lead to their release and the resulting wavelength range of interest vary from the short wavelengths in the soft X-ray region (from the plasma core region) up to the visible range. For the purpose of erosion monitoring, *line radiation* is of interest. Such radiation occurs for electron transitions between bound levels (below the ionization potential, E_∞). Considering the following transition between levels of principal quantum numbers $p \to q$ $(p > q)$, the energy of the emitted photon is given by:

$$\Delta E_{p\to q} = E(p) - E(q) = h\nu_{p\to q}, \tag{1.11}$$

where $\nu_{p\to q}$ is the photon's frequency and h is the Planck constant. For hydrogen-like atoms the Rydberg-Balmer formula yields [78]:

$$\Delta E_{p\to q} = RZ^2(1/q^2 - 1/p^2), \tag{1.12}$$

with Z being the atomic number and R the Rydberg constant for this element,

$$R = R_\infty/(1 + m_e/M), \tag{1.13}$$

where m_e is the electron mass, M is the total mass of the atom and $R_\infty = 13.61$ eV. For an atom that has just been sputtered from a surface layer, it is typically valid that energy of the impacting particles within the plasma edge is such that only first or second ionization stages are important. Therefore the wavelength range of spectrometers installed on tokamaks for the purpose of erosion control is typically tuned for observation of a strong line emission from neutral, once or double ionized atoms of interest. For example in JET the erosion of carbon and beryllium was detected via emission of C III and Be II lines. Erosion of tungsten tiles mounted on the outer divertor was analysed via detection of emission from neutral W I at $\lambda = 400.9$ nm and once ionized W II at $\lambda = 364.0$ nm [71]. Collection of light spectra represents an easy method enabling to monitor the erosion and once the spectrometer is absolutely calibrated, it is possible to determine the concentration of the eroded (impurity) ions.

In Vessel Viewing System, IVVS - this diagnostic uses a laser radar with amplitude modulated at 80 MHz. Intensity and phase shift of the reflected beam is detected and the surface is scanned with the use of a rotating prism. According to the characterization of the measuring system described in [79], this technique does not fulfil the ITER requirements in terms of erosion rate and range. IVVS in ITER will be installed in 6 ports and will be able to scan all surface of its vacuum vessel in 8 hours [76].

Speckle interferometry - this method uses again a laser of $\lambda = 562$ nm whose reflected beam interferes with a reference beam on a CCD (Charge-Coupled Device)

camera. Using four interferograms, with a phase shift of $\pi/2$, the phase of each pixel can be calculated and the variation of the phase during a time Δt allows to determine the erosion rate. The time resolution is about 0.4 s, spatial approximately 100 μm and the depth resolution is around 25 nm. In case of erosion exceeding $\lambda/2$ the phase shift cannot be detected and so the method is improved using two different wavelengths. For more details concerning this diagnostic see [80]. This technique meets the above mentioned requirements.

D/T retention

Fuel inventory within the PFCs represents a key issue for ITER from the safety regulation point of view. Maximum amount of tritium that can be retained within the PFCs is set to 700 g [81]. Large affinity of carbon to co-deposit with tritium led to its exclusion from the list of the candidate PFC materials, since the T-700 g safety limit would be reached just after $\sim$ 350 ITER discharges of expected duration of 400 s, Fig. 1.14. Results from the ITER-like wall project in JET showed a reduction by a factor $\sim$ 10 in T retention when carbon components were exchanged by the Be-W variant [82].

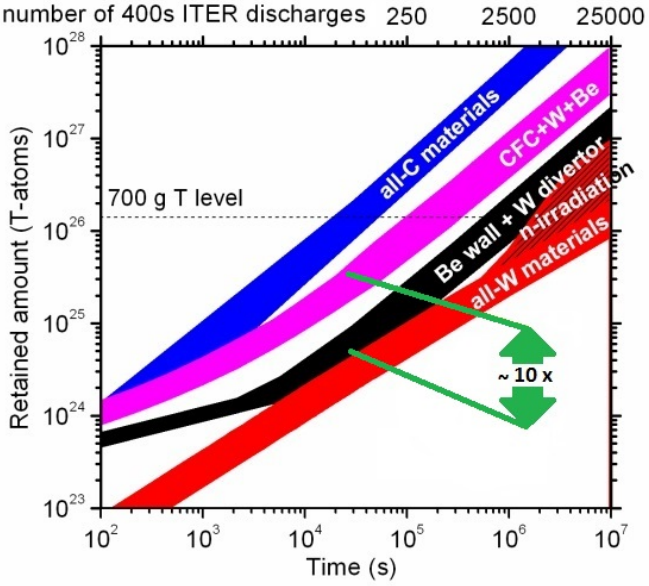

Figure 1.14: Comparison of T inventory for various options of material choice for PFCs. Note the factor of $\sim$ 10 when passing from CFC-Be-W to just Be-W variant [81].

Hydrogen atoms are in general very mobile within the W and the total amount of hydrogen that can be permanently retained is dependent on the concentration of the defects of the crystal lattice, since those defects act as traps for the implanted hydrogen atoms. Trapped hydrogen can be released through thermal activation of the de-trapping process followed by a diffusion towards the surface, where it can recombine with another atom and leave the surface as a molecule (the so called Langimur-Hinshelwood recombination, Fig.1.15) [83]. Although the mobility of the hydrogen within the bulk is rather high, concentration of hydrogen is typically larger at the surface than in the deeper regions. This is due

to the fact that the potential barrier for in-depth diffusion is larger than that of the at-surface recombination of the atoms.

Tungsten specimens, subjected to D-plasma, showed two types of damage, depending on the energy of the impacting ions. For ions of rather low energy (of the order of tenths of eV) a pronounced plastic deformation of the surface layer was observed, leading even to formation of shallow cracks/cavities along the GBs. This is thought to be a consequence of relaxation of stresses induced by concentration of D particles, that exceeded tungsten's solubility limit. Above-surface region thus got supersaturated which resulted in increasing the stress exerted on the surface of the tungsten sample [84]. Cracks along GBs represent another trap for deuterium atoms. Moreover, hydrogen retained along the GBs might enhance the brittleness of the tungsten specimen. Once the energy of the impacting ions exceeds certain threshold ($\sim$ 1 keV), those can cause displacement of the W atoms and formation of lattice defects within the bulk volume.

In the context of tritium retention within the fusion reactor's PFCs, it is important to develop tritium-removal techniques that can be implemented as a standard maintenance procedure. Tritium might be removed from the PFCs for example through *isotope exchange*, by exchange of tritium by deuterium (tritium-protium exchanged is not so effective due to larger mass ratio). Adsorbed atoms are removed from the surface by impact of a free atom, via Eiley-Rideal or Hot-Atom recombination processes, Fig. 1.15 [85]. Experimental investigation of isotope exchange reported in the last reference showed that this mechanism is effective at the surface at temperatures around $\sim$ 480 K, while in the bulk the isotope exchange is effective at higher temperatures ($\sim$ 600 K). Investigation of in-bulk isotope exchange is ongoing.

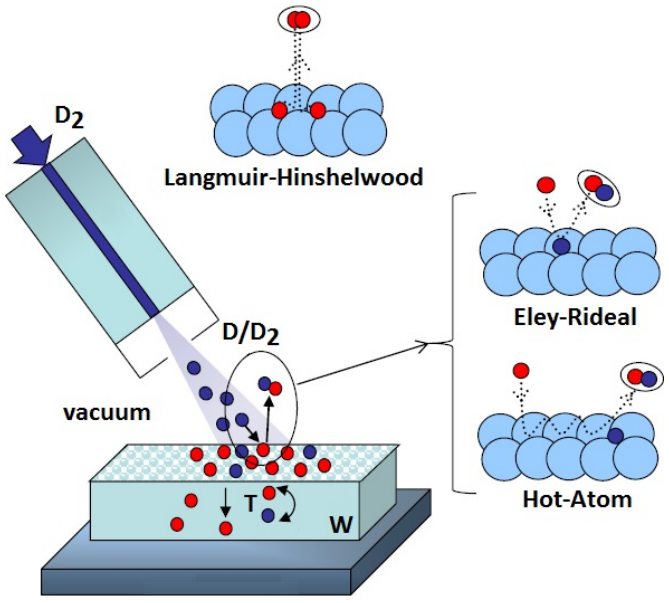

Figure 1.15: Isotope exchange mechanisms. Also shown is the Langmuir-Hinshelwood recombination scheme [86].

In recently performed experiments it was found that large amounts of tritium are retained within tungsten dust in comparison with the bulk samples. This gives an evidence of important surface effects that shall be subjected to further investigation [87, 88].

Finally, it is necessary to mention that irradiation by the products of the D-T fusion reaction increases the concentration of defects within the W lattice (all over the volume of the specimen, not only in the near-surface region). Consequently, more hydrogen can be trapped within the bulk, which is reflected in Fig. 1.14, where n-irradiation results in a lower number of ITER discharges that the all-W PFC option would allow before reaching the T-700 g safety limit.

1.4 Outline of the thesis

Tungsten is currently considered as a main candidate material for PFCs of ITER divertor. As such, its fusion-relevant properties represent a hot topic to investigate. Two distinct approaches can be adapted in the experimental tungsten plasma-surface interaction (PSI) research:

- simulation of tokamak-like conditions in various plasma generators or other facilities and devices,
- evaluation of specimen's performance under real tokamak discharges.

Both approaches are met in the scope of this work and results of two distinct experiments will be presented here. Since the first approach typically precedes the second one, results of experiment focused on evaluation of resistance to transient loading of a set of samples of defined properties will be first presented in Chap. 2, labelled 'Experimental campaign'. Results presented in Chap. 3 follow the second approach and will be thus labelled 'Next step experiments'.

EXPERIMENTAL CAMPAIGN - simulation of steady state and transient loading on W-SPS with variable grain size

So far it has not been decided which processing technique will be used for manufacture of the ITER divertor components. SPS might represent an attractive option in this context due to all its advantageous aspects introduced in the previous section. Key parameter influencing the specimen's mechanical properties is the size of its grains. With SPS, the size of the grains can be controlled by just tuning the fabrication specifications (temperature, pressure, sintering time). *Goal of the Experiment A is to evaluate W-SPS performance under simultaneous exposure to deuterium plasma and transient heat loads in a plasma generator within a parameter scan, with the grain size being the parameter to be varied.* After-exposure (= "post mortem") analysis of the samples will consist of:

- metallography of the exposed areas by means of optical and electron microscopy,
- evaluation of surface roughness via optical profilometry,
- measurement of the size of coherently diffracting domains (= crystallites) and microstrain by means of X-ray diffraction,
- cross-sectional metallography by electron microscopy,

- determination of deuterium concentration within the samples by elastic recoil detection analysis,

- measurement of Vickers microhardness of selected samples.

If necessary, other experimental methods might be used to investigate features of the irradiated regions.

Outcomes of this experimental campaign will be reflected in the future investigation proposals concerning the W-SPS samples.

NEXT STEP EXPERIMENTS - study and online monitoring of erosion of W samples exposed to COMPASS-D tokamak plasma

Tokamak COMPASS-D (COMPAct ASSembly), currently installed and operated at Institute of plasma physics in Prague, is one of the three tokamaks in Europe that are able to achieve H-mode in ITER-like plasma configuration. Tokamak department at IPP runs an extensive scientific program, focused on H-mode physics, plasma edge properties, evolution of magneto-hydrodynamic equilibrium and instabilities and other fusion-physics aspects, that are out of the scope of this work. In 2013, plasma-wall interaction activities started at COMPASS, with installation of a manipulator that is able to provide a support and positioning within the vacuum chamber for set of samples to be exposed to tokamak plasma. During December 2013 and February 2014 tungsten (pure W) and stainless steel (P92 steel) samples were mounted on the manipulator and exposed to series of plasma discharges. This campaign was focused on evaluation of the erosion of the samples when subjected to disruptions, H-mode discharges and accompanying ELMs in the specific configuration of the COMPASS-D tokamak. As was previously explained, variety of in-situ erosion monitoring techniques can be used while the most simple one is through the detection of the emission lines originating from the eroded particles. *Main goal of Experiment B is to evaluate usability of the spectroscopic measurements during the PSI experiments at COMPASS-D, with emphasis on W sample.*

Outcomes of this analysis will influence the diagnostic set-up of the future PSI experiments at COMPASS-D.

2. Experimental campaign - simulation of steady state and transient loading on W-SPS with variable grain size

Set of samples of variable grain size was prepared by SPS method in the scope of this chapter, exposed to simultaneous loading by plasma particles and transient loads and post-mortem analysed. Chapter will thus include description of the sample preparation procedure, description of the exposure facility and exposing parameters, introduction to measurement techniques used during the post-irradiation analysis and its results. Main findings of the campaign will be summarized at the end of the chapter. Given will be also comparison of the main outcomes of this work with results of similar experiment performed on ITER-grade tungsten samples. Results of the latter will be presented in the very first subsection of this chapter.

2.1 Results of comparable experiment with forged ITER-grade tungsten samples

Linear plasma generator, equipped with a wave guide for high energy laser beam, represents a great tool to study performance of test samples under simultaneous exposure to plasma particles and transient heat fluxes. Such 'dual' exposure represents more realistic tokamak-like loading conditions in comparison with for example purely thermal sample loading by an electron beam, scanning the specimen's surface. It has been recently shown that synergistic effects of the simultaneous exposure are reflected in the subsequent nature of the sample's damage [17]. W-SPS samples, studied in the scope of this work, underwent exposure to steady-state deuterium plasma (D-plasma) and transient-like heat pulses in PSI-2 linear device, installed at Forschungszentrum Juelich (FZ-J[1]), Germany. Exposure was made following a standardized scenario that allows to study effects of ordering of the particular loads (steady state or transient). Three different loading sequences are made within one exposition, on one particular sample:

a) exposure to laser pulses, followed by steady state loading by D-plasma,

b) simultaneous exposition to laser beam and D-plasma,

c) pre-exposure by D-plasma followed by exposition to laser pulses.

The procedure will be further explained in Sec. 2.3. It has been reported, in [17, 89, 90], that areas differing by the loading sequence show different features of the consequent surface damage. Results of these experiments, all performed at PSI-2, will serve as a certain comparative point for the results obtained within this work. This is because of the following reasons:

[1]Leo-Brandt-Straße, 52428, Jülich

- firstly, tungsten samples studied in the above mentioned references were fulfilling the ITER-grade specifications (i.e. with elongated grains) and since the loading conditions were very similar to those applied to the set of the W-SPS samples, influence of the manufacturing processes (and grain shape) on the specimen's performance under the heat/particles loading can be evaluated;

- secondly, as pointed out in [17], damage of samples depends on the loading conditions, which can in principle differ from machine to machine, for example by the heat pulse shape (rectangular, triangular..). In the sake of a correct interpretation of the results, samples loaded within the same facility shall be compared.

Orientation of the elongated grains was either perpendicular or parallel with respect to the loaded surface in the above mentioned experiments. Grains length was about ~ 100 μm and the mean diameter was approximately ~ 40 μm. Results of the experiments are hereby summarized:

- At BT = RT or 100 °C *blisters* of size $\sim 1-2$ μm were found on surfaces loaded with sequences b) and c). Those are supposed to be a consequence of the *hydrogen embrittlement*, e.a. concentration of hydrogen along the GBs and lattice defects, which might form bubbles filled with gas molecules leading to a blister-like formation on the surface. Indeed, detailed investigation revealed voids under the blisters, in a depth of few micrometers.

- Crack networks were found on areas loaded with sequences b) and c) with BT set to RT or 100 °C. This is explained by lower ductility of the material due to the hydrogen embrittlement.

- At BT = 400 °C, formation of blisters was practically suppressed. Probably this is because of faster diffusion of the hydrogen atoms in the near-surface region.

- At BT = 400 °C, main damage of the surface consisted of its roughening. The higher the power density absorbed during the transient events, the larger the final roughness of the surface. No cracks were found.

- Damage of the surface shows no dependence on the loading sequence at BT = 400 °C.

- At BT = RT - 130 °C, enhanced D retention was observed for sequence b) in the bulk region of the samples. Probably it is due to the enhanced diffusion of the hydrogen towards the depth of the material (because of the large temperature gradient) and increased mobility of the hydrogen atoms along the cracks induced by the transient-like thermal shocks.

2.2 Sample preparation by SPS

In order to prepare W-SPS bulk samples with variable grain size, as a starting point tungsten powders of different grain sizes were selected. Manufacturer of

the powders, the Global Tungsten & Powders [91], guarantees 99.95% purity of the powder. Content of the oxygen (responsible for oxide layer formation) is typically around wt.% 0.04. Content of other elements, such as Al, Ca, Co, Cr etc. is usually $\lesssim 20$ ppm.

Samples were prepared at Institute of Physics of the Czech Academy of Science (IP CAS[2]), in SPS device 10-4, Thermal Technology LLC, Santa Rosa, USA [92]. Procedure of the sample preparation is as follows (Fig. 2.1):

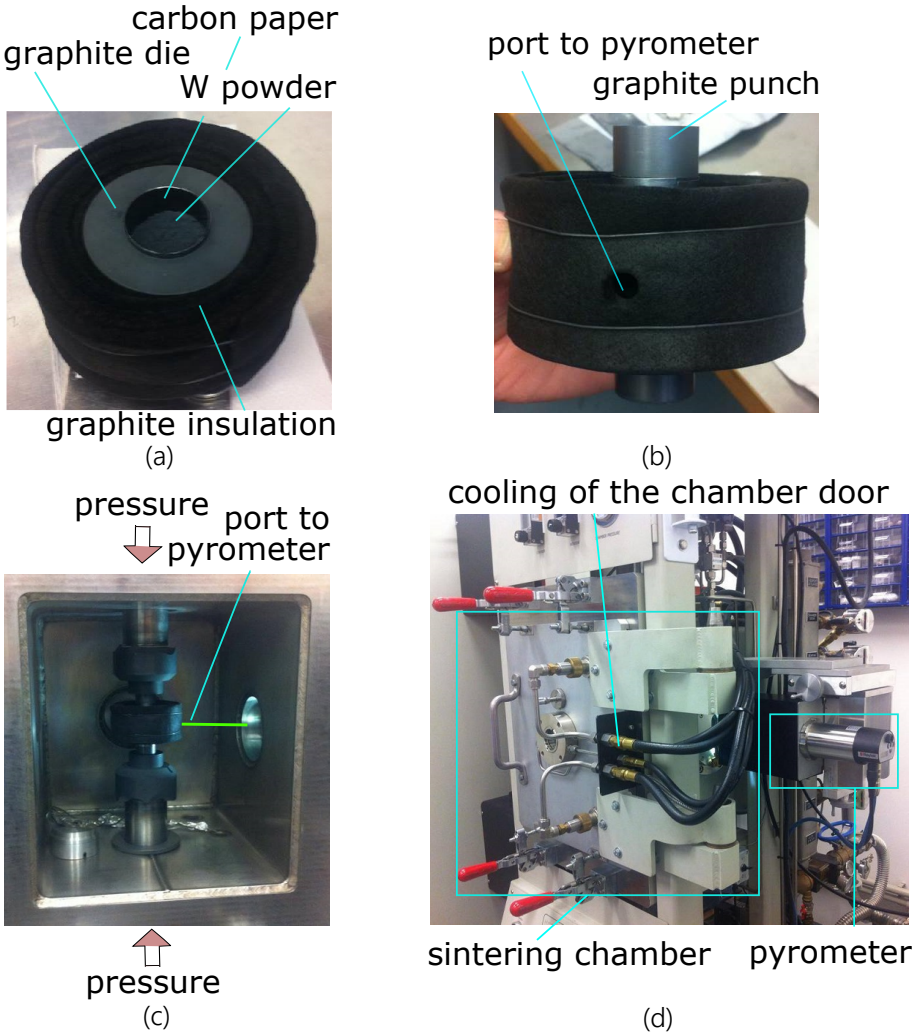

Figure 2.1: Sample preparation by SPS; (a) insertion of tungsten powder in the graphite die; (b) overview of the complete mould; (c) mould with powder installed within the sintering chamber; (d) overview of the sintering chamber.

- tungsten powder is enclosed within the graphite die (hollow cylinder) by two graphite punches; die is protected from a direct contact with the powder by a one-term use graphite foil,
- powder within the mould is pre-pressed manually in order to avoid mobilization of the powder within the sintering chamber,
- mould is installed in the chamber, ports to thermometers (in this case, pyrometer and thermocouple) are adjusted,

[2]Beranových 130, 199 05, Prague

- chamber is closed and vacuum is established (for sintering temperatures above 1800 °C, He protective atmosphere is used),
- pressure of 20 MPa is applied to align the aperture,
- pulsed DC current (with pulses of current ON of duration 80 ms and current OFF with duration 20 ms) is applied,
- sample is heated up to the predefined temperature, with a heating rate around 100 °C/min),
- full pressure is applied,
- pressure and temperature are applied for the preselected time interval,
- DC current is switched off, pressure is released, fabricated sample is cooled to ambient temperature.

Sample is prepared in a form of a disc of height of $\sim$ 3 mm and diameter $\sim$ 30 mm. Carbon and/or carbides are typically present (due to the diffusion of the carbon atoms from the protective carbon foil) on the surface and near-surface region of the sample.

Eight samples were prepared for the purpose of this work. Parameters of the sintering (temperature T, pressure p, sintering time t), together with the powder grain size (d_{powd}) are summarized in Tab. 2.1. Variation of all the sintering parameters shall result in collection of samples with variable grain size. Very large grains are expected for the sintering times of $t = 60$ min.

sample identification	T [°C]	p [MPa]	t [min]	d_{powd} [μm]
141023-1	2000	70	60	0.7
141022-1	2100	70	2	12
140731-1	1800	80	2	0.7
141023-2	2100	70	60	12
140801-1	1800	80	2	2
140805-1-u	2000	70	2	2
140805-2-u	2000	70	2	0.7
140805-2	2000	70	2	0.7

Table 2.1: Specification of the SPS parameters for preparation of the W-SPS samples with variable grain size ("-u" coding will be explained in Sec. 2.3).

Unfortunately due to the resistance of tungsten to chemical etching it was not possible to determine experimentally the as-prepared size of the grains. Successfulness of the variability of the grain size will be evaluated later. Nevertheless, in case of specimens 140731-1, 140801-1 and 140805-1-u, samples with exactly the same preparation parameters were prepared previously for the purpose of other experimental campaigns. Average grain size was determined by the circle method [93] at the fracture surfaces. The grain size for the respective samples was found

to be: $4.7 \pm 1.1, 3.7 \pm 1.0$ and 7.3 ± 2.1 μm. However, analysis with the circle method was rather difficult in case of samples 140801-1 and 140805-1-u since the GBs were not easily distinguishable. Pores of < 1 μm size were found within all three samples. Photographs of the fracture surfaces used for the grain size determination can be found on Fig. 2.2.

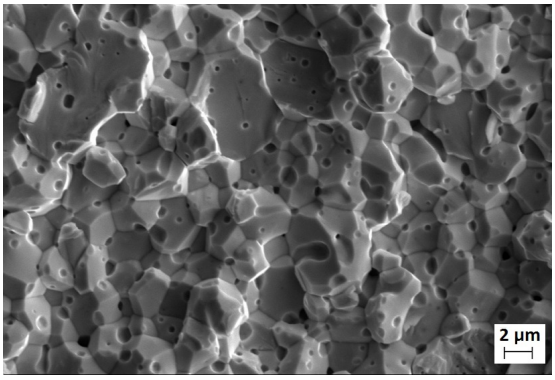

(a)

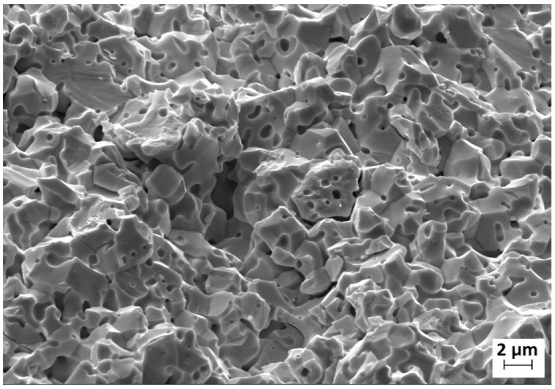

(b)

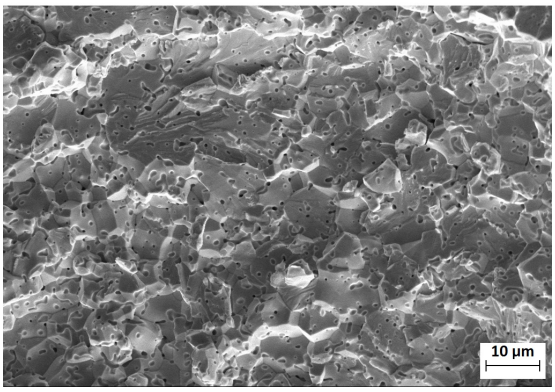

(c)

Figure 2.2: Photographs of fracture surfaces, obtained with a scanning electron microscope of samples prepared with same SPS parameters such as samples (a) 140731-1; (b) 140801-1; (c) 140805-1-u.

2.3 Exposition to simultaneous deuterium plasma and ELM-like heat fluxes at FZ-J

W-SPS samples underwent exposition to D-plasma and ELM-like transient loading at FZ-J. Description of the facility and exposure procedure follows.

2.3.1 Linear plasma generator PSI-2 & Nd:YAG laser

PSI-2

PSI-2 linear (meaning not-curved) device is a facility whose design was specialized to produce steady-state cylindrical plasma of parameters similar to those of edge plasmas of experimental fusion reactors. Beside PSI experiments, this facility provides possibility to investigate fundamental plasma properties, such as transport of the plasma species in the confined regime, passage from low to high density plasma regimes etc.

The device is schematically depicted on Fig. 2.4. Neutral gas (for example D_2, He, noble gases..) is injected into the vacuum vessel towards the cathode end via a gas inlet marked by blue star and labeled flow at source, f_s. Gas flow is measured by Mass Flow Controllers, MKS Instruments, and the flow value is given in standard cubic cm per second [sccm] unit. Additional mean of gas injection is via three gas inlets at the target chamber, denoted flow at chamber, f_{ch}. The set-up allows simultaneous injection of two different gases. Plasma is produced by an electrical current I (of values $100 - 1000$ A) that flows between a heated cathode and a grounded Mo anode (at a distance of about ~ 10 cm).

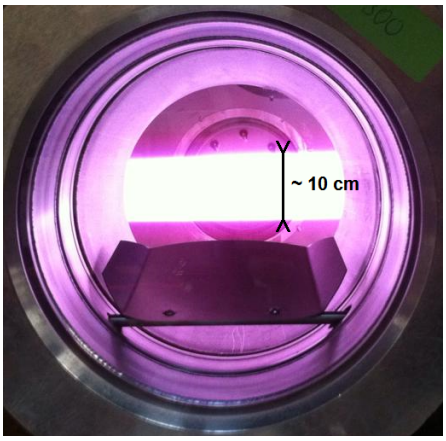

Figure 2.3: PSI-2 visible plasma column, as seen from one of the viewing ports (pure D-plasma).

Both cathode and anode have a cylindrical geometry, anode is of conical shape. Plasma is radially confined within an axial magnetic field of $B = 0.1$ T intensity. After leaving the anode bore, plasma streams along the magnetic field lines into a target chamber of length ~ 1.5 m where it either hits a neutralizer plate, or the metallic targets that are exposed to the plasma stream. Diameter of the visible plasma column is typically $D_{plasma} \sim 10$ cm, Fig. 2.3, but it can vary with the local intensity of the magnetic field.

Pressure of D_2 molecules, p_{D_2}, is measured by Pfeiffer Vacuum Sensor in the target chamber, distant ~ 0.6 m from plasma column, where T_{D_2} reaches approximately the ambient temperature, $T_{D_2} \sim 300$ K. The density of the D_2 molecules, n_{D_2}, can then be calculated using the ideal gas law,

$$p_{D_2} = n_{D_2} k_B T_{D_2}. \tag{2.1}$$

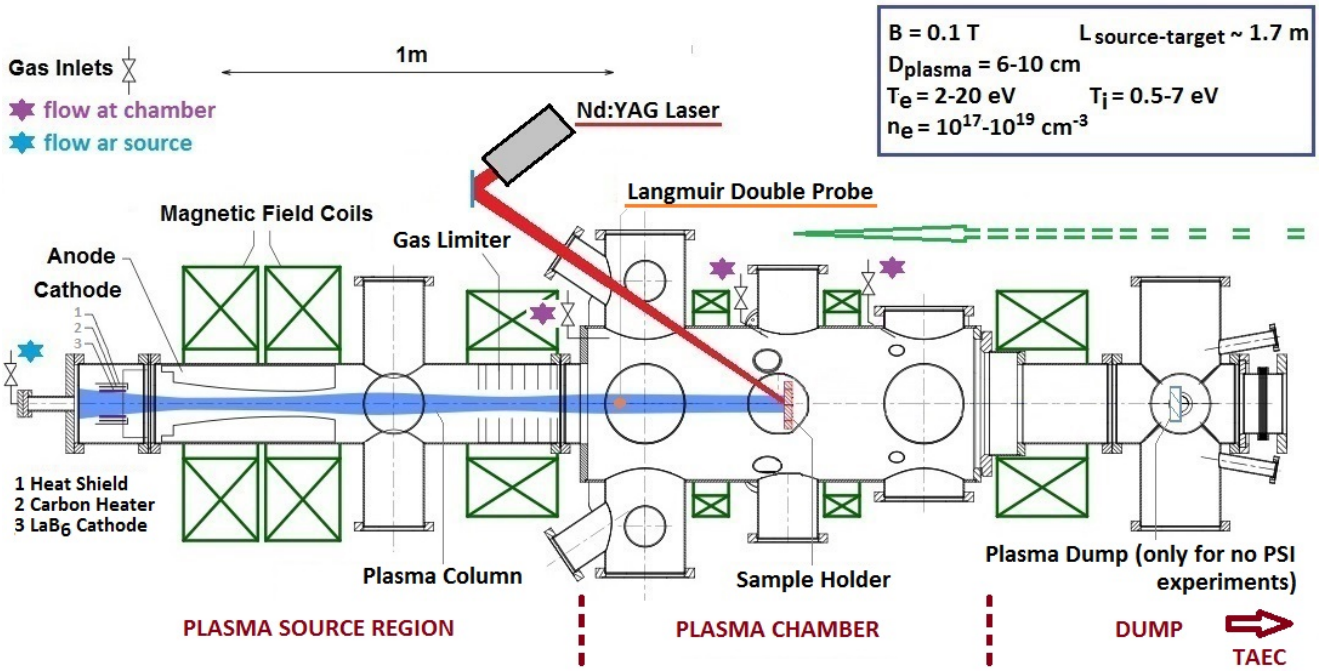

Figure 2.4: Schematic drawing of PSI-2 linear device [95] coupled with Nd:YAG laser. Typical plasma parameters are listed in the upper right corner.

It has been reported that typical radial profiles of plasma parameters are hollow [94]. Kreter et al. explained this by a hollow geometry of the LaB_6 cathode and by connection of anode and cathode via the magnetic field lines (for more details see [95]).
For correct interpretation of the PSI experiments, it is of ultimate importance to determine characteristics of the impacting plasma stream. In [96] properties of the PSI-2 D-plasma column were studied by means of high-resolution spectroscopy (with resolution $\sim$ 1 pm/pixel). No metallic targets were installed during the campaign, plasma was recombining in a plasma dump region (Fig. 2.4), on a target that was kept at a floating potential. Results presented in this thesis confirmed the previous findings [97]:

- gas injected in the plasma source region is not fully dissociated and ionized, plasma jet consists of two components: ionized and neutral, the latter being present mainly in the molecular form;

- along a pressure scan, with gradually increasing f_s and f_{ch}, temperature of the D^+ ions decreased from $\sim$ 7 eV down to $\sim$ 0.5 eV, temperature of the neutral component did not exceed $\sim$ 1 eV during the pressure scan;

- ions are *rotating* within the plasma column, with a maximum speed of $\sim$ 10 km/s for $f_s = 100$ sccm and $f_{ch} = 0$ sccm, movement of the neutrals is not affected by the magnetic field, they are transported along the plasma jet.

The degree of dissociation/ionization is not known. However, the larger the current at the plasma source, the more molecules of the injected gas are supposed to be dissociated and ionized within the source region. For $I = 150$ A, equality

$n_e = n_{D^+}$ is assumed. Electron density and temperature is measured in PSI-2 with the use of a Langmuir Double Probe (LDP, for detailed description of this probing system see [96]). Radial profiles of these plasma parameters for $I = 100$ A and $f_s = 100$ sccm are displayed on Fig. 2.5. Note that the maxima of the profiles are at ~ 3 cm. During the PSI experiments, exposed areas are placed in the vicinity of the maximum of the hollow profile. Due to the hollow profile of the parameters, plasma flux on the target (and on the spots that differ by the loading sequence, further explained in Sec. 2.3.2) lies in a certain range of values. Typically, for the PSI experiments, assuming $n_e = n_{D^+}$ and taking into account the speed of the ions to be ~ 10 km/s, the ion flux on the spots is between $2.5 - 4.0 \times 10^{21}$ m^2/s.

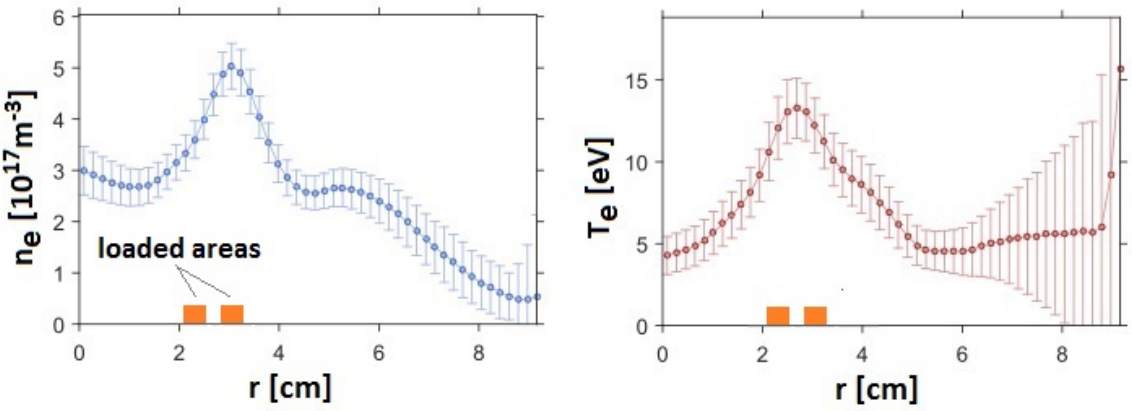

Figure 2.5: Electron density n_e (left) and temperature T_e (right) measured by LDP during D-plasma with settings $f_s = 100$ sccm and $I = 100$ A. Note the position of the loaded regions with respect to the maxima of the plasma parameters [96].

For $f_s = 100$ sccm, electron temperature does not exceed 15 eV, and that of ions 7 eV. However, situation is changed once a metallic target is installed for the purpose of the PSI experiments. Sample is typically electrically biased by voltage of maximum value 200 V. Energy of the incident ions is thus increased due their acceleration towards the target surface and their energy is given by the biasing voltage.

Finally, the role of the neutrals within the plasma jet shall be discussed. As was stated previously, neutral component is mainly present in the molecular form within the plasma jet and the temperature of the neutrals does not typically exceed ~ 1 eV and their speed is of the order of hundreds of m/s [96]. Compared with the energy of the ions, that is of the order of tenths of eV, their impacting energy is thus negligible. However they contribute to the plastic deformation of the material exposed to the D-plasma. Moreover, despite the fact that neutral component is mainly molecular, some part of the neutrals impact the target surface in atomic form. Once the target is heated above ~ 450 K, atoms can be adsorbed in the surface through chemisorption. Energy threshold for this process is about $E_{ch} \sim 0.5 - 0.8$ eV [85]. Adsorbed neutrals can then diffuse into the bulk and be possibly trapped in the lattice defects. Neutral component might thus in principle enhance the D retention within the irradiated samples. However, contribution of the neutrals to the overall D retention in PSI-2 has not been quantitatively evaluated yet.

Specimen to be exposed is mounted on an actively cooled copper support with an integrated plate for the ohmic heating. Through ohmic heating of this plate, various BT of the target can be set. Sample is then, together with dummy tungsten specimens, clamped to a Mo holder (see Fig. 2.6, left). Holder is then inserted into the PSI-2 target exchange and analysis chamber (TEAC) via a port not indicated on Fig. 2.4. Schematic drawing of PSI-2 with the TEAC chamber can be found for example in [98]. The whole target holder is then moved along the plasma axis (see the green arrow in Fig. 2.4) to its final position within the plasma chamber. Temperature of the sample is controlled by a thermocouple. An example of PSI experiment with D-plasma ON can be found on Fig. 2.6, right.

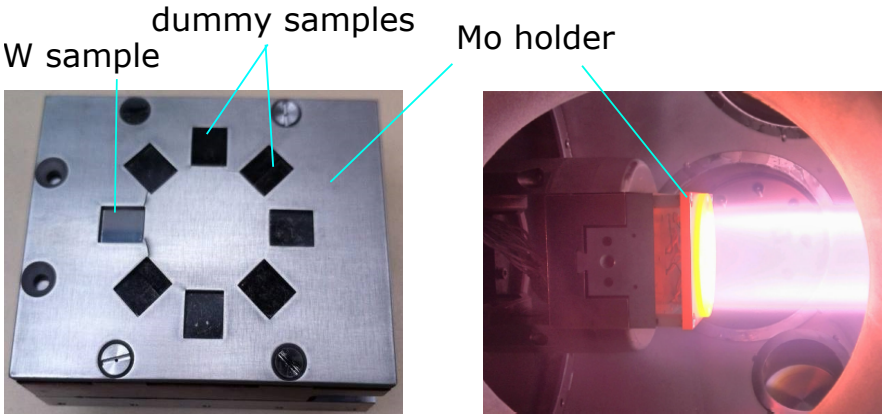

Figure 2.6: W sample mounted on a Mo holder, together with dummy samples (left); steady-state exposure of the sample to a D-plasma (right) [98].

Nd:YAG laser

ELM-like heat loads were produced with the use of a Nd:YAG laser operating at wavelength $\lambda = 1064$ nm, with a pulse duration $t_{pulse} = 1$ ms and maximum energy per pulse of $E = 32$ J. Laser beam is guided through an optical fibre just to the proximity of the PSI-2 window covering one of the ports. Beam is then focused on the exposition point with the use of focusing optical elements. Final shape of the exposed area is a circle of diameter ~ 3.0 mm. The power absorbed by the sample is calculated as:

$$P_{abs} = \frac{E}{t_{pulse}} \frac{T(1-R)}{S}, \tag{2.2}$$

where $S = 7.54$ mm^2 is the irradiated surface area, T is the transmittance of the optical elements and R is the reflectance of the target's surface. Transmission of the optical elements was measured with a photo diode and was found equal to $T = 88$ %. Same applies for the reflectance of the tungsten surface. Reflectance was found to be almost the same for before/after exposure tungsten surface and is thus assumed constant, of value $R = 60$ % [17]. Shape of the pulse is $\sim$ rectangular and the power deposited over the irradiated surface was found to be rather uniform (Fig. 2.7). During the experiment described in [90], surface temperature of the irradiated sample was measured with a pyrometer. For the highest absorbed power densities ($P_{abs} = 0.90$ GW/m^2) the temperature could

rise up to 1800 $°C$. Heated surface was cooled to its BT within few milliseconds (Fig. 2.7). Sample thus underwent cyclic thermal loading.

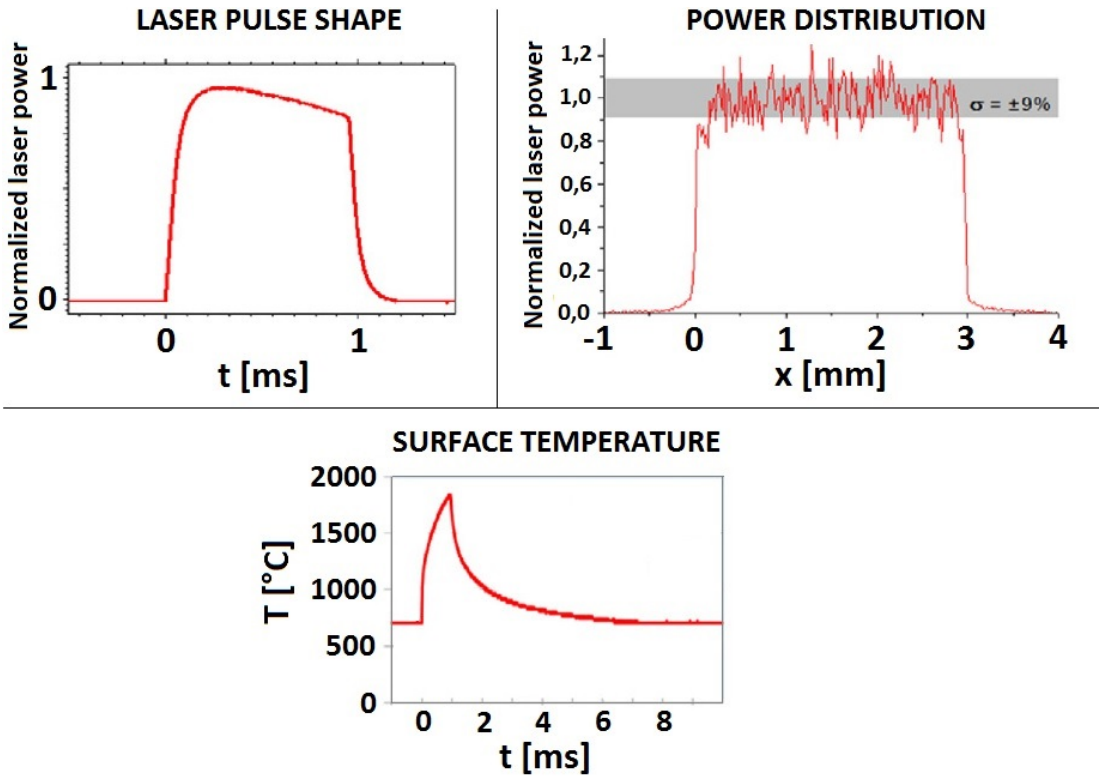

Figure 2.7: Nd:YAG laser pulse shape, power spatial distribution over the sample's surface and time evolution of the surface temperature of the sample during the irradiation by the laser beam. All graphs were taken from [89].

2.3.2 Description of exposition

As-prepared specimens fabricated by SPS must undergo a pre-exposure treatment in order to:

- fit with its dimensions into the Mo holder,
- remove regions where carbon or tungsten carbides could be diffused/formed and expose only areas with pure tungsten,
- provide a smooth surface for further reference and comparison with the unexposed state.

Carbon/carbide was thus removed with a use of a grinding wheel and samples were then cut into rectangles of dimensions $11 \times 11 \times 2$ mm^3. Surface was then ground with SiC abrasive papers of variable particle size (P120 up to P1200) and finally the surface was polished to a mirror finish with the help of a diamond paste of gradually decreasing particle size (from 6 to 1 μm). Pre-exposure roughness of $R_a < 0.1$ μm was achieved, R_a being the line arithmetic mean roughness factor. Two of the samples were only ground, not polished, in order to compare the response of the unpolished surface to the heat loading with that of the polished

samples. The two samples are marked by "-u" in their label, Tab. 2.1. Samples 140805-2-u and 140805-2 represent a pair of identical specimens, the only difference lies in the fact that one them was polished before the irradiation.

During previous experiments it was found that the damage threshold for ITER-grade tungsten is between $0.38 - 0.76$ GW/m^2 for samples exposed to 1000 heat pulses [90] (ELMs-relevant conditions). Power density to which the W-SPS were to be exposed should in principle exceed the damage threshold, so that the level of the surface damage would be evaluated and compared within the W-SPS samples set. It was thus decided to expose the specimens to $n = 100$ pulses of power density 0.76 GW/m^2 and pulse duration $t_{pulse} = 1$ ms. Nevertheless, such power density shall not lead to melting, since the F_{HF} in this case equals to:

$$F_{HF} = 24 \text{ MWm}^{-2}\text{s}^{1/2}, \tag{2.3}$$

which is not exceeding the melting limit given by Eq. 1.9. Energy of the laser was set accordingly to Eq. 2.2 to $E = 17.3$ J. Neutral gas flow was set to $f_s = 100$ sccm and the current at the plasma source to $I = 150$ A. Ion flux on the exposed areas was between $2.5 - 4.0 \times 10^{21}$ m^2/s. Tungsten target was biased by voltage of 60 V. Surface temperature was not monitored during the exposition, however one can expect it to exceed 1500 °C (and exceed thus probably the recrystallization temperature) during the transient loading, see the previous section. Frequency of the pulses was set to 0.5 Hz. In between the pulses, temperature of the samples could thus cool to the BT. In order to avoid appearance of large cracks that are related to the brittleness of tungsten at temperatures below its DBTT, BT was set to 400 °C by ohmic heating of the support and/or via impact of the plasma particles on the surface. All exposition parameters are summarized in Tab. 2.2.

f_s [sccm]	100
I [A]	150
E [J]	17.3
biasing voltage [V]	60
t_{pulse} [ms]	1
n	100
P_{abs} [GW/m^2]	0.76
F_{HF} [MWm^{-2}s$^{1/2}$]	24
BT [°C]	400
ion flux [$\times 10^{21}$ m^2/s]	2.5 - 4

Table 2.2: Exposition parameters.

During one exposition cycle, three distinct loading sequences (described in Sec. 2.1) were realised on the sample's surface. Moreover, one reference area, exposed just to the plasma stream, could be distinguished. Thus, four different "spots" can be recognised within the final pattern of the sample (Fig. 2.8). The exposition consists of three consecutive steps:

- **STEP 1** - Firstly, point labelled A was irradiated by 100 laser pulses solely.
- **STEP 2** - D-plasma was switched on and steady state was established. Point labelled B then underwent transient loading by the laser beam. Plasma was then switched off. Tungsten sample was fully immersed within the plasma jet, with the exposition points being located at the vicinity of the plasma parameters maxima. Navigation over the sample surface was realized with a help of an ordinary camera connected to a TV screen (Fig. 2.9). After this step was finished, *SPOT A* was completed, corresponding to the sequential loading by first laser beam and then D-plasma. *SPOT B* represents an area with simultaneous loading by both plasma and laser. The reference point, *SPOT r*, that underwent loading by only D-plasma, was obtained within this step as well.
- **STEP 3** - Finally, point C was irradiated by the laser beam. This finalized the exposition of *SPOT C*, that corresponds to sequential loading by first D-plasma and then by the laser beam.

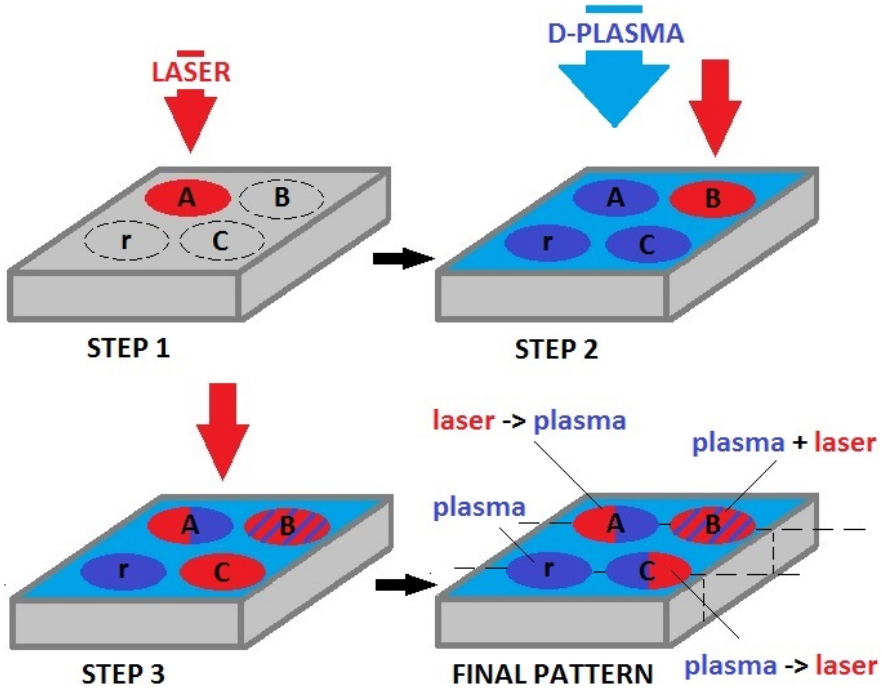

Figure 2.8: Illustration of **STEPS 1-3** of the exposition to D-plasma and laser pulses. *SPOTS A-C* and *SPOT r* are depicted on the lower-right part of the figure (meaning of dashed lines will be explained in Sec. 2.4.2)

.

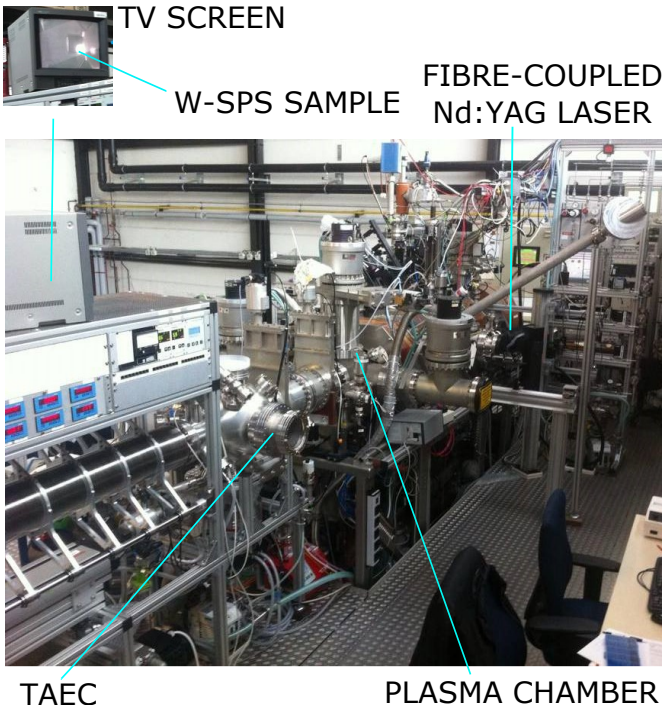

Figure 2.9: Overlook on the PSI-2 device, equipped with Nd:YAG laser.

Since PSI-2 can achieve steady state D-plasma, the overall fluence, f_{ions}, of ions (= number of ions that reach the target's surface [90]) is obtained by simple multiplication of the ion flux by the time that the plasma was switched on. Steady state control was possible through monitoring of the background pressure within the PSI-2 vessel. Pressure was measured in the source region, p_{source}, plasma chamber $p_{chamber}$ and at the dump, p_{dump}. Their steady state values are given for all samples in Tab. 2.3. In this table the total time during which the tungsten sample was exposed to D-plasma, t_{plasma}, is listed as well, together with the final fluences. Density of the neutral gas within the plasma chamber, $n_{D_2,chamber}$, calculated using Eq. 2.1, can be found in the table as well.

Density of the neutral gas during the steady state loading of the samples by D-plasma can be, based on the values listed in Tab. 2.3, considered the same for all the samples. However, sample 140805-1-u was immersed in the plasma jet slightly longer than the other samples, which might in principle result in larger fluence of the plasma species on it. This fact might be reflected in the amount of retained deuterium amounts within the sample.

Due to technological limits during the experiment, some of the *SPOTS* could not be obtained. Those exceptional cases are listed in Tab. 2.4.

After the samples exposure, complex post-mortem characterization was carried out with a range of methods, as will be described in the next sections.

2.4 Post-mortem material characterization - description of experimental methods

Post-mortem analysis of the irradiated samples was performed with use of several experimental methods. Of interest was examination of the damaged surfaces

sample identification	p_{source} [$\times 10^{-2}$ Pa]	$p_{chamber}$ [$\times 10^{-2}$ Pa]	p_{dump} [$\times 10^{-3}$ Pa]	$n_{D_2,chamber}$ [$\times 10^{19}$ m^{-3}]	t_{plasma} [min]	f_{ions} [$\times 10^{24}$ m^2]
141023-1	9.2	2.6	9.5	2.2	8	1.2 - 1.9
141022-1	9.4	2.5	9.7	2.3	7	1.1 - 1.7
140731-1	9.5	2.7	1.0	2.3	8	1.2 - 1.9
141023-2	9.8	2.6	1.0	2.4	8	1.2 - 1.9
140801-1	9.5	2.6	9.9	2.3	8	1.2 - 1.9
140805-1-u	9.6	2.6	9.8	2.3	9	1.4 - 2.2
140805-2-u	9.5	2.6	9.9	2.3	7	1.1 - 1.7
140805-2	9.5	2.6	9.8	2.3	7	1.1 - 1.7

Table 2.3: Summary of the loading conditions during the steady state loading of samples by D-plasma.

141023-1	141022-1	140731-1	141023-2	140801-1	140805-1-u	140805-2-u	140805-2
SPOTS A,B N.A.	SPOTS A,B N.A.	✓	✓	✓	✓	✓	✓

Table 2.4: Final recapitulation of exposition of W-SPS samples to simultaneous loading by D-plasma and ELM-like thermal shocks. Check mark indicates obtention of a full final pattern, e.a. of the *SPOTS A-C* and *SPOT r*.

by means of optical and electron metallography. Evaluation of the post-exposure grain size was possible with these techniques. Study of the morphological changes of the damaged surfaces revealed some interesting features of some of the irradiated surfaces. Those were further studied with the use of electron and atomic force microscopes and the near-surface layer in the cross-sectional view was investigated with the use of a focused gallium ion beam. Surface roughening, indicating the extent of plastic deformation, was compared within the specimen set by use of optical profilometry. Plastic deformation was further studied by means of electron microscopy. Size of the crystallites of all *SPOTS* within the specimens was determined by the X-ray diffraction analysis. This method also allowed to determine the samples microstrain. In-depths changes of the sample's structure could be examined by a cross-sectional metallography with the use of an electron microscope. Concentration of retained deuterium in the samples was determined by the elastic recoil detection analysis. Finally, changes of the mechanical properties, in particular of samples hardness, was studied by the Vickers microhardness test. The following sections will introduce all above mentioned experimental techniques together with the pre-examination sample preparation, if applicable.

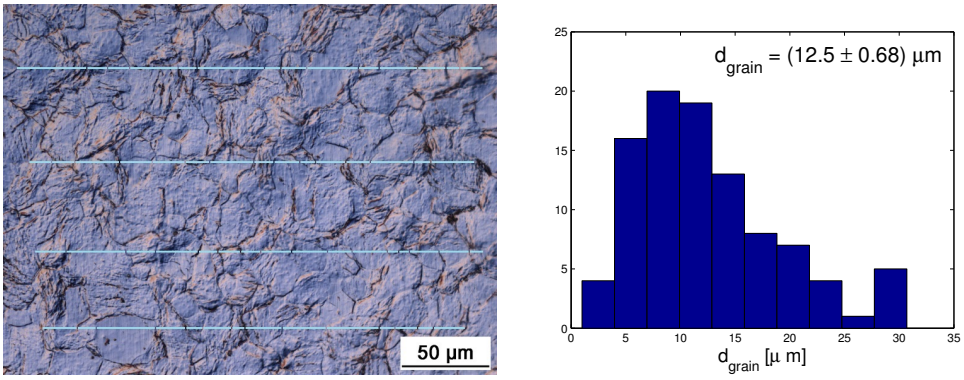

(a) (b)

Figure 2.10: (a) Determination of mean grain diameter via the intercept method; (b) histogram of obtained values (grain size in the upper right corner is reported in the form defined by Eq. 2.4). Example of sample 141023-1.

2.4.1 Surface optical metallography

Surface of the samples was examined by Olympus GX51 optical microscope at Department of Physics of Materials, Charles University (DPM CU[3]) without any polishing pre-treatment. Magnification of the microscope was set to 200x, 500x and in some cases to 1000x with a spatial calibration of $0.44, 0.18$ and 0.09 μm/pixel, respectively. In order to intensify the contrast between the particular topographical features, pictures were taken with the use of a Nomarski interference contrast [99].

As a consequence of irradiation, in case of polished surfaces, GBs could be clearly distinguished within the *SPOTS A-C*. Size of the grains was evaluated by the line intercept method. Principle of this method is straightforward. Several lines are drawn over the image of the surface. Every time the line intercepts a GB, an intercept is drawn. Taking into account the spatial calibration, mean length of the intercept (e.a. the mean grain diameter, d_{grain}) and its standard deviation are calculated. Assuming normal distribution of the intercept lengths, results are reported in the standardized form [100]:

$$x = \bar{x} \pm t_{1\sigma}(\nu)\frac{S_x}{\sqrt{n}}, \tag{2.4}$$

where $\bar{x}$ is the calculated mean value of the parameter x, S_x is its standard deviation, n is the number of repeated measurements of parameter x and $t_{1\sigma}(\nu)$ is a coefficient dependent on a degree of freedom of the measurement ν ($\nu = n-1$), evaluated for probability interval of $1\sigma = 0.6827$. For $n > 50$ (valid for all measurements), $t_{1\sigma}(\nu > 50) \simeq 1.0$. Data can be summarised for example in a histogram. Example of evaluation of the average grain diameter is given in Fig. 2.10.

2.4.2 Scanning electron microscopy, SEM

In general, resolution of a microscope is given by the wavelength of the probing species. Resolution better than that of optical microscopes is achieved when

[3]Ke Karlovu 5, 121 16, Prague 2

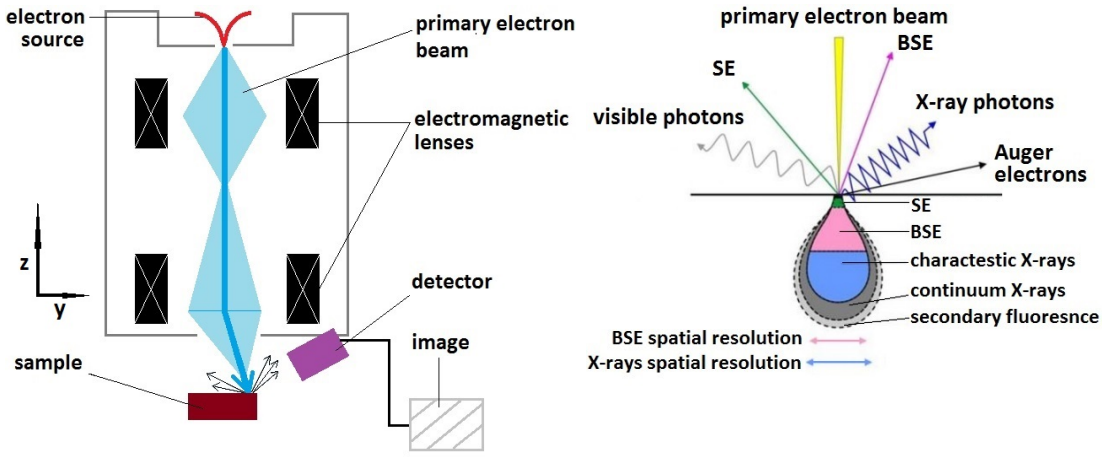

(a) (b)

Figure 2.11: (a) Schematic drawing of a SEM; (b) excitation volume of various electron-matter interaction products [102].

photons are replaced by electrons, since their wavelength, depending on the acceleration voltage, is lower than that of the visible light (typically by several orders of magnitude) [101] .

Principle of a scanning electron microscope, SEM, is illustrated on Fig. 2.11a. Electrons within a primary beam, emitted from the cathode (that can be either tungsten filament, LaB_6 crystal or a field emission gun, FEG), are accelerated towards an anode by application of a voltage of magnitude of several tenths of kV. Electrons are focused on a sample's surface with the help of electromagnetic lenses. Lenses are deflecting the beam along x and y axis, 'scanning' thus the investigated sample's surface. Various products of the electron-matter interaction are detected by the use of specialized detectors (see Fig. 2.11b). In the scope of this work only secondary electrons (SE) and back-scattered electrons (BSE) were detected.

SECONDARY ELECTRONS - electrons from the primary beam can lose their energy through inelastic collisions with electrons present in the sample's inner atomic shells. Electrons mobilized from these atomic shells can undergo further interactions until they, possibly, reach the surface and escape from the specimen. Energy of such secondary electrons does not typically exceed few tenths of eV. As a consequence of their low energy, electrons can escape only from the near-surface region (of depth of few nanometres, Fig. 2.11b), carrying thus information about the topography of the surface. More electrons can escape from the elevated/inclined formations such as small hills, droplets etc. in comparison with normal surfaces and in-depth regions such as cracks. This effect is responsible for the contrast that is observed when SE are detected.

BACK-SCATTERED ELECTRONS - electrons from the primary beam can also undergo elastic scattering and after several deviations of their direction of motion due to such collisions, they can be scattered back from the sample towards the dedicated detector. High-Z elements scatter electrons more than the low-Z elements, resulting in an apparent contrast in between two groups of elements

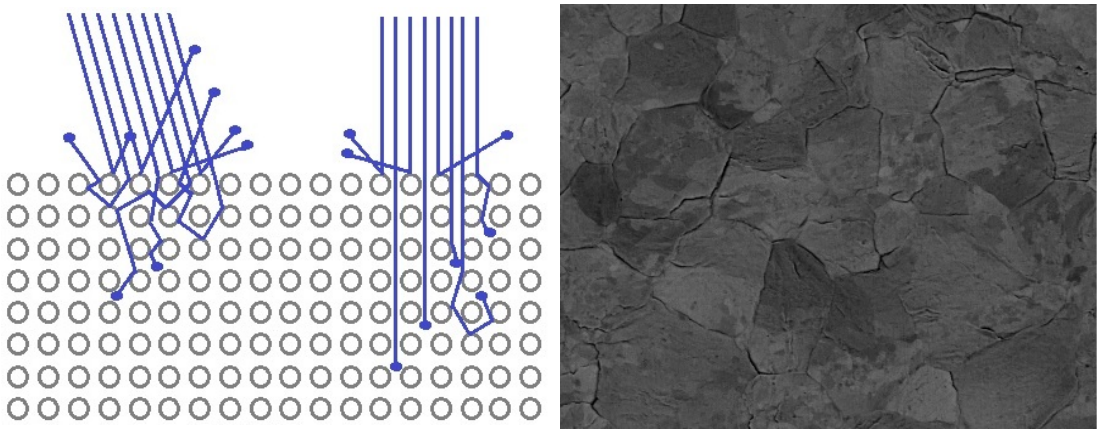

(a) (b)

Figure 2.12: (a) Illustration of ECCI principle; (b) example of the ECCI contrasting.

when present within one scanned region. BSE can thus serve to distinguish regions with different elemental composition. However, samples investigated in the scope of this work consisted of a single element (due to high purity of the powder used for their preparation), such analysis was thus not of interest in this context. Another information that BSE carry concerns the orientation of the crystallites and/or grains via the electron channelling contrast imaging (ECCI) and diffraction of the back-scattered electrons.

ECCI - this technique is based on dependence of the intensity of the BSE signal on the orientation of the crystal lattice with respect to the direction of the primary beam of electrons. Intensity of the signal can be given in relation to the deviation of the incident angle of the beam from the Bragg angle θ_B (see Sec. 2.4.6). For the case in which the primary beam is incident almost precisely under the θ_B, electrons penetrate deep into the crystal lattice without any pronounced interaction. This special case corresponds to the electron channelling [103]. With a proper adjustment of the optics (brightness, contrast etc.), it is thus possible to emphasize contrast between domains of different lattice orientation within the BSE image (Fig. 2.12a). Moreover, if the lattice contains defects, such as dislocations, those can be visualized with ECCI too. For example a dislocation present in a coherent lattice domain, oriented under the Bragg angle with respect to the primary beam, causes distortion of this coherency. Consequently, BSE signal is enhanced via electrons penetrating towards the surface through multiple scattering which causes the dislocation to appear as a brighter spot in the image.

EBSD, electron backscatter diffraction - electrons fulfilling the Bragg condition within particular crystal planes diffract and form the Kikuchi bands that are recorded on a screen located in the EBSD detector. The recorded pattern is defined by the lattice parameters (unique for every material) and besides other factors by the crystal's orientation. Number of Kikuchi bands is typically determined via a Hough transform, Miller indexes are assigned to the bands and the best fit for the crystal orientation is obtained. The latter is usually reported with the use of the Euler angles $(\varphi_1, \Phi, \varphi_2)$, i.e. set of rotations that brings one crystal's orientation into another one (typically a reference one of the EBSD detector). Angular resolution limit is usually about 0.5°. With EBSD not only

orientation of the particular region can be determined, but this technique can in general reveal information about the grain size, nature of the GBs, texture of the sample or identification of particular phases present in the specimen [104].

Surface metallography

Surface of the samples was examined by the electron microscope EVO MA 15 (Carl Zeiss SMT), at Institute of Plasma Physics of Czech Academy of Science (IPP CAS[4]), in SE and BSE modes, the latter with emphasis on ECCI. Accelerating voltage was set to 20 kV. Magnification was set to 500x, 2000x and 5000x with spatial calibration of $0.60, 0.15$ and 0.06 μm/pixel, respectively. Samples were observed as-irradiated.

EBSD analysis was performed at DPM CU, with the use of Quanta Fei 200 FEG microscope. Accelerating voltage was set to 15 or 20 kV. Photographs taken along the measurement were taken in both SE and BSE modes, at magnification of 1500x and 6000x, with spatial calibration of 0.18 and 0.04 μm/pixel, respectively. No sample pre-measurement treatment was made.

Cross-sectional metallography

In order to evaluate the near-surface and in-depth changes of the samples structure after their irradiation, samples were cut by a diamond cutting disc along the dashed lines depicted in Fig. 2.8. Cut pieces were fixed in Epofix resin and ground by SiC abrasive papers of variable particle sizes (P500 up to P4000). Surface was polished to a mirror finish with diamond paste of particle size of 1 μm. Finally, samples were polished by the OPS suspension (+ 30% H_2O_2) for 20 minutes. OPS suspension contains colloidal silicon of particle size 0.04 μm and its pH is about 9.8 (acidic). Use of the OPS provides both mechanical polishing and mild etching of the surface layer of the specimen.

Cross-sectional metallography was performed at IPP CAS, with the use of the EVO MA 15 (Carl Zeiss SMT) electron microscope. Accelerating voltage was set to 20 kV, magnification was set to 800x, 3000x and 5000x with spatial calibration of $0.38, 0.10$ and 0.06 μm/pixel, respectively. Photographs were taken in BSE mode with emphasis on ECCI.

2.4.3 Atomic force microscopy, AFM

Atomic force microscopy, AFM, together with other methods such as scanning tunnelling microscopy, magnetic force microscopy etc., belongs to the group of surface profiling methods, the so called scanning probe microscopic methods, that use a physical probe that scans the sample. In case of AFM, topography of the surface is acquired by simply measuring the deflection of the probe (= cantilever, ended by a sharp tip of surface that determines the method's resolution) during its movement along the sample surface. Typically, deflection is measured with the help of a laser beam, focused on the back of the cantilever. Reflected beam is detected by a photo diode, and the detection area is usually divided into several sections. Principle of measurement is illustrated in Fig. 2.13. Resolution of this

[4]Za Slovankou 1782/3, 182 00, Prague 8

profiling method in z-direction can be in principle of the order of picometers, however the actual resolution depends on the surface roughness.

Bruker Dimension Edge AFM located at DPM CU was used for the purpose of this thesis. Surface was scanned in the so called contact mode. In this working mode, the probe tip is in a direct contact with the surface. Moreover, a small amount of force is applied on it, so that the contact is made not with the surface atomic layers, but rather with the layers in the near surface region, so that the tip position is not distorted by the attractive atomic forces between the tip and surface atoms of the investigated sample. Deflection of the cantilever was kept constant during the measurement by a feedback loop [110]. OTESPA tip was used during this measurement, with a nominal radius of the tip of ~ 7 nm [111].

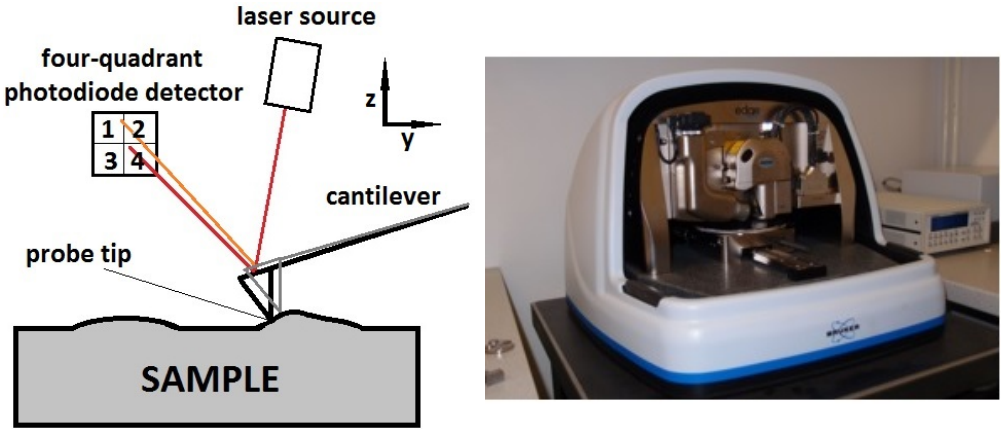

(a) (b)

Figure 2.13: (a) Principle of AFM profiling; (b) Bruker Dimension Edge AFM at DPM CU [110].

2.4.4 Focused ion beam analysis, FIB

Focused ion beam technique, FIB, is similar with its configuration to the SEM. However, instead of electrons, ions are accelerated and focused on the sample in order to extract the required information. Often, FIB is integrated within a SEM in order to use both electron and ion beams to investigate the specimen. At low ion beam currents, FIB can be used as an ion microscope, while in case of ion beams of high current, those can be used to sputter, or to 'mill' part of the specimen surface. Combined with a sample's proper inclination, electron beam can thus be used for cross-sectional imaging of the surface and near-surface specimen layers. SEM/FIB set-ups are often equipped with the so called Gas injection system (GIS), providing injection of gaseous precursors, that can be used for example for deposition of thin protective layers on the surface of the investigated area. Moreover, deposited layers can suppress formation of vertical stripes on the milled surfaces, referred to as 'curtaining' [112]. Beside the above mentioned applications, FIB can be used for example for preparation of thin foils for transmission electron microscopy, fabrication of micro-electro-mechanical systems etc.

FIB analysis was performed at IP CAS[5], using the Quanta Fei 3D dual beam

[5]U Slovanky 269/9, 182 00, Prague

SEM/FIB (Fig. 2.14a). This microscope uses for FIB the Ga^+ ion beam of diameter of ~ 10 nm with a possible range of accelerating voltage $2 - 30$ kV. Four different gaseous precursors can be used during the experiments - W, Pt, SiO_2 and I. Protective layers of Pt or W of thickness ~ 2 μm were deposited on the W-SPS specimen. In one case, no protective layer was deposited prior to milling by the ion beam. Experimental procedure consisted of the following steps: firstly, with the use of GIS a protective layer was deposited (if applicable) on the region of interest (ROI); secondly, the surface layer was milled by the gallium ion beam *around* the ROI up to depth of ~ 15 μm; finally, the ROI was milled by the ion beam up to same depth as the surrounding area. Photographs by SEM in the SE mode (with various magnifications) were taken during the milling of the ROI. ROI was typically a rectangle of dimensions $\sim 15 \times 20$ μm^2 (Fig. 2.14b) and the SEM images were taken after steps of length 1.0, 0.5 or 0.25 μm. The specimen was tilted by 52° with respect to the SEM detector, spatial calibration must be thus corrected by a multiplication factor of ~ 1.27. ROI was cleaned by methanol prior to the FIB analysis.

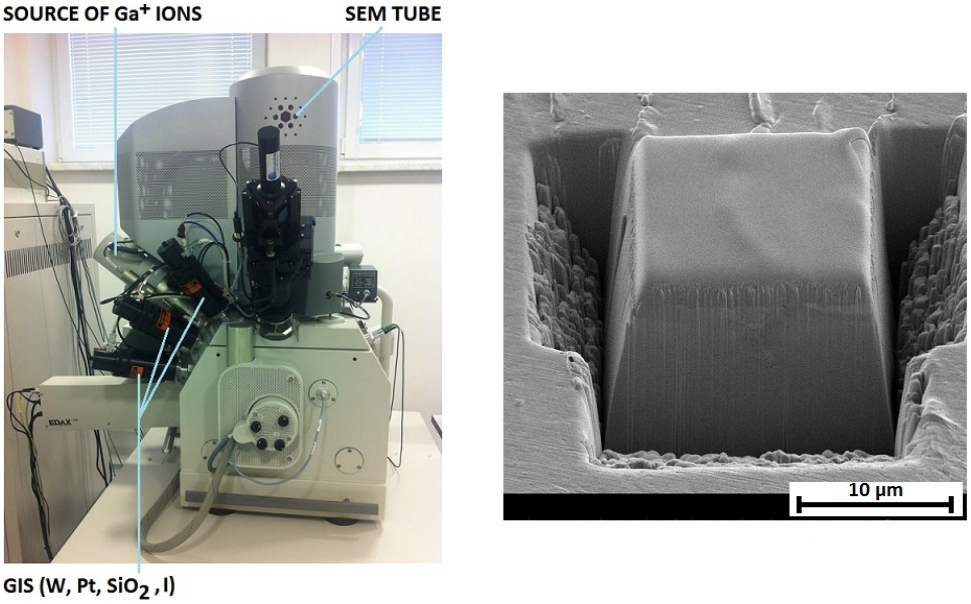

(a) (b)

Figure 2.14: (a) Quanta Fei 3D dual beam SEM/FIB, located at IP CAS; (b) example of FIB analysis of W-SPS sample.

2.4.5 Optical profilometry

For the purpose of surface roughness measurements, Zygo NewView 7200 optical profiler (Fig. 2.15a), installed at IPP CAS[6], was used. This profiler uses white light interferometry in order to scan the surface in a non-contact mode. White light produced by a LED Illuminator is guided towards an interferometric objective. Part of the light is reflected from a reference surfaces, embedded within the objective, other part reflects from the investigated sample surface,

[6]Sobotecká 1660, 511 01, Turnov

Fig. 2.15b. Both beams are then guided towards a camera. Resulting image consists of light and dark bands, carrying information about the surface topography. Those bands are a consequence of interference of the two light wavefronts [113]. Sample is scanned through a vertical movement of the objective with the use of a piezoelectric sensor and the final surface height map is obtained by recording intensity at each pixel. Vertical resolution of the profiler is < 0.1 nm and lateral resolution depends on the used objective. Data scan rate can be chosen to be ≤ 26 μm/s, and during the measurement was set to 10 or 20 μm/s.

Height maps were recorded for each as-exposed W-SPS sample with the use of two objectives of distinct magnifications:

- magnification 5x, area of tested surface 1.40×1.05 mm^2, lateral resolution of 9.5 μm;
- magnification 20x, area of tested surface 0.35×0.26 mm^2, lateral resolution of 1.3 μm.

The lower is the magnification, the larger area can be viewed by the objective and the data are thus covering larger surface area. However, the lower the magnification, the lower the lateral resolution of the measurement. Therefore, measurements were taken with the two above listed objectives. Data were averaged over four consecutive measurements.

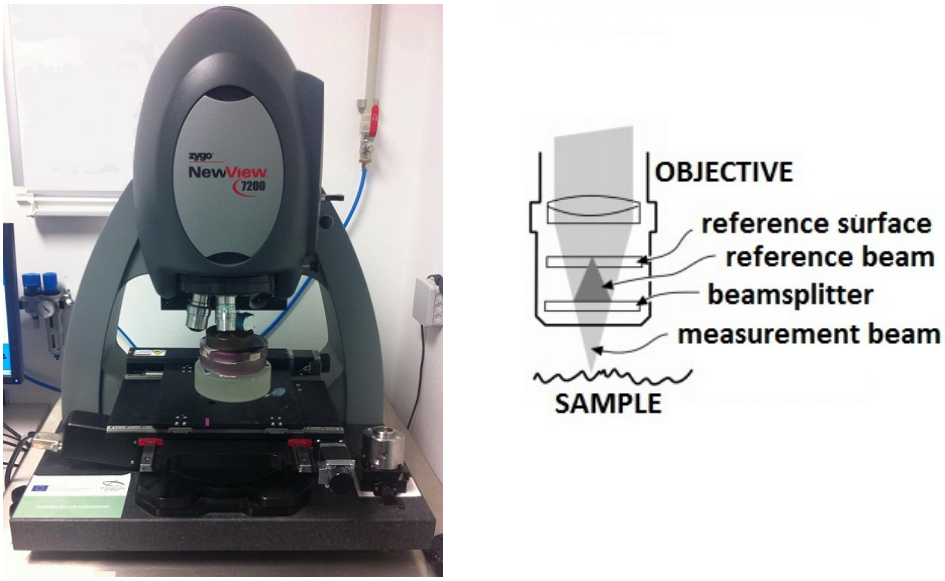

(a) (b)

Figure 2.15: (a) Zygo NewView 7200 profiler; (b) principle of roughness measurement [113].

Data were processed by a MetroPro software and the following values were given as an output of the measurements (together with a 3D picture of the surface):

- S_a, the surface average roughness:

$$S_a = \frac{1}{A} \iint\limits_{x,y} |z(x,y)| dxdy, \tag{2.5}$$

where $z(x, y)$ is the height of the surface and A is the area of the investigated sample surface;

- S_q, the surface root mean square roughness:

$$S_q = \frac{1}{A}\sqrt{\iint\limits_{x,y} (|z(x,y)|)^2 dxdy}. \tag{2.6}$$

Both parameters can be reported, however it is a custom to report S_a in case of machined surfaces.

2.4.6 X-ray diffraction, XRD

Comparable orders of magnitude of X-rays wavelength range ($0.1 - 100$ Å) with those of the typical inter-atomic distances in solid matter make of X-rays an ideal tool to study structure of a material. X-rays incident on a crystal scatter in all directions unless the Bragg condition is fulfilled (Fig. 2.16a):

$$n\lambda = 2d_{hkl}\sin(\theta). \tag{2.7}$$

where n refers to the diffraction order, λ is the wavelength of the X-ray waves, d_{hkl} is the inter-planar distance between planes within the crystal lattice indexed hkl and θ is the incident angle of the X-ray beam. In such case conditions for constructive interference are met, since fulfilment of Eq. 2.7 means, that the difference in path lengths between the two waves scattered at distinct hkl planes is equal to an integer (n) multiplied by the wavelength. Scanning of the θ angle with a X-ray source (and correspondingly, X-ray detector by 2θ, Fig. 2.16b) might serve for identification of phases within the sample, since a set of d_{hkl} is a material's characteristic property [105].

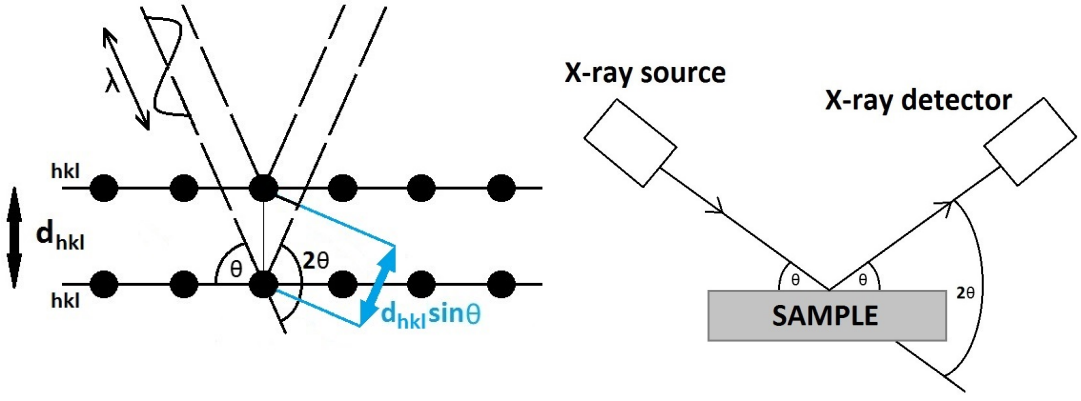

(a) (b)

Figure 2.16: (a) Diffraction of X-rays on crystal lattice planes; (b) $\theta - 2\theta$ scanning mode arrangement.

In an ideal θ-2θ scan the constructive interference reflection would appear as δ-function. However, in the real situation, the final interference pattern is broadened due to several broadening mechanisms: instrumental function of the

aperture, small size of the coherently diffracting domains (= crystallites) and microstrains. Lattice defects such as dislocations arrays (of small-angle boundaries), stacking faults, large-angle boundaries defining grains etc. might be responsible for breaking of the crystal into crystallites. Scherrer equation ([107]),

$$w_{cryst,FWHM}(2\theta) = \frac{k\lambda}{L\cos(\theta)}, \tag{2.8}$$

shows that the mean size of crystallites, L, is inversely proportional to the line width at half of its maximum intensity $w_{cryst,FWHM}$. Factor k in the Eq. 2.8 is the so called shape factor, whose value varies between 0.62 - 2.08 and depends on the actual crystallites shape. As a consequence of a plastic deformation, local variations in the inter-planar distances (due to appearance of dislocations, vacancies, interstitials etc.) can lead to broadening of the diffraction pattern as well. After removal of the external stresses causing the plastic deformation to occur, crystal lattice can be left in an elastically deformed state, i.e. contains a microstrain, ϵ. Level of microstrain can influence material's properties, such as fatigue strength, hardness or can be reflected in crack propagation along the specimen. Line broadening due to microstrain, $w_{microstrain}$, can be calculated via the following equation [108]:

$$w_{microstrain}(2\theta) = 4\epsilon\tan(\theta). \tag{2.9}$$

Diffraction peak is thus a convolution of instrumental $g(x)$ and physical $h(x)$ broadening, the latter given by the crystallite size and microstrain of the specimen. Background, B, must be typically subtracted from the measured data as well. The measured line profile $f(x)$ can be thus expressed as:

$$f(x) = g(x) \star h(x) + B, \tag{2.10}$$

where $\star$ denotes the convolution of the distinct broadening mechanisms. Various deconvolution methods were proposed for the analysis of the X-ray diffraction peaks [109].

Evaluation of the as-exposed W-SPS crystallite size and microstrain was done with the use of a Bruker D8 Discover X-ray diffractometer at IPP CAS (Fig. 2.17a). A Cu target was used as the source of the X-rays, in particular the K_α line ($\lambda_{K_\alpha} = 0.154$ nm). A Ni filter was used to reduce the intensity of the K_β line and the continuum radiation at the lowest wavelengths (Fig. 2.17b). Scanning angle step was set to 0.5° and the angle range was chosen to cover the most intense tungsten diffraction peaks, i.e. to $30 - 80°$.

TOPAS program was used for the analysis of the measured spectra. Diffractograms were fitted using the so called double-Voigt method [109], which assumes that both crystallite-size and microstrain shape of broadening can be described by a Voigt function, i.e. the convolution of a Gaussian and Lorentzian functions. Background was described by set of Chebychev polynomials. Shape factor k was set to value $k = 0.89$ which corresponds to assumption of spherical shape of the crystallites. As a result of the fitting routine (whose goodness was evaluated by the program), L and ϵ were obtained.

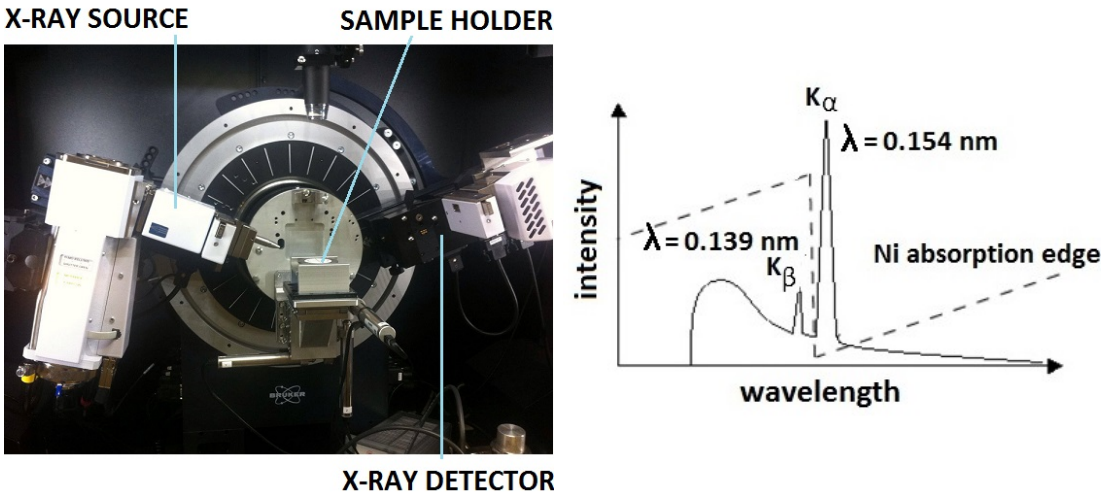

(a) (b)

Figure 2.17: (a) Bruker D8 Discover X-ray diffractometer (IPP CAS); (b) characteristic and continuum X-ray radiation of the Cu target [106]. Note the wavelength range of absorption of the Ni filter.

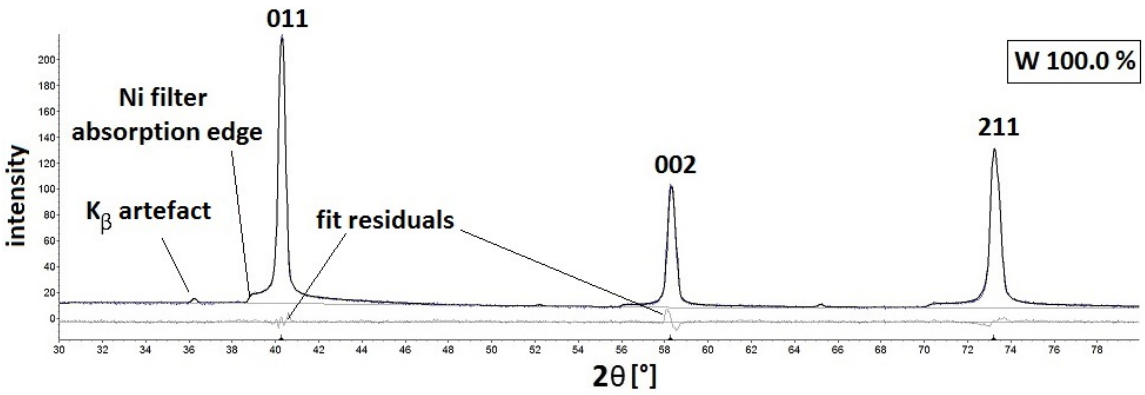

Figure 2.18: Example of a W-SPS diffractogram. Diffraction peaks are indexed accordingly (only pure W was found in the sample). Spectrum was fitted using the double-Voigt method, shown are the residuals of the fitting procedure.

.

2.4.7 Elastic recoil detection analysis, ERDA

Concentration of hydrogen isotopes within the PFCs can be deduced with the use of various experimental methods, such as thermal desorption spectroscopy, secondary ion mass spectroscopy etc. [115]. Amount of deuterium retained in the W-SPS samples was in the scope of this work deduced with the help of ERDA, elastic recoil detection analysis. Deuterium (and hydrogen) atoms where recoiled from the tested samples with an incident ion beam, in particular with the He^{2+} ions. Such configuration, when heavier atoms cause lighter atoms to recoil from the sample, represents a characteristic feature of the ERDA method. Schematic drawing depicted on Fig. 2.19 illustrates the principle of the technique. Heavy projectile, in this case, He^{2+} ion, of mass M and incident energy E_0 scatters elastically from the target atom of mass m ($m < M$). Incident atom is scattered under angle θ, with kinetic energy E_s, while the recoiled atom leaves the sample

with energy E_r, under angle Φ. With the validity of conservation laws for the total kinetic energy and momentum, the energies of scattered and recoiled atoms are given by [118]:

$$E_s = (\frac{M\cos(\theta) + \sqrt{m^2 - M^2\sin^2(\theta)}}{M+m})^2 E_0 = (1-k)E_0, \tag{2.11}$$

$$E_r = \frac{4Mm\cos^2(\Phi)}{(M+m)^2} E_0 = kE_0, \tag{2.12}$$

where k represents the recoil kinematic factor. However, target atoms can be recoiled from the near-surface layers as well. Atoms passing through the material lose their energy via collisions with nucleus or electrons within the atomic shell of the atoms present in the specimen. Energy loss $\mathrm{d}E$ per unit path length $\mathrm{d}x$ can be expressed in terms of a stopping power, S,

$$S = -\left(\frac{\mathrm{d}E}{\mathrm{d}x}\right). \tag{2.13}$$

Energy of the recoiled atom at the moment of its detection within the detector, E_{det} equals kE_0 in case of atoms recoiling from the surface layer. E_{det} of atom recoiled from the near-surface layer depends on the distance z, depth in which the atom was originally present:

$$E_{det} = k[E_0 - \underbrace{S_{He^{2+}}(E_0)z/\sin(\alpha)}_{\Delta E_{in,s}}] - \underbrace{S_r(E_r)z/\sin(\beta)}_{\Delta E_{out,r}}. \tag{2.14}$$

Factors $z/\sin(\alpha)$ and $z/\sin(\beta)$ represent distances travelled by the incident ion and recoiled atom within the sample, respectively (Fig. 2.19). Typically, maximum depth profiling of deuterium atoms does not exceed 100 nm significantly.

In order to detect exclusively the atoms of interest in the detector (i.e. hydrogen and deuterium), the so called stopping foil is introduced into the experimental configuration. Ions from the incident beam, scattered in the direction of the detector, shall dissipate their energy within the foil completely. Energy of the recoiled atoms is reduced as a consequence of the passage through the foil. A typical ERDA spectrum can be found on Fig. 2.20, in which two detecting areas can be distinguished: surface layer of few tenths of nanometers and the bulk region within the sample. Usually, the sensitivity of ERDA technique is about at.%0.1.

ERDA measurements were done at Nuclear Physics Institute of Czech Academy of Science, NPI CAS[7]. ERDA detector is located at one of the beam lines of the Tandetron 4130 MC accelerator (Figs. 2.22,2.21). This device is able to produce ion beams of large variety of elements, of energy between 400 keV to 24 MeV. As an ion source two kinds of devices can be used - either a duoplasmaptron or a Cs sputter ion source. He^+ ions are mainly produced within the duoplasmatron, in which the ions from the neutral He gas are obtained via ionization by electrons, that are emitted from a heated filament. The second source is able to produce atomic or molecular ions through sputtering of a solid target by Cs^+ ions.

[7]Hlavní 130, 250 68, Řež

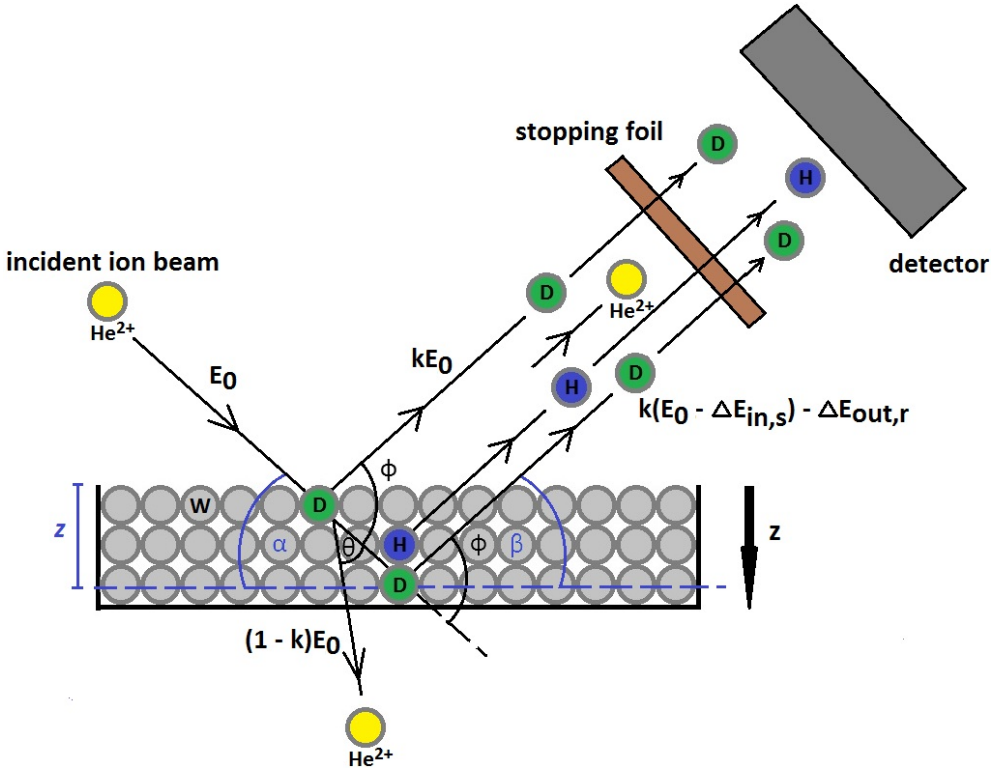

Figure 2.19: Principle or ERDA measurement.

.

Negative ions must be fed into the accelerator chamber. Tandetron accelerates ions during a two-stage, tandem, process. Negative ions are at first accelerated by a positive high voltage. Within the high voltage region negative ions lose their electrons within a gas stripper and becomes n-times positively charged. Positive ions are accelerated towards grounded high energy accelerator base, representing the second stage of the acceleration process [116]. Once fully accelerated, ions are deflected towards the desired beam line by a deflecting magnet. Along the path of ions towards the target sample, beam properties are controlled through set of electromagnetic lenses, diaphragms etc. Diameter of the incident He^{2+} beam when impacting on the target is ~ 1.2 mm.

Cross-section for forward recoil of deuterium atoms by helium ions is maximised for $E_0 = 2.14$ MeV and the scattering angle $\alpha = 20°$. However, due to the thickness of the stopping foil (see below) and the required depth profiling (rather low in case of the above mentioned energy), the energy of the helium ions was set to $E_0 = 2.60$ MeV. ERDA detector (a Si diode detector, distant from the sample surface by $\sim$ 9 cm) was located at the angle corresponding to the recoil angle $\Phi = 25°$ [119]. Recoiled surface deuterium atoms have under such arrangement energy $E_{r,D} = 1.554$ MeV, for hydrogen atoms $E_{r,H} = 1.121$ MeV, Eq. 2.12. As a stopping foil a 12.9 μm Mylar (biaxially-oriented polyethylene terephthalate, BoPET [120]) foil was used. Detected energy after passage through the Mylar foil was for deuterium surface atoms $E_{det,D} \sim 660$ keV, for hydrogen atoms $E_{det,H} \sim 430$ keV. Detection limit is about 10^{15} atoms/cm^2.

Measured data were evaluated with Plochy2 software, developed by RNDr.

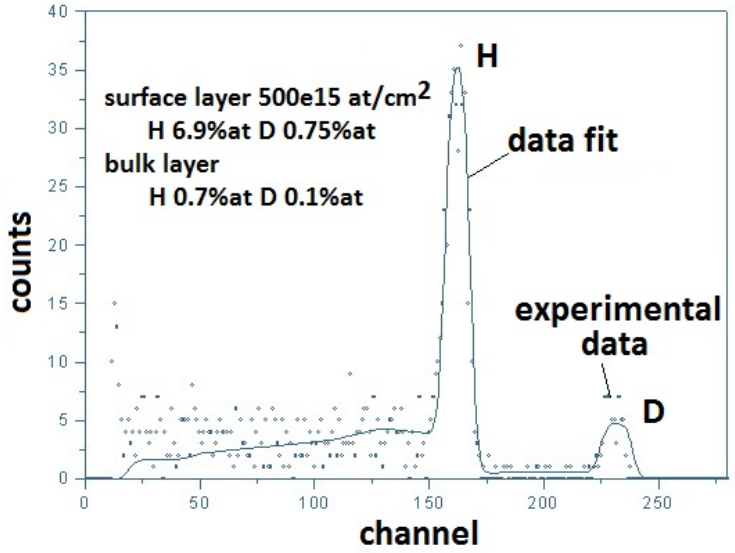

Figure 2.20: ERDA spectrum of a reference sample (prepared by diffusion of D_2O into a polyimid), measured at NPI CAS [117].

.

Vladimír Havránek, CSc.[8]. Cross-section and stopping power data from the dedicated sources are included in the software. Experimental data were fitted by a theoretical curve, input data for the fit consisted of number or layers within the sample, number of elements present in it, identification of the elements and thickness of the layers. Roughness of the sample surface, that might in principle lead to broadening of the measured peaks, was not taken into account. Output of the fitting routine consists of areal density (in 10^{15} atoms/cm^2) of hydrogen and deuterium atoms. Contents of hydrogen and deuterium are reported for two distinct layers: surface layer and bulk layer, the latter ranging in depth of $z = (50 - 90)$ nm.

ERDA measurement was performed on as-exposed W-SPS samples 16 days after their exposure to D-plasma and transient thermal shocks.

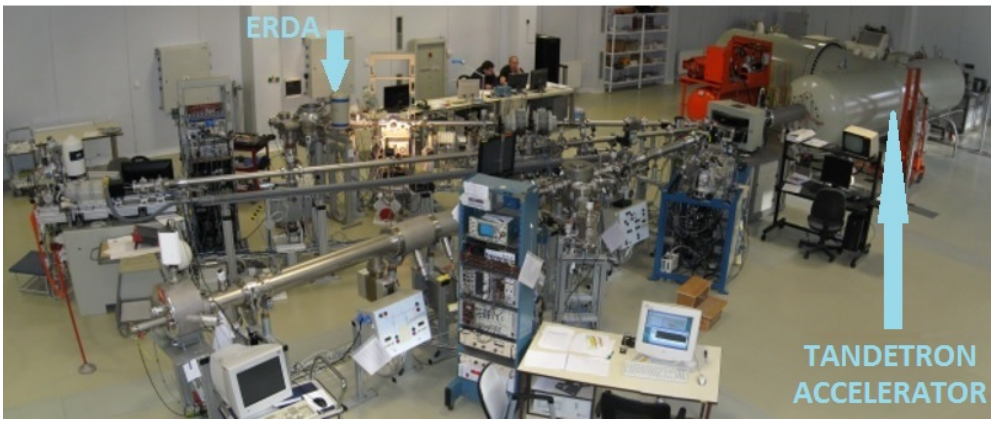

Figure 2.21: Tandetron laboratory [118].

.

[8]havranek@ujf.cas.cs

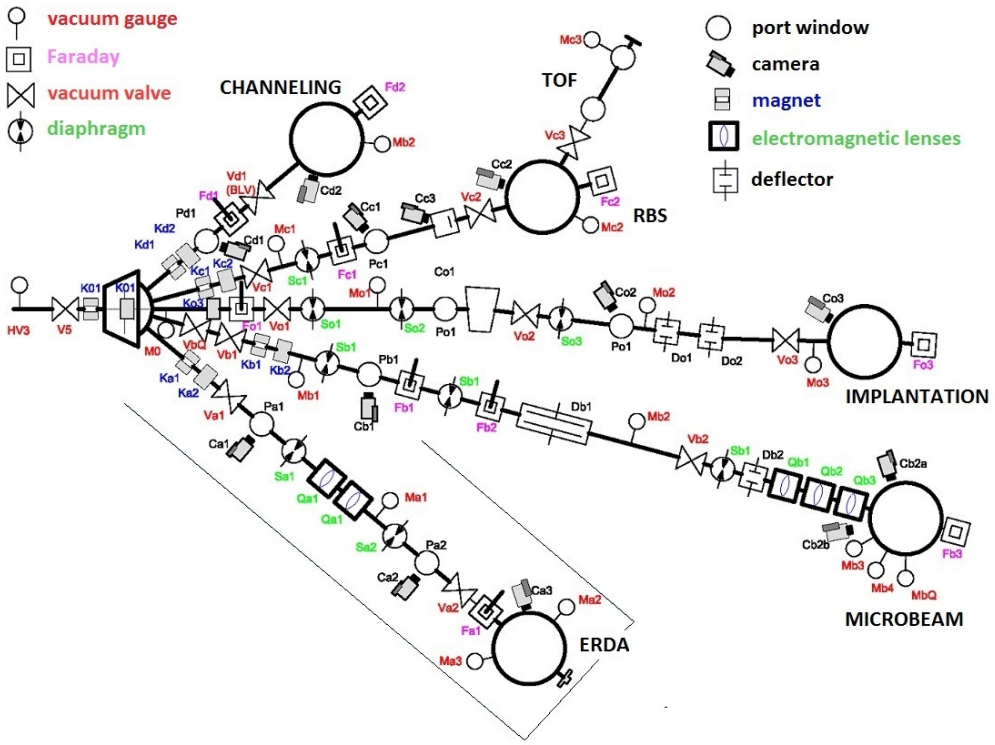

Figure 2.22: Schematic overview of Tandetron, with distinct beam lines for different experimental methods. Beam line for ERDA is emphasized by the black bordering. With courtesy of Vladimír Semián.

.

2.4.8 Vickers microhardness

Hardness of a material can be defined as its resistance against local deformation. In case that a force of $\sim 0.098 - 9.8$ N (equivalent to $1 - 1000$ g) is applied on a sample, the so called microhardness can be determined. Vickers microhardness test consists of impressing a diamond indenter (of well defined geometry, pyramidally shaped with squared base, see Fig. 2.23a) into the surface of the tested sample. Both time of the indentation and the force applied on the specimen define the parameters of the test. After indentation, a small pit in the shape of the indentor is left within the sample surface layer. Surface area of the indentation spot can be calculated in the following way [114]:

$$A = \frac{d^2}{2\sin(136°/2)} \simeq \frac{d^2}{1.854}, \tag{2.15}$$

where d is a mean of the diagonal lengths d_1 and d_2 of the indentation squared spot. Vickers microhardness (number HV) is given by the ratio F/A where F is the force applied on the sample:

$$HV = \frac{F}{A} = \frac{1.854F}{d^2}. \tag{2.16}$$

Units of HV are given in kgf/mm^2, where kgf represents a kilogram-force unit, a gravitational metric unit of force. One can express the HV in SI units by multiplying it by 9.80665 m/s^2 [114]. Vickers hardness is usually reported as

$xHVy$, where x indicated the measured Vickers number and y is the load applied on the sample.

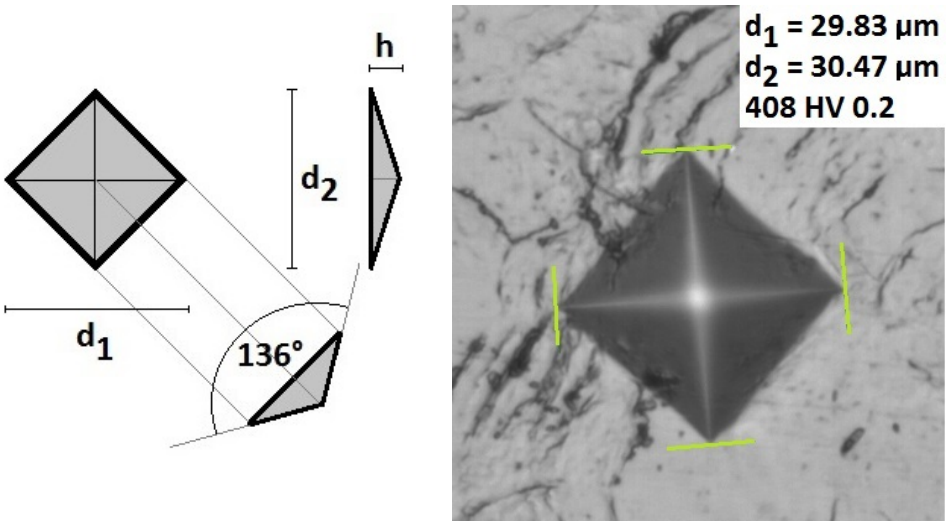

(a) (b)

Figure 2.23: (a) Geometry of the Vickers microhardness indentor; (b) example of an indentation during the Vickers test.

Measurements of HV were done at DPM CU, with the use of a microhardness tester QNESS A10+. Time of indentation was set to 10 s and the applied load equalled to $F = 0.1$ kgf. In order to reduce uncertainty of the result, tested region was indented ten times (with indentation spacing set to 0.2 μm) and the HV number was evaluated automatically by the software QPix Control, which gives also as a part of the output file the standard deviation of the Vickers number. Samples were investigated in the as-exposed state.

2.5 Results and discussion

In the following section, the extent of damage of the irradiated W-SPS samples and its features will be examined by various analytical methods within the specimen set. Results of the post-mortem analysis will be correlated, if possible, with the parameter varied within the specimen set, i.e. the grain diameter, d_{grain}.

Comparison of the damage will be discussed in a context of four different sample/$SPOT$ sets:

- differing by loading sequences, therefore in between the set of $SPOTS$ on particular W-SPS specimens,
- within the W-SPS set, i.e. within the set of polished specimens of variable grain size,
- difference between polished and unpolished samples (140805-2 and 140805-2-u),
- resistance to damage of unpolished samples differing by grain size (140805-1-u and 140805-2-u).

At the end of each subsection, brief summary of the most important information deduced within the particular part will be given.

2.5.1 Determination of post-irradiation grain size

Due to the resistance of tungsten to chemical etching, it was not possible to determine the as-prepared grain size of the W-SPS samples. However, it was assumed that due to the variation of the SPS fabrication parameters, a set of samples with variable d_{grain} shall be obtained. As a consequence of sample irradiation by D-plasma and transient heat pulses, GBs were distinguishable in case of polished surfaces, and the post-irradiation grain size could be determined with the help of the line intercept method, described in Sec. 2.4.1. Results of analysis are summarized in Tab. 2.5, full set of histograms can be found in the Attachments.

Standard deviation of the d_{grain} exceeds in all cases 40 % of the mean value of the grain size, indicating rather dispersed distribution of the intercepts lengths. Moreover, the intercept length distribution is apparently skewed (coarse skewed, in all cases [121]), reporting thus the results in a form given by Eq. 2.4 is not completely correct, since in case of skewed distributions rather the median of values shall be reported, not the mean. However, for the purpose of this paper, skewness of the grain size distribution is omitted. Grain diameter of samples 140731-1 and 140801-1 exceeds that deduced on the as-prepared fracture surfaces. Surface temperature during the irradiation thus probably exceeded the recrystallization temperature of the W-SPS samples. In case of samples 1410731-1, 141023-2 and 140801-1 the largest grains are located in the frame of SPOT B. In principle this might mean that during the simultaneous exposition to laser beam and D-plasma (loading sequence b), Sec. 2.1) the surface temperature was higher than during the two other loading sequences, which might promote enhanced grain growth in comparison with the sequences a) and c) (with no D-plasma on during the exposure). However, this trend is not confirmed in case of sample 140805-2.

For better orientation, W-SPS samples set will be from now on labelled by a new set of identification numbers. Specimens will be numbered by gradually increasing grain diameter. New encoding is listed in Tab. 2.6. Grain size of a particular sample is, if applicable, calculated as an average over d_{grain} of the three *SPOTS*. Those will be encoded by "-A", "-B" or "-C", correspondingly. For example, *SPOT* B on sample 140731-1 will be further labelled as 1-A. Since samples 140805-2 and 140805-2-u differ solely by the state of the surface before the exposure, d_{grain} is assumed to be the same for those samples, their encoding will thus be as follows: 3 and 3-u. Finally, it was not possible to deduce post-irradiation d_{grain}. However, of interest is a comparison of results of post-mortem analysis of this unpolished sample with the second unpolished sample, 3-u. Based on the fabrication parameters applied to those two samples, Tab. 2.1, sample 140805-1-u was prepared with larger powder grain size than that of sample 3-u. It can be thus assumed that the as-prepared grain size of this sample is larger. Sample will be thus labelled 7-u, in which this fact is reflected naturally ($7 > 3$).

Based on the values listed in the two previous tables, it can be finally confirmed that a set of tungsten samples with gradually increasing grain size was prepared by SPS method (Fig. 2.24). Grain sizes do not overlap in the 1σ range within the W-SPS set.

sample identification	*SPOT*	d_{grain} [μm]	$d_{grain,frac.surf}$ [μm]
141023-1	A	-	-
	B	-	
	C	12.50 ± 0.68	-
141022-1	A	-	-
	B	-	-
	C	9.35 ± 0.54	-
140731-1	A	4.27 ± 0.21	-
	B	7.82 ± 0.35	4.7 ± 1.1
	C	4.44 ± 0.19	-
141023-2	A	50.1 ± 3.3	-
	B	50.8 ± 3.5	-
	C	47.9 ± 3.7	-
140801-1	A	6.26 ± 0.37	-
	B	7.06 ± 0.45	3.7 ± 1.0
	C	6.61 ± 0.32	-
140805-1-u	A	-	-
	B	-	7.4 ± 2.1
	C	-	-
140805-2-u	A	-	-
	B	-	-
	C	-	-
140805-2	A	8.58 ± 0.53	-
	B	7.58 ± 0.37	-
	C	8.36 ± 0.47	-

Table 2.5: Post-irradiation grain size, d_{grain}, determined by the line intercept method. GBs were distinguishable only on polished surfaces, on *SPOTS A-C*. Grain diameters, deduced by circle method on fracture surfaces $d_{grain,frac.surf}$, are, if available (Fig. 2.2), included in the last column.

sample identification	$d_{grain,mean}$ [μm]	new sample identification
141023-1	12.50 ± 0.68	5
141022-1	9.35 ± 0.54	4
140731-1	5.51 ± 0.25	1
141023-2	49.6 ± 3.5	6
140801-1	6.64 ± 0.38	2
140805-1-u	-	7-u
140805-2-u	- (8.17 ± 0.46)	3-u
140805-2	8.17 ± 0.46	3

Table 2.6: New encoding of W-SPS sample set. Ordering is following the gradually increasing post-irradiation grain diameter. Question mark indicates the fact that grain size by line intercept method could not be determined in case of unpolished surfaces.

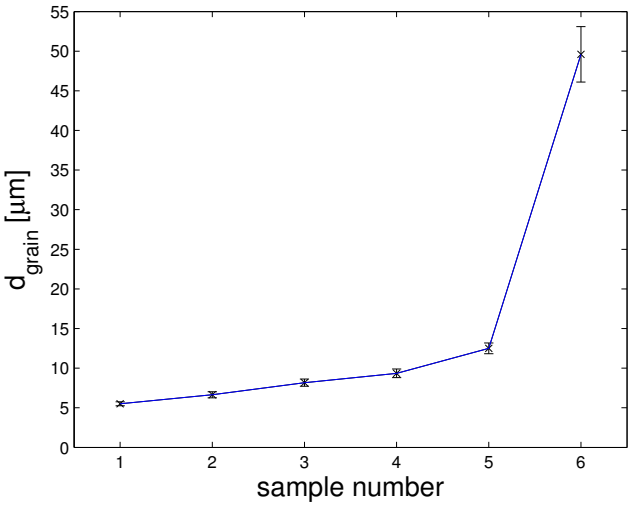

Figure 2.24: Gradually increasing grain diameter within the W-SPS specimen set.

.

Recapitulation of results

- When applicable, grain diameter was deduced by the line intercept method.
- It was confirmed that a set of specimens with variable grain size was fabricated by SPS.
- New encoding was given to the samples, following the gradually increasing grain diameter.
- No generally valid trend, concerning the grain size, was found for the *SPOTS* within the W-SPS sample set. However, increased grain size within *SPOTS B* in some of the samples might indicate larger surface temperature during the loading sequence b), enhancing thus grain recrystallization.

2.5.2 Morphology of irradiated surfaces

Optical metallography

Not only grain size could be determined by inspecting the photographs of surface taken by the optical microscope. Also first information concerning the surface as-irradiated morphology could be retrieved.

Firstly, reference surfaces (*SPOTS-r*) can be compared within the W-SPS sample set, Fig. 2.25. Polygonal structures are recognizable on otherwise polished surfaces in case of samples #1-6. Diameter of those structures increases gradually with the d_{grain} and their dimensions correspond to the average grain size determined for the particular samples. In principle, those structures might be associated to the porous nature of the SPS samples, however it was shown previously that for the range of the fabrication parameters used for the W-SPS set, size of the pores is typically < 1 μm. Rather than pores the grains of the material are responsible for the relief appearance. Material was thus probably plastically deformed under the impact of the D-plasma species, which would correspond to a typical damage caused by the plasma particles of energy of the order of tenths of eV, described in Sec. 1.3.3. Relaxation of the stresses caused by the supersaturation of the above-surface region was probably realized through slight slip of material along the GBs. No cracks were developed on the reference *SPOTS*. Unpolished surfaces show clearly a network of straight grooves within the surface layer, as expected. Polygonal structures are not visible on the unpolished surfaces. No apparent difference can be obtained from the comparison of reference surfaces of samples 3-u and 7-u.

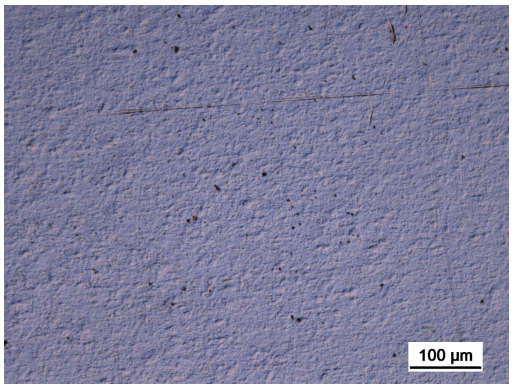

(a) 1-r

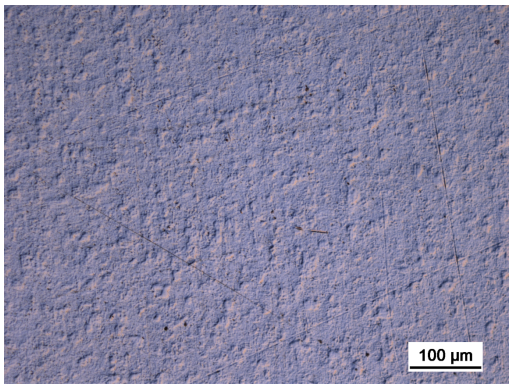

(b) 2-r

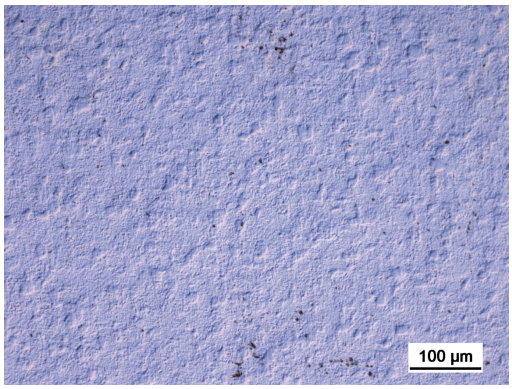

(c) 3-r

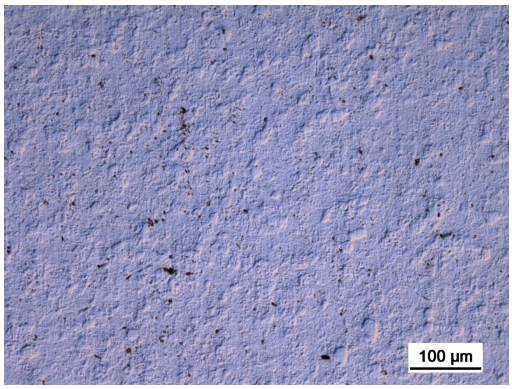

(d) 4-r

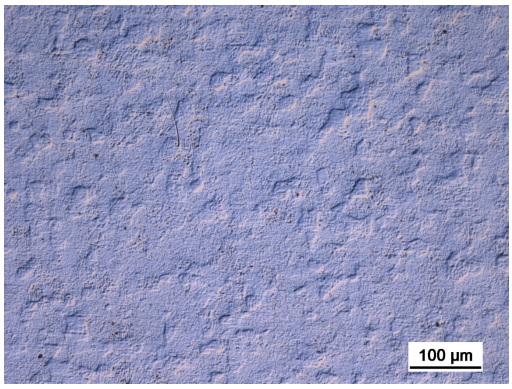

(e) 5-r

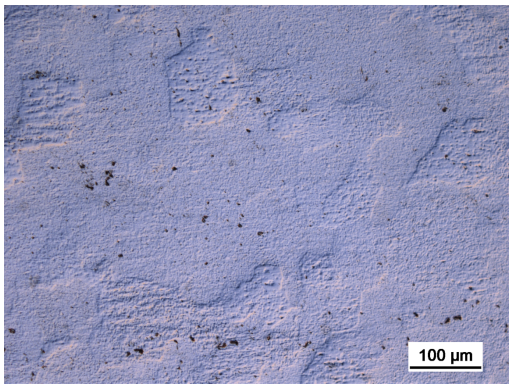

(f) 6-r

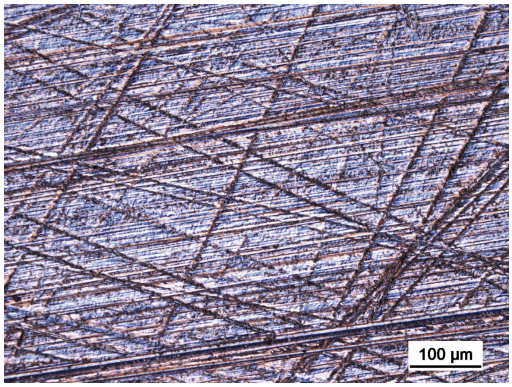

(g) 3-u-r

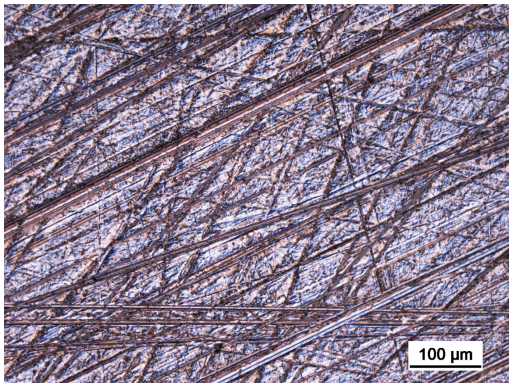

(h) 7-u-r

Figure 2.25: Photographs of surfaces of *SPOTS-r* of all W-SPS samples.

Full set of photographs of *SPOTS A-C* of the W-SPS samples can be found in Attachments. Comparison of damaged polished surfaces within the *SPOTS* sets yields no significant influence of loading sequence on the subsequent features of the damaged areas. The only difference lies in grain size for the respective *SPOTS*, as listed in Tab. 2.5.

Since no apparent dependence on the loading sequence was found in case of polished surfaces, a representative figure (of *SPOT A/B/C*) was chosen for each sample surface and the complete set of photographs is given in Fig. 2.26.

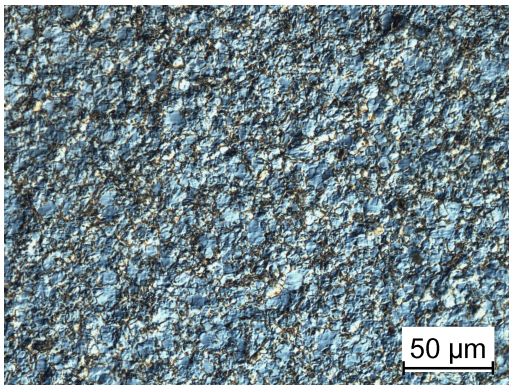

(a) 1-A

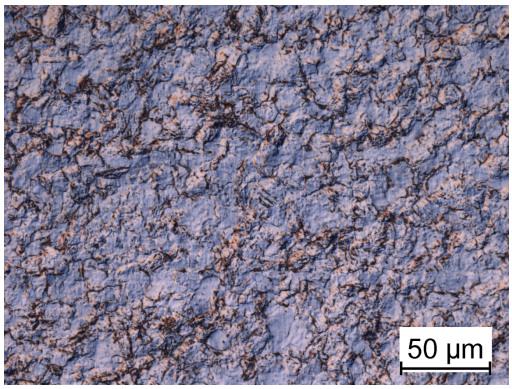

(b) 2-C

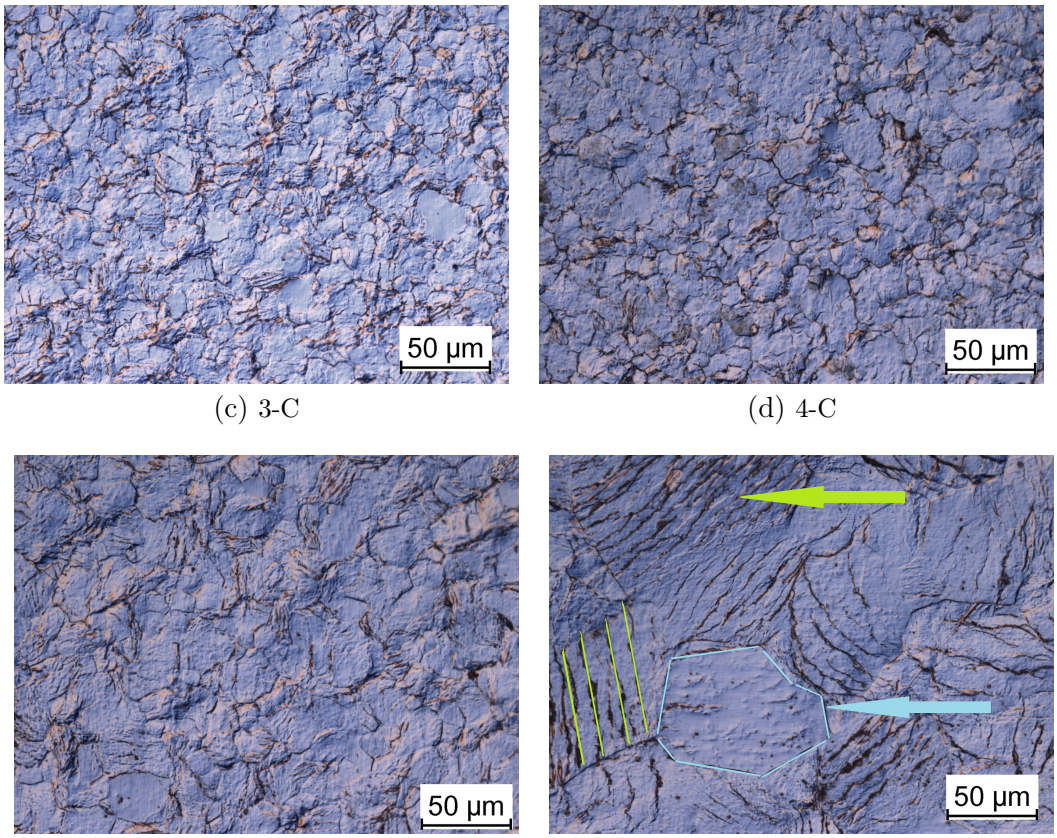

(c) 3-C (d) 4-C

(e) 5-C (f) 6-A

Figure 2.26: Photographs of surfaces of representative *SPOTS* of the polished W-SPS samples. Note the roughly symmetrical stripes (ridges) within the individual grains (green lines and arrow, example of sample #6). Beside grains with such structure, stripes-free grains are present in the sample surface layer (blue lines and arrow, example of sample #6).

Beside apparent plastic deformation and a probable slip of the grains along GBs, starting from sample #2 (with possible exception of sample #4) a certain symmetrical *in-grain* structure, in form of parallel stripes (ridges), can be recognised within some of the grains. Largest concentration of grains with such structure appears for sample #6. Topographical features of the damaged surfaces deserve further study by means of SEM in the SE mode, applying larger magnification of the imaging.

In comparison with sample #3, besides a rather week appearance of GBs a crack network across the sample surface was developed in case of unpolished sample #3-u. Direction of the crack propagation seems to be at first sight rather random. This is a common feature of both unpolished samples, of all loading sequences, *SPOTS A-C*, Fig. 2.27. Residual grooves within the surface layer must have thus serve as crack nucleation sites. However, in case of *SPOT B*, the crack concentration is decreased in both cases (nearly suppressed in case of 7-u). Since changes in surface morphology appear to be same in case of *SPOTS A, C*, it is more likely that this effect is a consequence of a different surface temperature during the simultaneous exposure to D-plasma and transient heat loads. Suppression of crack formation is typically associated with a base temperature of the sample exceeding its DBTT. No major cracks have been observed so far on the polished

surfaces, which might lead to conclusion, that with $BT = 400$ °C this condition was fulfilled.

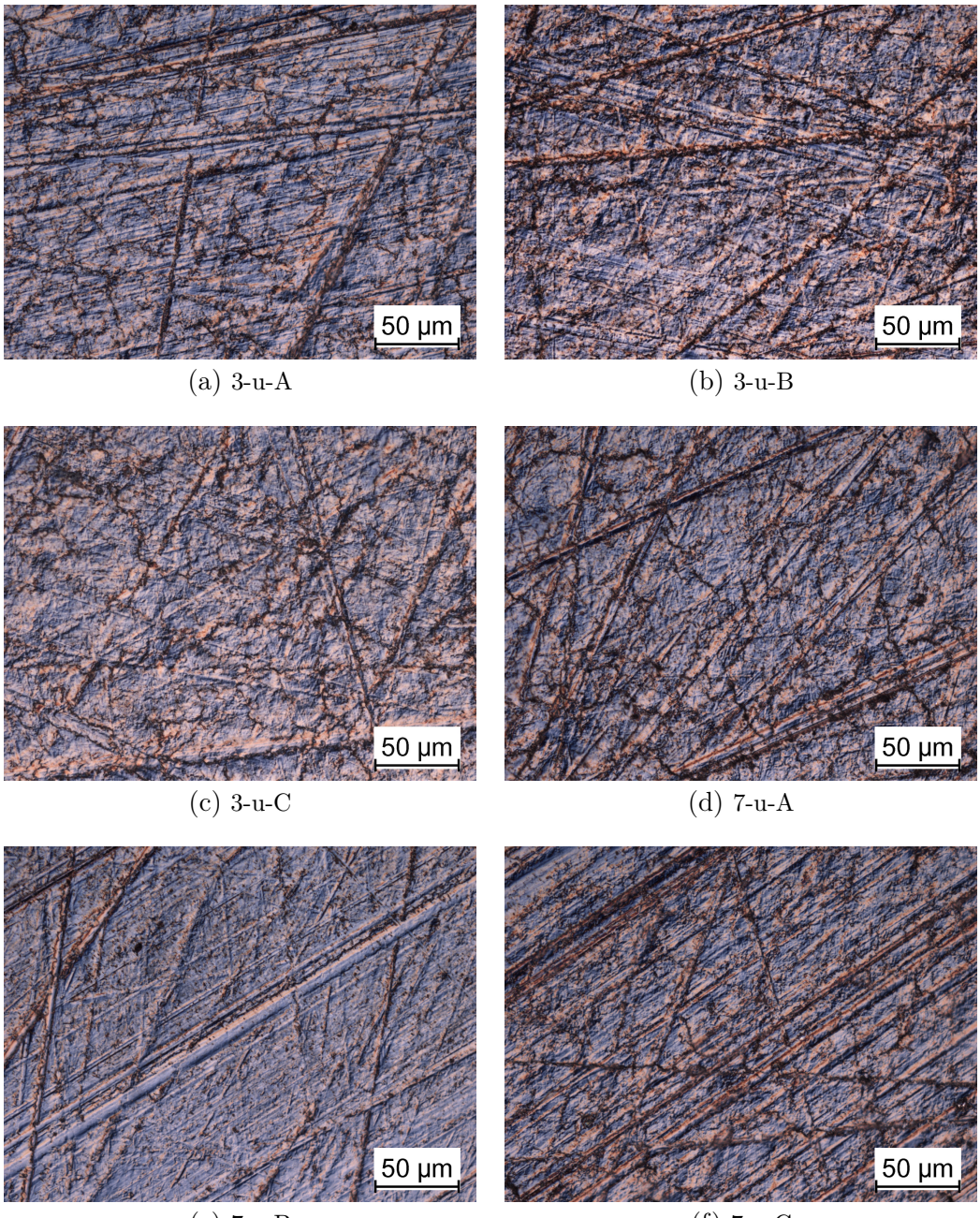

(a) 3-u-A (b) 3-u-B

(c) 3-u-C (d) 7-u-A

(e) 7-u-B (f) 7-u-C

Figure 2.27: Photographs of *SPOTS A-C* of the unpolished W-SPS samples. Crack width does not, in case of both samples, exceed ~ 2 μm. Length of cracks exceeds 100 μm in some cases.

.

SEM metallography (SE mode)

In order to study post-irradiation changes in surface morphology in further details, topographical features of the damaged surfaces of all *SPOTS* of W-SPS samples were examined by the means of SEM, in SE mode. Full set of photographs can be found in the Attachments.

On first sight, no apparent differences in between the particular loading sequences are recognizable on the surfaces of polished samples. However, in case of sample #1, *SPOT A*, cracks of submicron width surrounding the grains can be found, while no cracks are found on *SPOTS B, C*. This might indicate degradation of mechanical properties as a consequence of irradiation by transient pulses. Surface layer, with, probably, recrystallized grains might thus be more vulnerable to plastic deformation when loaded by D-plasma. No cracks in *SPOT C* indicate that level of recovery during the D-plasma loading does not decrease the tensile strength of the material to such extent that cracks would be formed during the subsequent transient loading by laser. Similar conclusion might be retrieved for simultaneous loading by plasma and laser pulses. Lack of blisters (see Sec. 2.1) on all *SPOTS* and samples indicates no embrittlement of material by deuterium impact.

Since no difference in between the loading sequences was found in case of polished samples (beside the above mentioned exception of sample #1), representative photograph of the surface was chosen for each specimen, see Fig. 2.29. Firstly, it is confirmed that in case of samples #1 and #4 no ridges-like structures are present on the surface. On the other hand, these are the only two samples in which cracks are present. It seems that two types of stress relaxation processes can be realized during the transient loading - via roughening and eventually cracking *or* in-grain ridges-like structure formation. Closer look on the in-grain ridges (for example Fig.2.28f) reveals that they consist of apparently lowered and elevated material. The latter, due to its rather rounded nature, appears to be molten. Which relaxation process will be dominant under transient loading might firstly appear rather unsystematic, since no clear dependence on grain size can be followed. However, certain information can be obtained from the comparison of fabrication parameters of samples #4 and #6. Those differ solely by the sintering time (2 and 60 minutes, respectively, Tab. 2.1). Longer sintering time resulted in this case in larger grain growth, by a factor of ~ 5. At the same time, powder inter-grain diffusion took place for a longer time, enhancing thus the bounds between neighbouring grains. Weaker bounds between grains might in principle enhance crack formation in between them. The ridges-like structure appears only inside the individual grains, this structure does not propagate in the neighbouring grain (Fig. 2.28g) Another interesting information can be gained from comparison of fabrication parameters of samples #1 and #2. Both samples were prepared at temperature 1800 °C, which is the lowest temperature used during the preparation of the W-SPS sample set. It has been shown previously, that the lower the sintering temperature, the less are the original powder grains interconnected through bounds due to reduced atomic diffusion (resulting in a porous structure of the final specimen). It can be thus assumed, that the powder inter-grain diffusion was the lowest in case of these two samples, resulting thus in week bounds in between the grains. However, the samples differ by original powder grain size. This was larger in case of sample #2. Certain dependence on the grain size of the final SPS product can be thus assumed. Cracks within the surface layer were observed during previous experiments (see Chap. 2), however the ridges-like structure has not been reported yet. Those will be further studied in the next section.

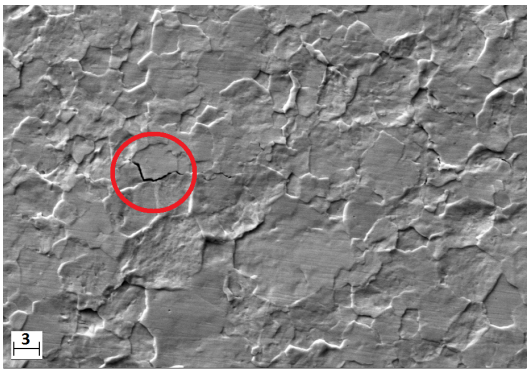

(a) 1-A (note the encircled crack)

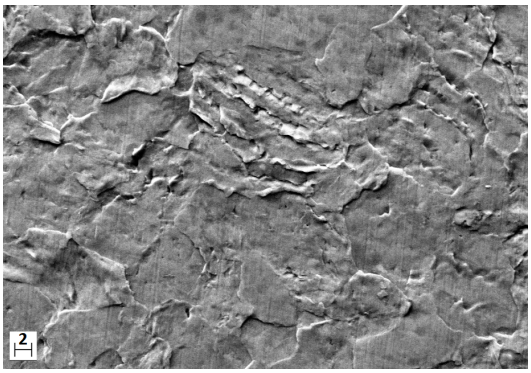

(b) 2-A

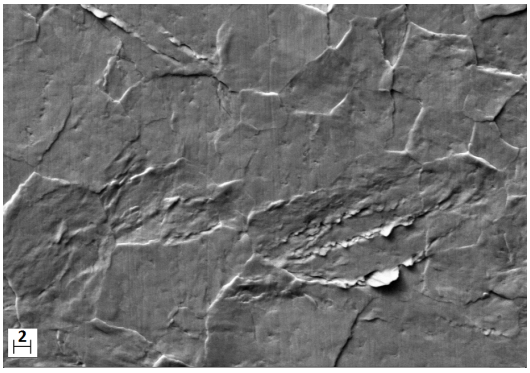

(c) 3-C

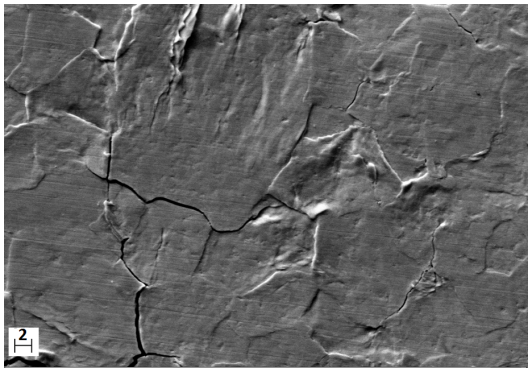

(d) 4-C (note the crack network)

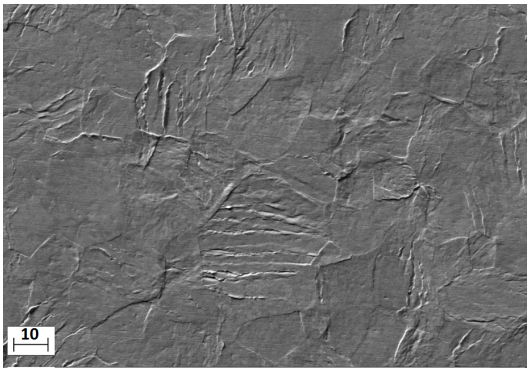

(e) 5-C

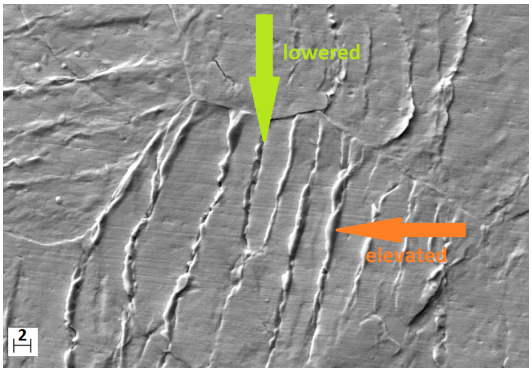

(f) 6-A (lowered and elevated areas of the ridges-like in-grain structure)

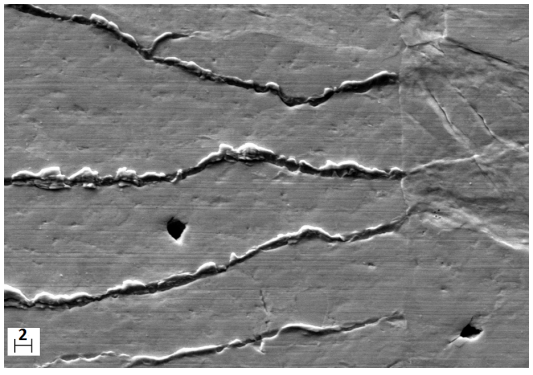

(g) 6-B (detailed interface)

Figure 2.28: Representative photographs of surfaces of the polished W-SPS samples (SEM SE mode). Spatial unit of the scales is [μm].

Comparison of polished and unpolished post-irradiated surfaces confirms the previous findings when investigated by SEM: sample 3-u shows a clear crack network formation. It is worth stressing out that damage of sample #3 consisted beside roughening of in-grain ridges formation, no cracks surrounding the grains were found. Ground surface must thus support the crack formation during the transient loading.

Comparison of loading sequences yields again a certain crack density reduction (some form of crack recovery) in case of simultaneous loading, *SPOT B*, Fig .2.29.

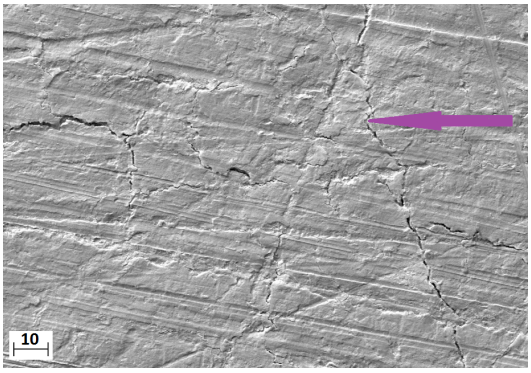

(a) 3-u-A (note the crack interconnecting the two main grooves)

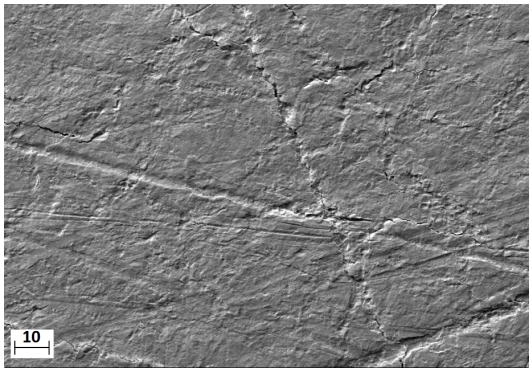

(b) 3-u-B

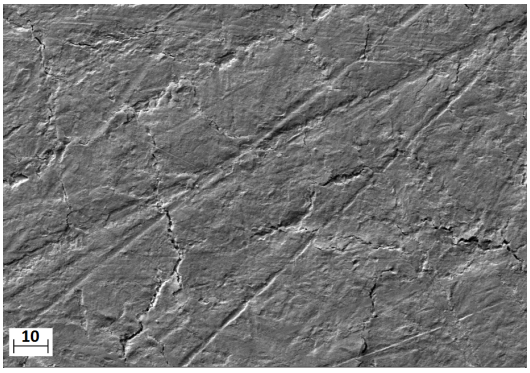

(c) 3-u-C

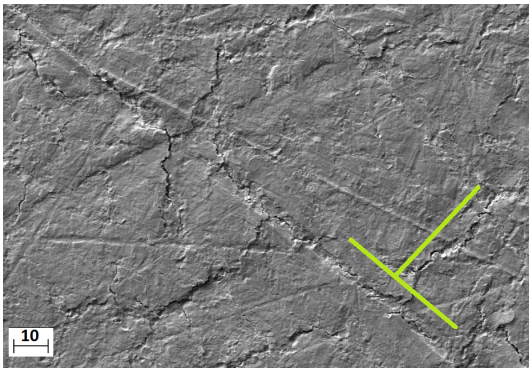

(d) 7-u-A (crack propagation perpendicular to main groove)

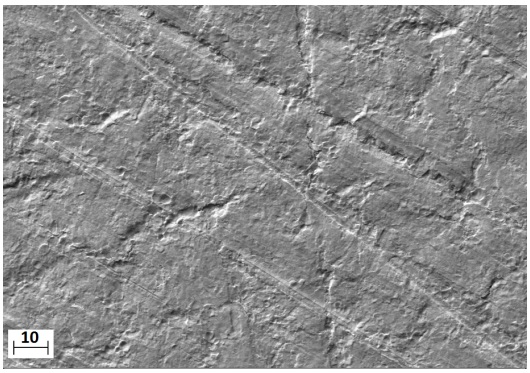

(e) 7-u-B

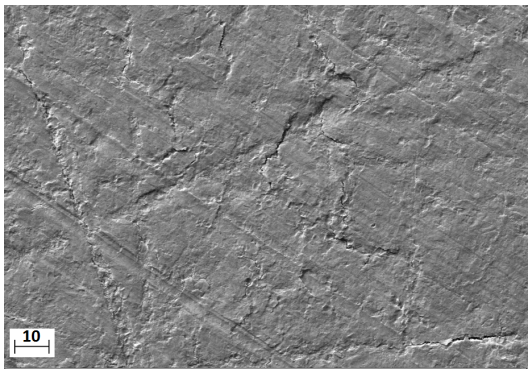

(f) 7-u-C

Figure 2.29: Photographs of surfaces of the unpolished W-SPS samples (SEM SE mode). Spatial unit of the scales is [μm].

Detailed photographs show that cracks propagate both inside of the residual

grooves, but also between them. At some cases the cracks appear to interconnect the main grooves (Fig. 2.29a), sometimes their orientation is perpendicular to the main groove (Fig. 2.29d). However the trajectory of the crack propagation and the final network seems to be rather random. No in-situ observation of crack formation and propagation was performed, it cannot be thus concluded whether the main grooves serve as crack nucleation sites or not.

Recapitulation of results

- Loading solely by D-plasma led to plastic deformation of the reference *SPOTS*, slight slip of grains along GBs probably took place.
- No particular difference in surface morphology was found between the surfaces loaded by distinct loading sequences. Exception is sample #1, in whose *SPOT A* cracks were found. Those cracks might be explained by embrittlement of material as a consequence of loading by transient pulses and reduced resistance to plastic deformation (and crack formation) during the subsequent loading by D-plasma. No cracks were found in *SPOTS B,C*.
- Relaxation of stresses induced in the surface layer by transient heat loading seems to be realized by plastic deformation resulting *either* in roughening (and eventually crack formation) *or* in roughening and in-grain ridges-like structure formation. Realization of either first or second variant seems to be dependent on fabrication parameters, rather than on the final grain diameter. Weaker inter-grain bounds might enhance the crack formation.
- Ridges-like in-grain structures seem to consist of regions of lowered and elevated material. This will be subjected to further investigation.
- Crack network was developed within the unpolished surface layers. Residual grooves must support the crack growth. It is not clear whether the main grooves serve as crack nucleation sites.
- Simultaneous loading by D-plasma and laser pulses leads to reduction of crack density in case of the unpolished surfaces.

2.5.3 Investigation of in-grain ridges-like damage structure

In the context of development of tungsten PFCs for fusion applications the ridges-like damage structures within the grains have not been reported yet. Since these represent an important damage mechanism in the frame of this work, it is worth to investigate this feature in further details.

Firstly, the apparent symmetry of the stripes indicates certain link to the symmetrical crystal structure of tungsten (body-centred cubic, with lattice parameter $a = 3.1652$ Å [122]). Of interest is thus to determine the crystallographic orientation of the areas circumscribed by the GBs and ridges, or better say, to determine if those regions are *misoriented* with respect to each other (Fig. 2.30a, example of grain containing three parallel stripes). Crystallographic orientation of the in-grain domains was determined by EBSD. Highly resolved line profiling can be obtained with the use of AFM. Usage of this technique can reveal first estimation of height/depth of the elevated/lowered areas within the grain. Finally,

in order to find out whether melting of material took place or not, near surface layer in cross-sectional view was investigated with the help of a FIB technique.

Crystallographic orientation of in-grain domains

In order to determine possible misorientation of in-grain areas delimited both by GBs and parallel stripes, a representative ROI was selected (within sample and *SPOT* 6-A), containing both grains with the ridges-like structure and undamaged grains (for reference). Map of grains orientation within the ROI, shown in Fig. 2.30b, revealed that within the angular resolution of the experimental technique, no misorientation is detected in between the in-grain domains. Twenty distinct grains/subgrains were detected within the ROI. Respective Euler angles are listed in Tab. 2.7.

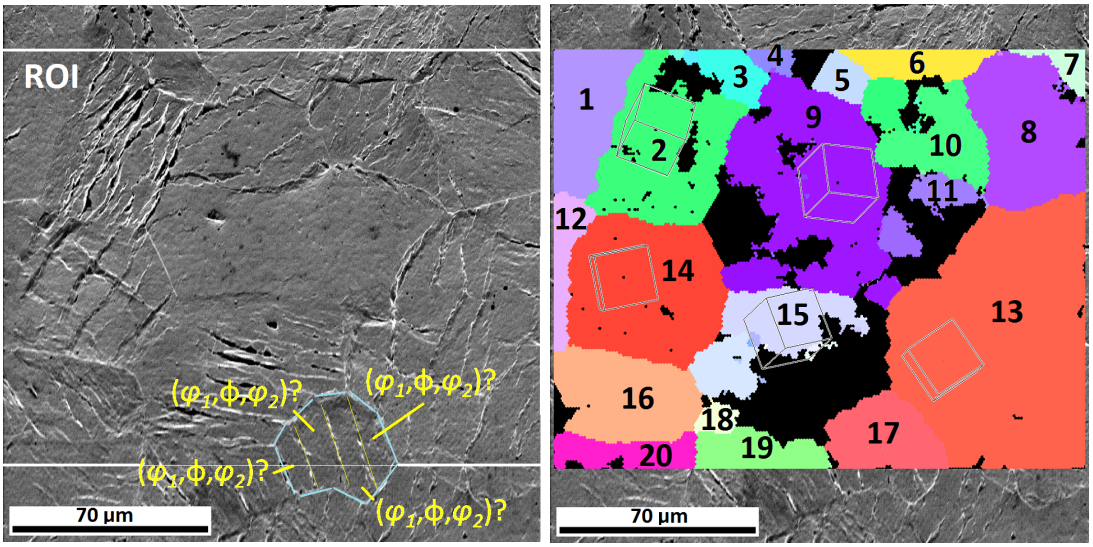

(a) (b)

Figure 2.30: (a) ROI containing both grains with the ridges-like structure and undamaged grains; (b) map of grain orientation determined by EBSD, Euler angles for respective grains are listed in Tab. 2.7.

grain #	ϕ_1 [°]	Φ [°]	ϕ_2 [°]
1	22.7	36.6	303
2	254	43.4	81.5
3	120	45.4	201
4	173	40.5	215
5	214	35.8	154
6	29.1	21.4	3.03
7	135	34.3	251
8	152	36.4	229
9	45.2	39.5	315
10	229	47.6	98.9
11	338	38.7	54.1
12	145	31.3	240
13	51.4	9.07	343
14	354	5.03	16.9
15	42.3	34.3	334
16	72.9	20.2	286
17	49.4	12.7	295
18	36.8	30.6	341
19	127	36.4	260
20	318	21.6	46.0

Table 2.7: Orientation of grains within ROI, determined by EBSD.

Highly resolved in-grain line profiling by AFM

In order to perform highly resolved line profiling of in-grain areas delimited both by GBs and parallel stripes, a representative ROI was again selected (within sample and *SPOT* 6-A, containing both grain with the ridges-like structure and a part of an undamaged grain (for reference). Dimensions of the ROI (50×50 μm) were optimized so that a significant part of the damaged grain could be investigated.

A 3D reconstruction of surface topography is given in Fig. 2.31a. Reference area lies in a grain with no ridges-like structure. Profiles were processed in such a way that the reference area was posed parallel to the laboratory surface. One representative line profile is displayed in Fig. 2.31b, its position along the y-axis is depicted in Fig. 2.31a by a blue line. Approximately 35 μm of the damaged grain area is included in this profile, including five elevated/lowered areas of sample material. Two interesting information can be extracted from the profile: firstly, maximum difference in height of the elevated and lowered areas is in this particular case approximately ~ 1.2 μm; secondly, regions in between the distinct stripes appear to be *parallel* to each other, confirming thus the previous findings,

i.e. lack of significant misorientation in between the in-grain domains.

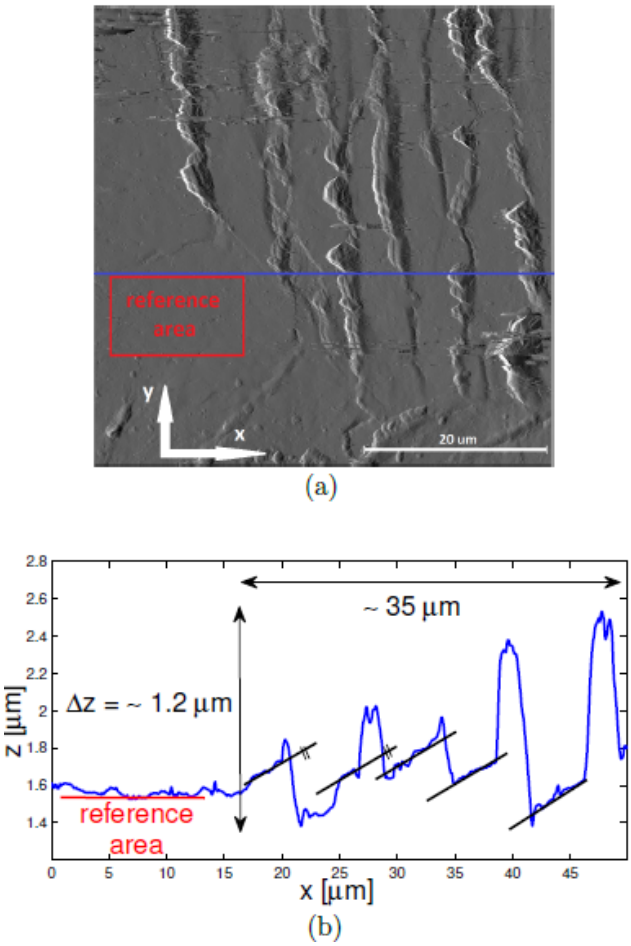

Figure 2.31: (a) 3D reconstruction of surface topography obtained by AFM; (b) representative line profile along the x-axis within the ROI.

Cross-sectional metallography by means of FIB analysis

As described in Sec. 1.3.3, molten material represents a potential source of dust within the fusion reactor's vacuum vessel, melting is thus well inspected during the development of tokamak PFCs. Representative ROI was thus selected prior to the FIB analysis (within sample and *SPOT* 6-A and 6-B, see Attachments for full record of the analysis, files FIB_6-A.avi and FIB_6-B.avi, step of images 1.0 and 0.5 μm, respectively). Detailed photographs show that the elevated material has rather sharp edges (see a representative example in Fig. 2.32a, *SPOT A*), which would indicate that no melting took place during the sample irradiation by laser heat pulses and the subsequent loading by D-plasma. On the other hand, rather rounded edges (indicating melting) were found on the elevated material in the proximity of a protective Pt layer, deposited on the ROI prior to the milling by the ion beam (Fig. 2.32b, *SPOT B*, corresponding to simultaneous loading). Cross-sectional metallography of the ROI revealed that the material was lowered due to formation of cracks of submicrometer width and length of approximately 1 μm, Fig.2.32c. Moreover, those microcracks show a parallel orientation with respect to each other (in a frame of a particular grain, Fig. 2.32d).

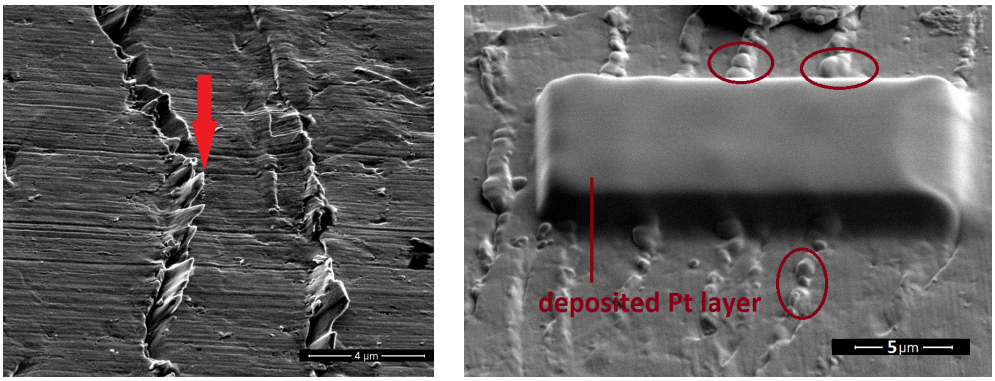

(a) 6-A (note the sharp edges of the elevated material)

(b) 6-B (note the rounded edges of the elevated material)

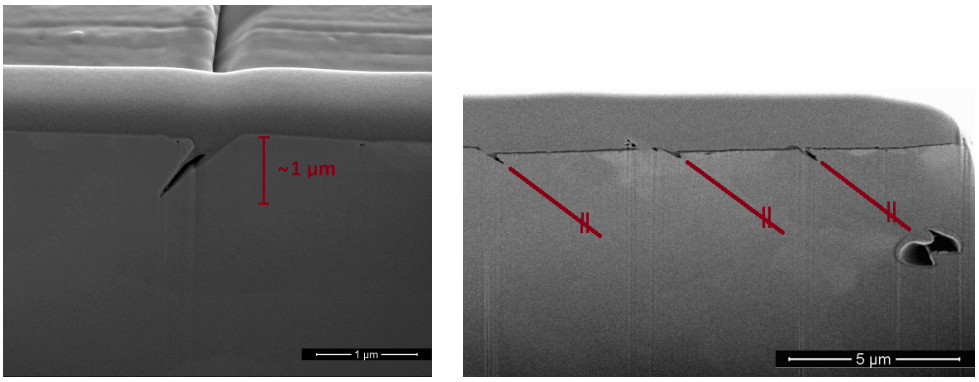

(c) 6-A

(d) 6-B

Figure 2.32: Photographs taken during the FIB analysis.

Analogy with deformation of monocrystal/polycrystalline material

Apparent symmetry of the in-grain ridges-like damage structures indicates a possible link to the crystallographic structure of the deformed material. It is known that at ambient temperature the main source of plastic deformation under material's compression or tension is the motion of dislocations through the crystal lattice. Dislocations move along fixed crystal planes (the so called *slip planes*) in certain crystallographic directions (*slip directions*) within these planes. The final *slip system* consists of combination of slip planes and directions. Tungsten has in total 24 slip systems with 12 of them originating from set of {1 1 0} planes with $<\bar{1}\ 1\ 0>$ directions and the remaining slip systems coming from set of {2 1 1} planes and $<\bar{1}\ 1\ 1>$ directions [29]. Schmid's law states that a threshold value of component of the shear stress in the slip's direction (the so called critical resolved shear stress, τ_C), necessary to initiate a slip within the grain, is given by [124]:

$$\tau_C = \frac{\text{force acting on slip plane}}{\text{area of slip plane}} = \frac{F\cos(\lambda)}{A/\cos(\Phi)} = \frac{F}{A}\ \cos(\lambda)\cos(\Phi), \qquad (2.17)$$

with the geometrical factors defined with the help of Fig. 2.33a (left). No slip occurs when the slip plane is parallel or perpendicular to the direction of the applied force. Appearance of the parallel stripes within the grains might thus be explained in terms of activation of a certain slip system during the irradiation of the surface layer of W-SPS samples by the transient heat pulses. Expanding

grains might push on each other, exerting thus compressive forces among themselves. It is a deformation of a polycrystalline material that eventually takes place here (with activation of various slip systems - or none - due to distinct crystallographic orientations of the grains), however the final geometry of the process is best viewed on an example of deformation of a monocrystal under applied tensile force, Fig. 2.33a (right, no spatial constraints are present in this example).

Nevertheless, activation of the slip within the grains does not explain the appearance of elevated/lowered material along the parallel stripes (slip bands). In order to explain this feature, it shall be reminded that the W-SPS samples are loaded *cyclically* during their exposure to the transient heat loads. Man et al. [123] studied in-situ with the use of SEM and AFM the evolution of fatigue cracks in cyclically loaded polycrystalline stainless steel samples. During the experiment a progressive growth of *extrusions* and accompanying *intrusions* along the slip bands, similar to those reported in this work, was found, e.a. formation of elevated and lowered regions of material (of approximately same height/depth) within the grains. Appearance of those regions is associated with the migration of point defects (vacancies) towards the surface during the cyclic loading. As nucleation sites of point defects, 'notch-peak' structures within the surface layer, being a consequence of activation of a certain slip system within the grains (Fig. 2.33a, right, encircled), are stated in the above mentioned reference. For more information concerning the extrusions/intrusions formation in fatigued material see for example [125, 126]. Combination of the in-grain slip and cyclic loading can thus lead to formation of both parallel ridges-like structures and elevation/lowering of the material alongside them. Man and his colleagues illustrated part of their experiment, in particular the AFM profiling of the steel surface, in a figure whose copy can be found in Fig. 2.33b. It is obvious that while AFM can provide information concerning the true height of the extrusions, profiling of the intrusions (cracks) is inaccessible by this method.

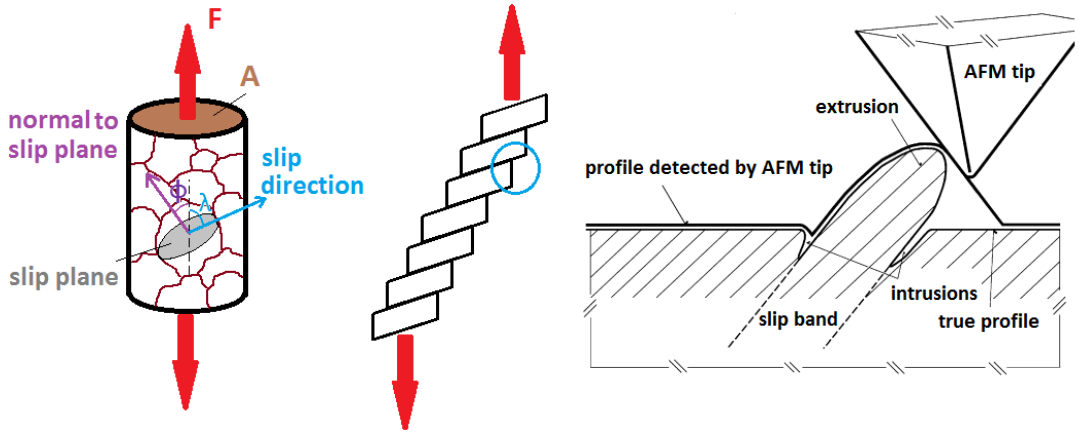

(a) (b)

Figure 2.33: (a) Schematic drawing of deformation of polycrystalline material (left) and monocrystal (right) under tensile loading, without any constraints. Encircled is a possible nucleation source of extrusions/intrusions under cyclic loading; (b) schema of AFM study of polycrystalline stainless steel specimen, with developed extrusion/intrusion relief [123].

Although the ridges-likes structure within the loaded areas show indisputably

symmetrical trend, the parallelism of stripes within the grains is violated to some extent, which might indicate presence of lattice defects in the grains. Those will be further studied in the following section. Moreover, dislocation movement is responsible for the activation of the slip systems. Their absence/presence within the grains of particular samples will be investigated.

Recapitulation of results

- Combined EBSD, AFM and FIB analysis provided extensive information concerning the topographical features of the ridges-like in-grain structures, found within some of the irradiated W-SPS samples.
- It appears that slip systems were activated, if possible, within the grains as a consequence of application of compressive forces during the irradiation by transient heat loads and consequent expansion of material. This process might explain appearance of parallel ridges-like structures within some of the grains.
- Slip band structures might have served further as nucleation sites for extrusion/intrusion (cracks) formation during the subsequent cyclic loading of the sample by the heat pulses. Formation of those structures is explained in the corresponding references by point defect formation in the slip band regions and their migration towards the surface of the specimen.
- Sharp edges of the extrusions indicate that the material was not melted during the exposure. Molten structures were found in the proximity of protective layers deposited prior to the FIB analysis.

2.5.4 Study of plastic deformation caused by dual exposition

Results of optical metallography, presented in Sec. 2.5.2, showed that the transient loading by laser pulses lead to pronounced plastic deformation of the originally polished surfaces (comparison of reference *SPOTS r* with *SPOTS A-C*). Moreover, inspection of reference surfaces indicates that these areas were plastically deformed, under D-plasma impact, as well. Plastic deformation is an undesirable damage mechanism in the context of the fusion reactor PFCs, since sharp edges (vulnerable to melting), cracks etc. might be formed. Plastically deformed and recrystallized material might show degraded mechanical and thermal properties such as hardness or thermal conductivity etc. Post-irradiation level of plastic deformation of the W-SPS sample set will be studied in this section. Firstly, roughness of the loaded surfaces (indicator of plastic deformation), obtained with the help of the optical profiler, will be presented. Secondly, surfaces will be inspected by SEM in BSE mode (with the emphasis on channelling, revealing possibly the lattice defects) and finally the size of crystallites and level of microstrain, measured with the use of XRD analysis, will be showed.

Roughness of W-SPS *SPOTS* set

Level of plastic deformation is reflected in increase of roughness of the originally polished surface, since a relation of proportionality might be posed in between them. Roughness of the full set of W-SPS samples and available *SPOTS* was thus evaluated by optical profilometry. Results are listed in Tab. 2.8.

sample #	*SPOT*	S_a [nm] (5x/20x)	$\overline{S_a}$ [nm]
1	r	17.8/16.9	17.4
	A	150/130	140
	B	150/140	145
	C	161/146	154
2	r	29.4/27.4	28.4
	A	146/108	127
	B	144/126	135
	C	131/111	121
3	r	29.0/30.9	30.0
	A	146/113	130
	B	169/144	157
	C	165/137	151
4	r	28.3/25.7	27.0
	C	108/94.3	101
5	r	37.7/33.0	35.4
	C	148/143	146
6	r	72.0/59.2	65.6
	A	294/228	261
	B	251/225	238
	C	298/213	256
3-u	r	75.7/89.3	82.5
	A	183/178	181
	B	192/171	182
	C	189/173	181
7-u	r	87.7/91.1	89.4
	A	202/170	186
	B	113/105	109
	C	185/163	174

Table 2.8: Roughness of W-SPS samples *SPOTS*. Given are results obtained with magnifications 5x and 20x. Larger area can be inspected with lower magnification, however the lateral resolution is decreased. Compromisingly, last column contains the mean $\overline{S_a}$ (treated in the text) calculated as the average of the two S_a values.

Pre-irradiation treatment of part of the specimens consisted of surface polishing with a final roughness $R_a < 100$ nm. However, the actual pre-exposure surface roughness of the samples surfaces was not measured prior to the experiment, absolute reference roughness of the surfaces is thus not available. Nevertheless, it can be assumed that the absolute roughness values were the same for all samples. Comparison of S_a of the polished *SPOTS r* loaded solely by D-plasma show an interesting dependence on the grain size (Fig. 2.34) in case of polished samples. Slip along GBs, leading to differences in the height of the particular slipped grains, seems to be thus proportional to the grain diameter. Increase of roughness by a factor $5 - 8\times$ of the areas loaded by laser pulses with respect to the reference areas is observed (case of polished samples). Largest difference in S_a is seen in sample #1, with the smallest grain diameter, lowest shows sample #4. As expected, difference in S_a of reference *SPOTS r* of polished and unpolished samples #3 and #3-u is observed.

No particular difference or trend in roughness values can be found within the *SPOTS A-C* differing by the loading sequences. An exception is sample #7-u, *SPOT B*. Simultaneous loading by D-plasma and transient heat loads lead in this case only to a slight plastic deformation, reflected in a minor increase of the roughness with respect to the reference spot.

Certain dependence of S_a on grain size can be observed, Fig. 2.34 (S_a is averaged over the three *SPOTS*). However, this trend is violated in case of samples #1 and #4. The latter showed a crack network formation when inspected by SEM. The sample was plastically deformed up to such a level that the roughness was increased possibly by a factor of ~ 4 before it broke. Nevertheless no in-situ crack monitoring was performed during the exposure, it is thus not clear whether was the surface layer further deformed. Since this specimen exhibits the lowest factor of positive increment of roughening of all samples, it might be supposed that the other samples deformed plastically by the same factor and the final increase in profile roughness was due to the gradual growth of extrusions/intrusions (if applicable). Roughness of sample #1 is rather high in the context of the overall tendency (recall the increase in roughness by factor ~ 8 in comparison with reference area). No cracks or in-grain stripes were found in case of this specimen (in *SPOTS B,C*). Relaxation of the stresses induced by transient loadings was thus realized through pronounced slip of grains along GBs, leading to the final rough relief.

Final roughness of the sample #3-u is larger than that of the #3 in absolute numbers. However, increase in roughness is by a factor ~ 2 and ~ 5, respectively. The unpolished sample was relaxed via dense crack network formation.

No particular difference in S_a is observed between the two values of the unpolished samples, #3-u and #7-u, differing by grain size. Specimen #7-u exhibits the lowest roughness in case of loading sequence b), confirming thus the previous observations.

Observation of lattice defects by means of SEM in BSE mode

With a proper adjustment, inspection of metal surface by SEM in BSE mode with emphasis on ECCI provides information concerning the relative orientation of lattice domains, as was described in one of the preceding section. Thanks to ECCI, lattice defects such as dislocations can be recognised within the images.

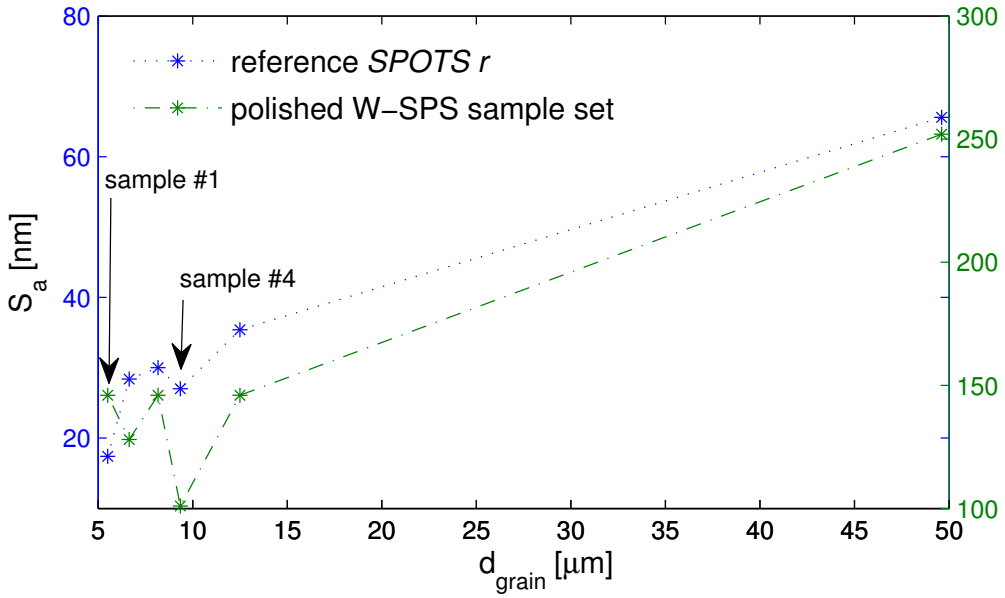

Figure 2.34: Final surface roughness reported as a function of the grain size. Samples #1 and #4 show deviation from the overall tendency. This graphic serves for trend observation, no error bars are displayed.

Surfaces of all *SPOTS* of W-SPS samples were thus examined in this mode in order to gather information about the concentration of lattice defects within the grains. Full set of photographs of surfaces of *SPOTS A-C* can be found in the Attachments.

No particular dependence of lattice defects concentration on loading sequence can be recognised within the set of *SPOTS A-C* in case of polished samples. Representative photographs of each of the specimen were thus chosen, those can be found in Fig. 2.35.

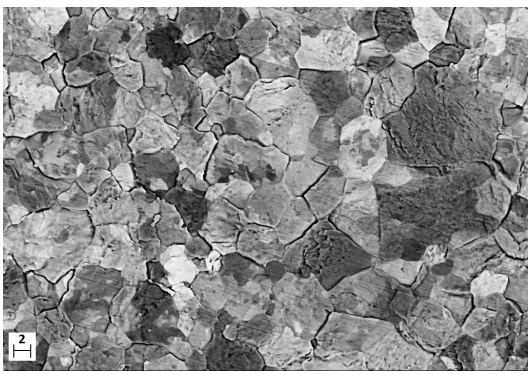

(a) 1-B

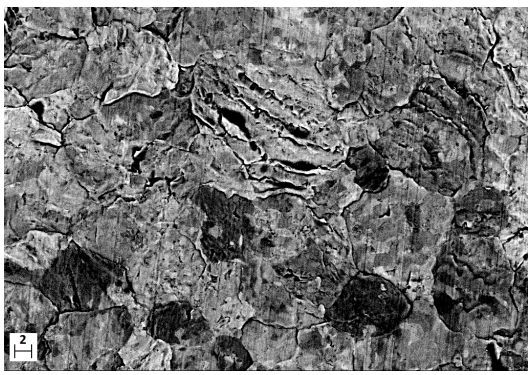

(b) 2-B

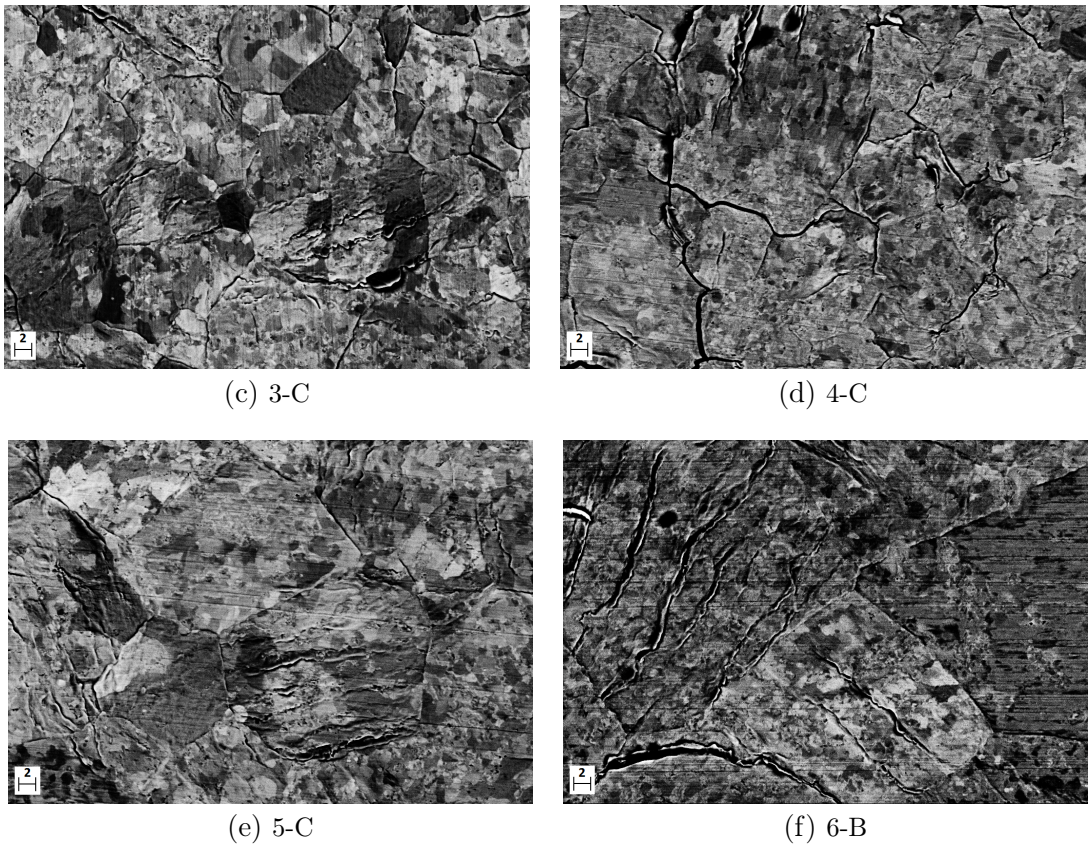

(c) 3-C (d) 4-C

(e) 5-C (f) 6-B

Figure 2.35: Representative photographs of surfaces of the polished W-SPS samples (SEM BSE mode). Spatial unit of the scales is [μm].

Thanks to the contrasting of grain scale within the frame of the individual grains, it is evident that grains contain large amount of defects (resulting in appearance of domains of different lattice orientation within the individual grains). However, in case of samples #1-3 coherent domains of size of the order of the grain diameter can be distinguished. It seems that the largest density of grains with no apparent defects can be found in sample #1, the only sample that did not contain slip band structures within the grains. Position of the defects within the grains appears to be rather random, with no particular relation to the slip bands. Smallest domains with the same orientation appear to be present in sample #4, which cracked during the irradiation. However this shall be further confirmed by XRD analysis and deduction of the coherent domain size.

Unpolished samples cracked during the exposure, no apparent slip along the GBs took place. Domains of the same crystallographic orientation, of rather circular shape, can be found all over the samples #3-u and #7-u (Fig .2.36). Unlike the case of #3-u, coherent domains can be clearly distinguishable within the individual grains of specimen #3.

It appears that in case of loading sequence a) the size of the coherent domains is smaller in comparison with that of sequences b) and c) in both unpolished samples (compare the photographs in the Attachments). Nevertheless, precise measurement of their size shall be deduced with the help of XRD.

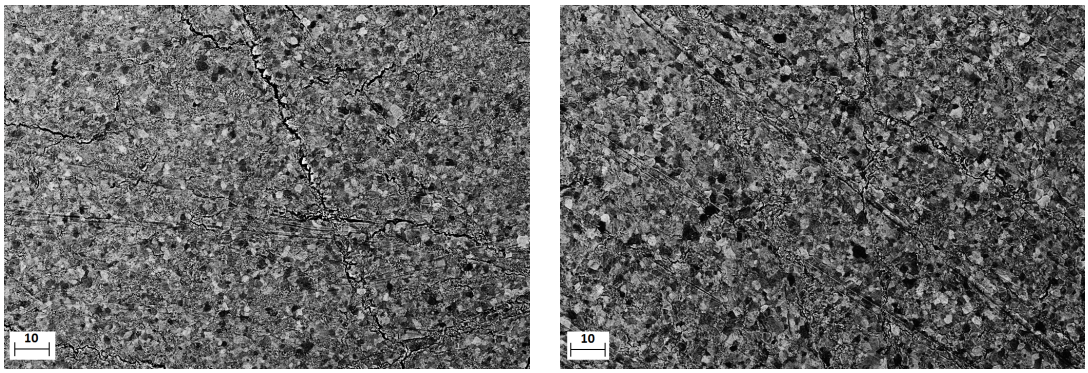

(a) 3-u-B (b) 7-u-B

Figure 2.36: Representative photographs of surfaces of the unpolished W-SPS samples (SEM BSE mode). Spatial unit of the scales is [μm].

Measurement of crystallite size and microstrain by XRD

With the help of XRD analysis, crystallite size L of all available *SPOTS* of the W-SPS sample set was determined. Results are listed in Tab. 2.9, third column. Moreover, thanks to the surface polishing of the other side of sample #1, crystallite size was determined for part of this sample that was without any contact with either D-plasma or laser. This measurement (label as 'no plasma') will serve as an absolute reference in the further analysis.

Examination of the results yields several information. Firstly, in case of the surface roughness, no particular dependence of crystallite size on grain diameter can be followed in case of reference polished surfaces. It seems that due to impact of D-plasma, final size of coherent domains was $L_{ref} \sim 100$ nm for all polished samples. Comparison of un-irradiated crystallite size with that of the reference *SPOT r* in case of specimen #1 shows that L was approximately doubled during the D-plasma impact. This indicates that beside plastic deformation through slip along GBs, the as-prepared deformed grains underwent recovery during the D-plasma loading. It is worth noticing that recovery might lead to reduction of original material strength. Surface temperature during the D-plasma loading should not have exceeded the recrystallization temperature. This is not the case of the loading by transient heat pulses. It is assumed that the temperature could rise well above T_{rec}, resulting in an initiation of recrystallization, i.e. growth of undeformed grains. This is well seen in comparison of L in case of reference and loaded *SPOTS*. Coherent domains were increased by factors $\sim 1.5 - 3.5$.

Interesting is a comparison of crystallite size of polished and unpolished samples set, #3 and #3-u. In case of unpolished surface, the recovery did not take place to the same extent as in the polished sample (compare the corresponding L values in Tab. 2.9). Recovery following the plastic deformation (slip along GBs) did not take place in case of unpolished surfaces. Residual grooves must served as slip inhibitor.

No generally valid trend can be deduced from the crystallite size for distinct loading sequences in case of polished surfaces. Although it might be in principle assumed that during the sequence b) the surface temperature was larger in comparison with the two other sequences, larger L within *SPOT B* is not observed for all of the samples. In any case, it shall not be forgotten that the measurements

sample #	*SPOT*	L [nm]	d_{grain} [μm]	d_{grain}/L	$\epsilon \cdot 10^{-3}$	present phases
1	no plasma	60.5	-	-	1.09	W
	r	128	-	-	1.01	
	A	211	4.27	20.2	0.855	
	B	255	7.82	30.7	0.899	
	C	223	4.44	19.9	0.870	
2	r	110	-	-	1.04	W
	A	219	6.26	28.6	0.893	
	B	196	7.06	36.0	0.877	
	C	234	6.61	28.2	0.962	
3	r	97.0	-	-	0.971	W
	A	204	8.58	42.1	0.936	
	B	247	7.58	30.7	0.937	
	C	186	8.36	45.0	0.894	
4	r	102	-	-	0.987	W, W_2C
	C	156	9.35	60.0	0.994	
5	r	114	-	-	1.03	W
	C	195	12.5	64.1	0.939	
6	r	85.0	-	-	0.820	W, W_2C
	A	298	50.1	168	1.12	
	B	246	50.8	207	0.953	
	C	141	47.9	340	0.865	
3-u	r	59.1	-	-	1.16	W
	A	194	-	-	0.989	
	B	229	-	-	0.980	
	C	208	-	-	0.995	
7-u	r	54.8	-	-	1.05	W
	A	172	-	-	0.855	
	B	193	-	-	0.839	
	C	187	-	-	0.877	

Table 2.9: Results of the XRD analysis. Fourth column contains grain diameters, deduced by optical metallography, see Tab. 2.5

.

were made on as-irradiated surfaces without further (polishing) treatment, which might in principle distort the measurements. Surface roughness is largest in case of sample #6, for which the difference in crystallite size for distinct *SPOTS* differs by a factor of 2.

In almost all polished samples, $L \sim 200$ nm, indicating independence of the recovery on the grain size, at first sight. However, average values (over the three loaded *SPOTS*) indicate that the final crystallite size decreases slightly with increasing grain diameter (Fig. 2.37). Recrystallization could be reduced by present in-grain lattice defects. Exception represents sample #4, which confirms the previous findings obtained with SEM in BSE mode. This might mean that the sample was under transient loading plastically deformed (and grains recrystallized) up to a level in which the stresses relaxed through crack formation. Recrystallization might in principle continue after the crack formation, however an analogy can be found with the case of unpolished surfaces, in which the residual grooves served probably as plastic deformation inhibitors. It is possible that the cracks (surrounding grains) could serve as grain growth inhibitors. In order to evaluate the level of lattice defect concentration within the particular grains, and provide thus a link to the variable parameter (grain diameter), it is useful to define a certain comparative factor indicating the level of lattice defects within the grains. This can be defined for example as ratio d_{grain}/L. The larger the ratio is, the higher is the lattice defect concentration within the grains. This parameter can be found in Tab. 2.9, fifth column. Following its trend, it is clear that the concentration of defects increases with the grain diameter with no exceptions.

No particular difference in crystallite size is seen in case of unpolished/polished sample pair. Residual grooves could have in principle served as plastic deformation inhibitor, nevertheless the recrystallization took place up to the same level as in case of polished sample.

Largest coherent domains are found in *SPOT B* in case of both unpolished samples. Those areas also showed slightly improved resistance to crack formation. Simultaneous loading by D-plasma and laser pulses might, as was mentioned previously, induce larger surface temperature. However, the mechanism standing behind the crack density reduction stays unclear.

Smaller coherent domains are found in sample #7-u in comparison with sample #3-u in case of all *SPOTS*, including the reference ones. This is an interesting trend, considering that in case of polished surfaces the crystallite size showed rather week (or none) dependence on the grain size. It seems that larger grains limited the plastic deformation during the loading both by D-plasma and transient heat pulses in case of unpolished samples.

As was mentioned in the corresponding introductory section, microstrains can serve as indicators of the plastic deformation that took place during the samples irradiation. Microstrain ϵ was deduced with the help of XRD, results of the measurement are listed in Tab. 2.9, sixth column.

First information can be obtained from the comparison of absolute microstrain, measured within sample #1 with that of the reference *SPOT r* irradiated by D-plasma. As-prepared, originally deformed sample part, show larger lattice distortion than that which underwent D-plasma loading, indicating again a plastic deformation and subsequent recovery taking place during the plasma loading. Again, no general trend can be followed for values of reference microstrains as

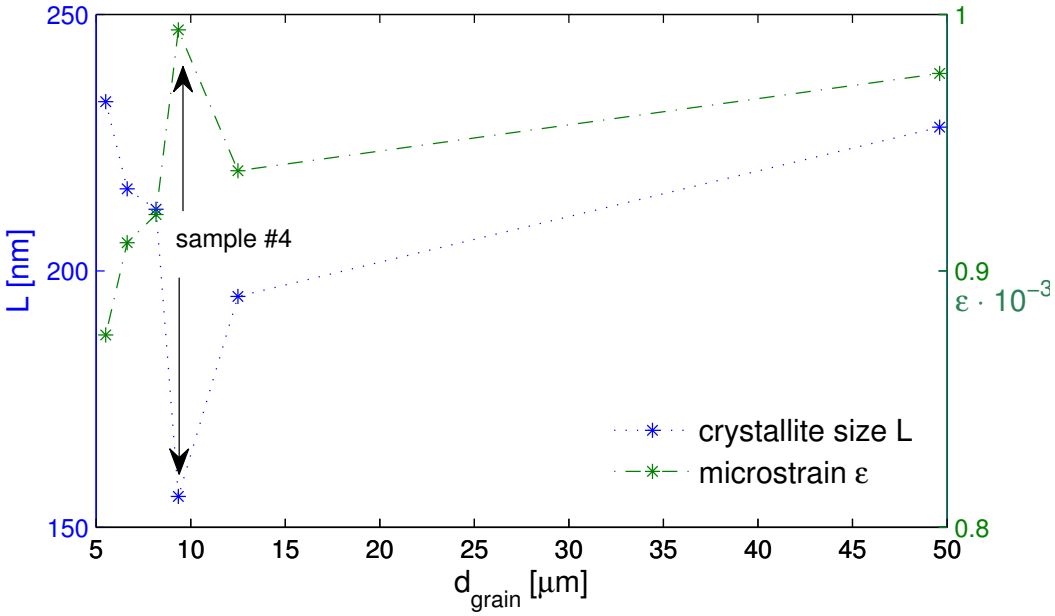

Figure 2.37: Dependence of crystallite size and microstrain on the samples grain size (polished W-SPS sample set).

a function of grain size. Microstrain seems to be reduced as a consequence of transient loading, except for sample #4 and #6. Limitation of recovery in case of unpolished sample #3-u led to larger final value of ϵ of reference *SPOT* r in comparison with that of the polished sample #3.

Again, no particular dependence of ϵ on the loading sequence can be recognised. On the other hand, the microstrain averaged over the three loaded *SPOTS* seems to be proportional to the grain diameter, Fig. 2.37. This might indicate that level of plastic deformation is proportional to the grain size, which is consistent with the previous determination of the surface roughness. Exception of this trend represents again sample #4. This sample exhibits the largest ϵ of all polished samples.

Microstrain is larger in case of unpolished sample in comparison with that of the polished one, indicating larger lattice distortion in case of specimen #3-u.

Lower ϵ shows again the sample #7-u in comparison with sample #3-u. Just as is the case of the crystallite size, this fact remains unclear.

Some of the observations still remain unexplained in terms of the so far measured quantities and since no particular relation to the grain size can be found, discussion shall be brought back to the role of fabrication parameters on the sample damage resistance, discussed firstly in Sec. 2.5.2.

In comparison to sample #2, sample #1 was prepared with lower grain size of the tungsten powder. This fact resulted in lower final grain size of the bulk as-prepared specimen and so far this sample showed the best resistance to the damage induced by transient heat pulses in terms of no crack or slip bands formation. On the other hand, this sample shows relatively high roughness of the surface, largest crystallite size, lowest concentration of lattice defects within the grains and at the same time lowest level of microstrain. This might indicate that

the relaxation of stresses induced by transient pulses was realized solely by the slip along GBs, with pronounced elevation of the GBs leading to relatively rough relief. Rather low amount of in-grain obstacles did not however reduce the grain recrystallization and stress relaxation, resulting in the largest values of L and ϵ.

Trends of microstrain and crystallite size as a function of the grain diameter remains unclear in case of samples #3-u and #7-u. Their tendencies do not follow that of the polished samples. However, those two samples differ only by the fabrication powder grain size. Resulting grain diameters shall gradually increase from smaller to larger, sample #3-u and #7-u, respectively.

Completely unclear so far stays the crack formation within the surface of sample #4. This sample does not follow any trend presented in this subsection (except for the concentration of the in-grain lattice defects). On the other hand, explanation of this behaviour might be found in the last column of Tab. 2.9, which shows the phases detected during the XRD measurements. Tungsten carbide was detected in case of samples #4 (at.%2) and #6 (at.%1 - just above detectable limit). Although its presence might be expected in case of sample #6 (due to high sintering temperature and time, both supporting the carbon diffusion and formation of the carbides), its detection within the sample #4 is surprising. Sintering time was set to only 2 minutes in case of this sample. Nevertheless, high sintering temperature must have supported to a sufficient level the carbide formation within the central regimes of the prepared component. As is stated in [127], presence of interstitial carbon increases significantly the tungsten's DBTT. Even though the BT was set to 400 °C, and it was proved so far that this is enough to exceed the W-SPS DBTT, this BT is probably not sufficiently high to exceed the DBTT once W_2C is formed. Sample could be thus brittle during the exposure, which might led to crack formation along the GBs.

Recapitulation of results

- Combined optical profilometry, SEM surface metallography in BSE mode and XRD analysis provided extensive information concerning the deformation of the samples during the irradiation by D-plasma and transient heat pulses.

- Surface roughness, indicator of plastic deformation, is proportional to the grain size, with exception of cracked sample #4 and sample #1, the latter showing extraordinarily high roughness in this context.

- Lattice defects were identified within the grains with the help of ECCI. Their in-grain concentration is proportional to the grain size in case of polished surfaces. No individual grains are recognizable within the unpolished samples. Induced stresses were in this case relaxed through crack formation.

- Comparison of absolute crystallite size present in reference, un-irradiated, surface (sample #1) indicates that surfaces loaded solely by D-plasma underwent plastic deformation through slip along GBs *and* recovery.

- Crystallite size and microstrain showed no general dependence on the loading sequence.

- Microstrain, an indicator of plastic in-grain deformation, increased slightly with grain diameter.
- Fabrication parameters showed to influence strongly the subsequent performance of specimens during the transient loading. In case of sample #4, large sintering temperature lead to tungsten carbide formation, increasing thus the DBTT.

2.5.5 Cross-sectional metallography

In order to study near-surface and in-depth post-irradiation changes in surface structure (and, for example, determine the depth of the cracks, if applicable), samples were cut vertically and examined by SEM in BSE mode with emphasis on ECCI. Full set of photographs of W-SPS samples and *SPOTS* set can be found in the Attachments. Moreover, photographs of cross-sectional surfaces taken at approximately 200 μm from the original loaded surfaces are included in the attached file as well. Those might serve as a reference for comparison of the surface region with the in-depth, bulk region, unaffected by exposure. Those photographs are labelled as 'X-middle', where 'X' is replaced by the corresponding sample number. Representative set of photographs can be found in Fig. 2.38 (polished samples). For better orientation, results of the analysis will be discussed in separate blocks, each sample individually. Overall conclusions will be given afterwards.

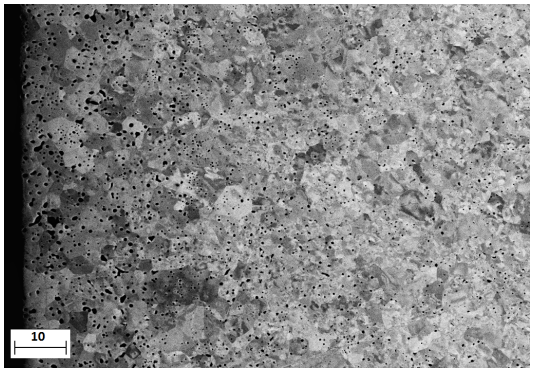

(a) 1-C

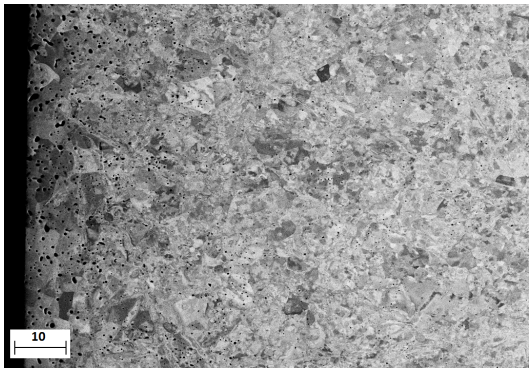

(b) 1-r

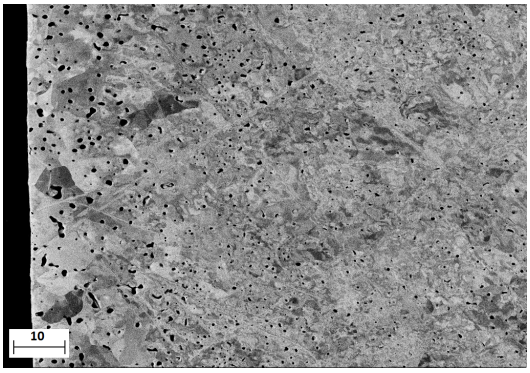

(c) 2-B

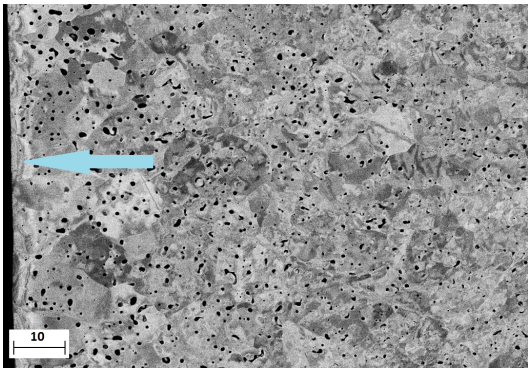

(d) 2-r (note the stripes parallel to surface)

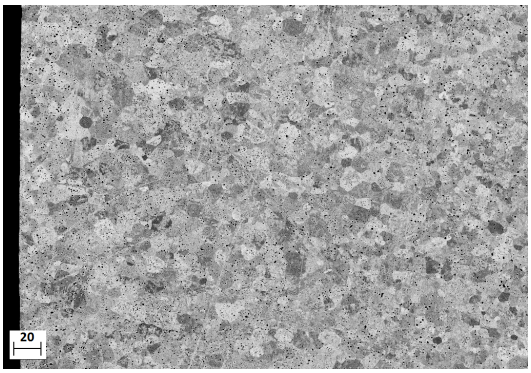

(e) 3-C

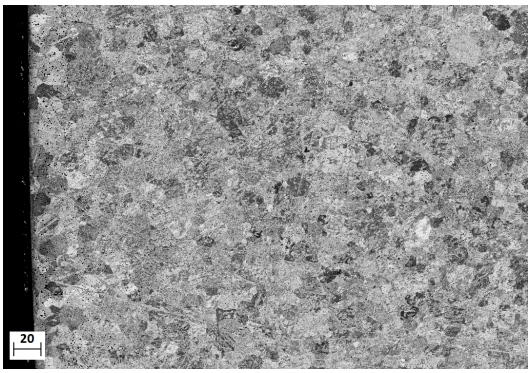

(f) 3-r

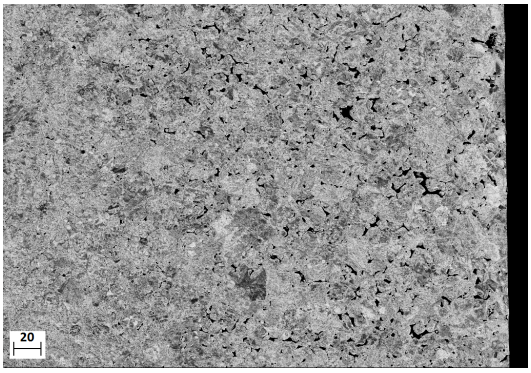

(g) 4-C

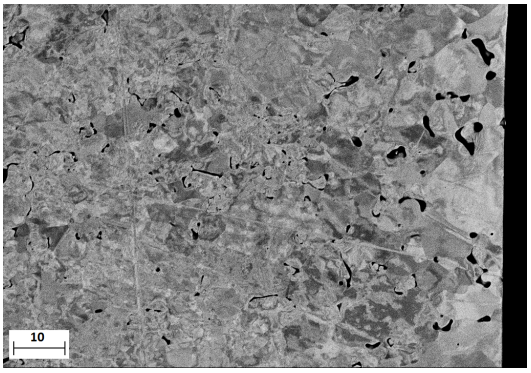

(h) 4-r

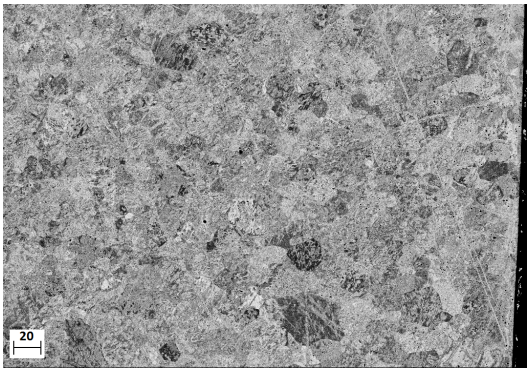

(i) 5-C

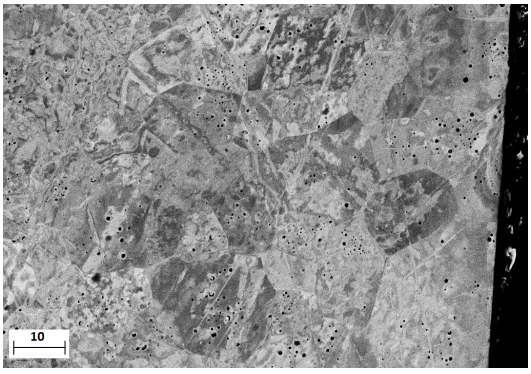

(j) 5-r

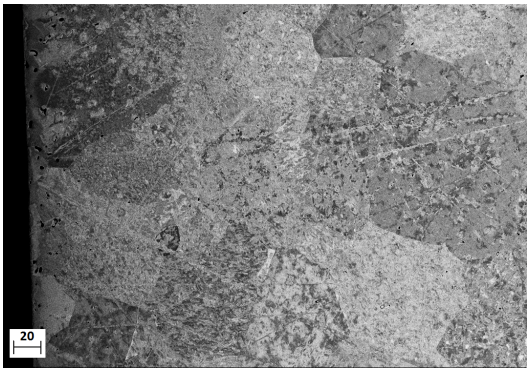

(k) 6-C

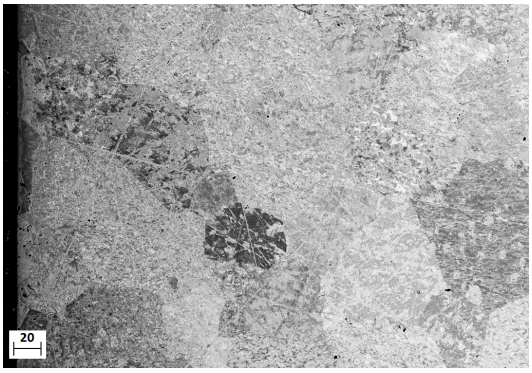

(l) 6-r

Figure 2.38: Representative photographs of cross-sectional surfaces of polished W-SPS samples (SEM BSE mode). Comparison with reference areas (*SPOTS r*) is given. Spatial unit of the scales is [μm].

- #**1** This sample was prepared at the lowest sintering temperature, presence of pores within the bulk of the specimen is thus expected (although the applied fabrication pressure was the highest, which shall support the densification of the component). It is thus not surprising that pores are found within the sample. Pore concentration shows approximately constant distribution all over the volume of the sample, however their size is the largest in the near-surface region. Recall that pores, lattice defects etc. might serve as deuterium traps. Regions of the same orientation, of size of the order of the deduced post-irradiation grain size, can be distinguished within the full volume of the sample. However, concentration of in-grain defects is dramatically decreased in the near surface region, indicating that the as-prepared in-grain defects were substantially recovered during the irradiation procedure [9]. This is applicable for all *SPOTS*, including the reference one. Nevertheless, in case of *SPOT r*, recovered grains seem to be recovered only up to depth of $\sim$ 15 μm, while in the other *SPOTS* recovered grains can be found in larger depths (up to $\sim$ 30 μm. Recovery might explain the increased pore size, since the vacancies could diffuse throughout the volume and concentrate within the pores, increasing thus their volume. However such macroscopic difference in pore size indicates rather that deuterium atoms concentrated in those areas and increased their size. Interesting information yields comparison of in-depth changes within the *SPOTS* differing by the loading sequence. It seems that the grains are in *SPOT B* recovered up to lower depth than within the other *SPOTS*. This might mean that the heat transfer towards the bulk was decreased in this case, keeping thus the heat in the near surface zone, resulting in more important grain growth. This would explain the increased average grain diameter within this *SPOT* in comparison with the two other areas (see Tab. 2.5). This is an interesting phenomenon, reflecting the synergistic effect of the simultaneous loading and discussion concerning the particular loading sequences, reflecting the so far obtained findings, shall be made here:

  a) During the transient heat loading, surface is plastically deformed, lattice defects are recovered, grains are due to high temperature recrystallized, size of pores is slightly increased due to migration of point defects. Subsequent loading by D-plasma leads to further plastic deformation and grain recovery, deuterium atoms enter the surface region, diffuse through the bulk and eventually get trapped within the lattice defects and pores, increasing thus their size.

  b) D-plasma was impacting for several minutes the sample surface, until the steady state was achieved. During this time, surface could plastically deform and recover, deuterium could enter the bulk, get trapped etc. Transient heat pulses, increasing the temperature above T_{rec} (probably), lead to grain growth and partial de-trapping of deuterium atoms through enhanced diffusion of the atoms. Deuterium atoms were nevertheless constantly bombarding the surface during the exposure.

  c) Loading by D-plasma lead to exactly same state of the near-surface layer

[9] The larger the pores, the lower the thermal conductivity towards the bulk (i.e. note the possible post-irradiation degradation of thermal properties)

as can be seen on Fig. 2.38b. Once the heat pulses were applied, the heat propagated into the in-depth region causing the grain growth. Trapped deuterium could be released during the transient loading.
From the described scenarios it seems that periodical trapping and detrapping of deuterium could influence the heat propagation within the near-surface regions.

- #**2** Pores are, just as in the case of sample #1, distributed homogeneously over the sample volume. Largest pores can be found in the near-surface region, in consistency with the previous sample. Situation analogical to that in case of sample #1, in terms of in-depth in-grain changes and difference between the particular *SPOTS* can be found, including the in-depth spatial scales. Presence of 'stripes', parallel to the original surface, distinguishable in the reference *SPOT* seem to be a residual effect of the pre-experiment treatment rather than having some physical meaning.

- #**3** This sample was prepared at higher temperature than the previous two specimens, however the applied pressure was lower, defavoring thus densification in comparison to previous samples. Pores within the bulk can be recognised, with homogeneous distribution over the specimen. Yet, their size does not seem to be so dramatically affected in the vicinity of the surface. Reference *SPOT* shows that the lattice defect recovery took place up to depth of $\sim$ 15 μm. However, no particular difference in recovery/recrystallization depth can be unambiguously recognised within the *SPOTS A-C* set. Recovery depth seems to propagate till the depth of $\sim$ 30 μm in all cases.

- #**4** Specimen was prepared with the largest powder grain size, with sintering time set to only 2 minutes. Boundaries between the individual grains of the original powder can be still clearly recognised within the full volume of the specimen. Their size is increased in the vicinity of the original surface, forming even macroscopic cavities. Cracks along the grains, with depth of several micrometers, are clearly visible. Beside the crack formation, no particular difference between the reference and laser loaded *SPOT* can be recognised. Grains seem to be somewhat recovered up to the depth of few micrometers.

- #**5** This sample, sintered for one hour, still shows presence of pores, however of low concentration. Their size appears to be slightly increased in the proximity of the loaded surface. Depth of recovery/recrystallization seems to be the same as in previous cases.

- #**6** Formation of pores is nearly suppressed in case of this specimen. Same differences between the *SPOTS* in terms of recovery/recrystallization depths and trends can be retrieved as for samples #1 and #2.

Fabrication parameters are reflected in the features of the investigated surfaces. No particular dependence of the damaged features on grain size can be recognised. In terms of in-depth changes no particular difference in terms of spatial scales can be found within the samples set.

Representative set of photographs of unpolished samples can be found in Fig. 2.39.

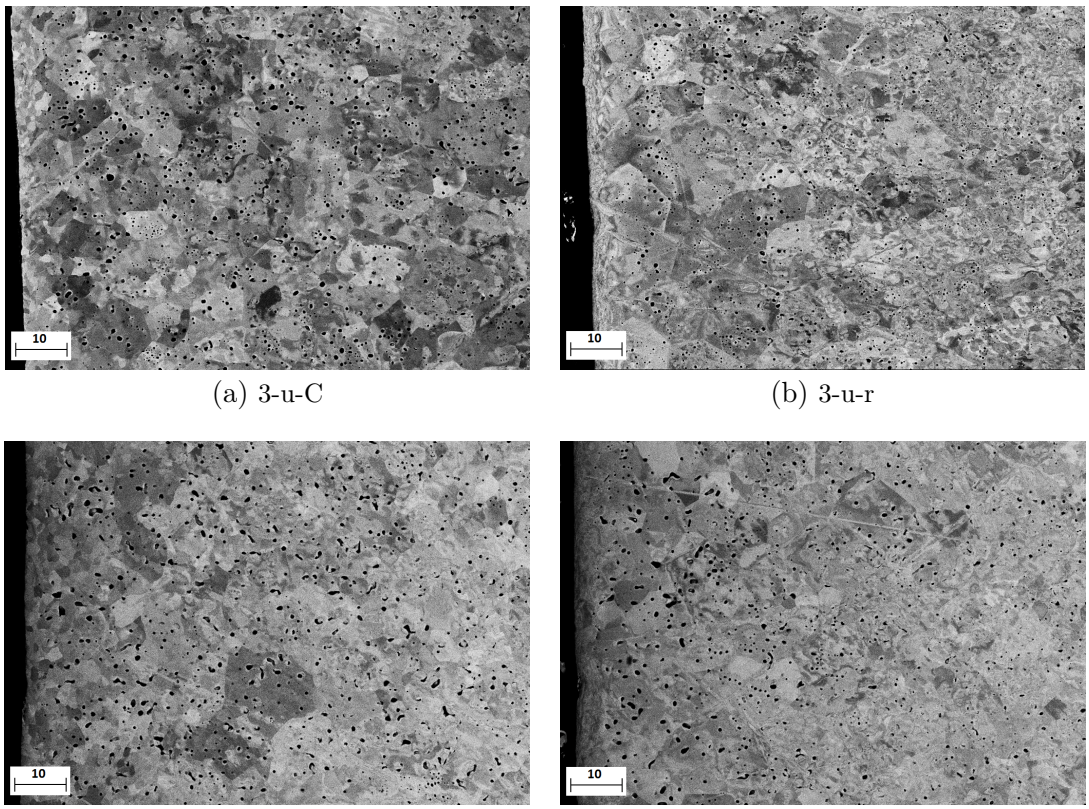

(a) 3-u-C (b) 3-u-r

(c) 7-u-B (d) 7-u-r

Figure 2.39: Representative photographs of cross-sectional surfaces of unpolished W-SPS samples (SEM BSE mode). Comparison with reference areas (*SPOTS r*) is given. Spatial unit of the scales is [μm].

- #**3-u** Surfaces loaded by laser pulses show a completely different in-depth features than the reference areas. The later show some unclear structure of domains parallel to the surfaces. In principle those seem like molten layers, but no melting is supposed to take place during the irradiation, more probably they might be a consequence of the pre-experiment treatment. In comparison to the polished sample #3, practically no pores can be found in the vicinity of the loaded surface (up to depth of $\sim$ 5 μm). However, concentration of pores is the same for both samples. Small domains of same orientation (recognizable in previous sections of this work) can be clearly distinguished. Those domains are present up to depth of $\sim$ 5 μm (pore-free zone) within all three *SPOTS*. Cracks of depth of few micrometers are recognisable in the surface layer.

- #**7-u** Same features as in case of the previous sample can be recognised. Pores present within the sample are slightly larger in the proximity of the surface. Domains of same orientation can be found within slightly larger depth in comparison with the previous specimen.

Recapitulation of results

- Features of the fabrication parameters are reflected in the results rather than the dependence on the grain size only.
- Synergistic effects of simultaneous loading can be recognised within samples #1, #2 and #6. This is reflected in the increased grain size within the corresponding *SPOT*. This effect is not pronounced in case of sample #3. No explanation so far in terms of fabrication parameters, irradiation procedure etc. can be found for this exception.
- It seems that cyclic trapping and de-trapping of deuterium affects the heat propagation within the loaded area. This is reflected in the features of the correspondingly loaded *SPOT*.
- Depth of recovery zone seems to be independent of grain size in polished samples.
- Unpolished samples show formation of defect-free domains of size of few micrometers in the vicinity of the loaded surfaces. Those were formed deeper in the near-surface layer in case of sample with larger grains. No particular dependence on loading sequences can be recognised.

2.5.6 Retention of deuterium in W-SPS sample set

The amount od retained hydrogen isotopes within candidate PFCs represents a key factor in the fusion-oriented material research. W-SPS samples were stored approximately 16 days at RT in ambient atmosphere before the analysis of retained post-exposure deuterium concentration was performed. Despite the fact that samples were exposed to pure D-plasma, hydrogen H could stick to the surface when present in the air. Signal corresponding to hydrogen atoms was detected within the full set of W-SPS samples and *SPOTS*. Results of the ERDA measurement are listed in Tab. 2.10. Two distinct regions can be distinguished: the surface layer and a bulk region, the latter located in depth of z = (50 - 80) nm. Hydrogen content was determined only for the surface layer, since its content within the deeper region is assumed to be irrelevant for the analysis.

As can be seen in the corresponding table, hydrogen content within the surface layer of the reference *SPOTS r* decreases both with the grain size and surface roughness. This is an unexpected trend, since the larger the surface (caused by presence of hills/valleys reflected in the roughness S_a), the more hydrogen atoms can in principle stick to the surface layer. This assumption is confirmed in comparison of hydrogen content in surface layers of samples #3 and #3-u. On the other hand, hydrogen could in time diffuse within the near-surface region and be trapped in the lattice defects, or in the cavities (pores). Density within the near-surface layer of the latter showed to decrease with increasing grain size. Ratio of hydrogen concentration between the reference and loaded spots shows an interesting behaviour. In case of two samples with the smallest grains, the H content within loaded *SPOTS* exceeds that in the reference areas by a rather significant factor. The same applies to sample #4, but here the cracks, not present in reference area, could serve as hydrogen traps. On the other hand,

sample #	*SPOT*	$H_{sur} \cdot 10^{15}$ [cm^{-2}]	$D_{sur} \cdot 10^{15}$ [cm^{-2}]	$D_{bulk} \cdot 10^{15}$ [cm^{-2}]
1	r	67	-	-
	A	95	0.28	0.33
	B	91	0.21	0.34
	C	81	0.16	0.34
2	r	53	0.47	0.14
	A	81	0.39	0.38
	B	78	0.16	0.28
	C	57	-	-
3	r	21	-	-
	A	22	-	-
	B	26	-	0.04
	C	21	-	-
4	r	22	-	-
	C	36	0.17	-
5	r	20	-	-
	C	15	-	-
6	r	23	-	-
	A	25	-	-
	B	38	-	0.06
	C	35	-	-
3-u	r	50	0.51	1.0
	A	24	-	-
	B	33	-	0.45
	C	26	-	0.06
7-u	r	47	0.47	0.91
	A	18	-	-
	B	34	0.24	0.84
	C	18	-	-

Table 2.10: Results of ERDA measurement.

hydrogen present in laser loaded areas within the unpolished samples is lower than that in the reference spot. Largest hydrogen content can be found in *SPOT B*, corresponding to simultaneous loading.

But more important is the deuterium content within the samples. Concentration of retained deuterium atoms in the samples in many cases did not exceed the minimum detectable limit. Those cases are marked by '-' sign in Tab. 2.10. However, important information can be gathered even in that case.

Firstly, considering only the polished samples, the largest amounts od D were detected in the two samples with the lowest grain size. Large amount of pores present in the near-surface region could serve as trap. Interesting is the relatively high deuterium concentration in reference region of sample #2 and its absence in the same region in case of sample #1 (and all other polished samples). As indicated the values of microstrain listed in Tab. 2.9, lattices were more distorted due to plastic deformation in sample #2 (except of *SPOT B*). Solute deuterium atoms could distort the lattices to larger extent in case of this sample. But the retention itself in reference areas of this sample remains unclear. The only other difference between these reference areas and the others lies in the presence of stripe-like areas in the near-surface region, observed in the cross-sectional view. Those were supposed to be residuals of the pre-experimental treatment, with no apparent physical meaning. Nevertheless this opinion might be revised. Same structures were found in unpolished samples, which show relatively large concentration of surface and in-bulk retained deuterium as well.

Sample #1 is the only one that exhibited presence of detectable amount of deuterium within all three loaded areas. In principle this might be explained in terms of pores present in relatively large concentration, serving as trap both for hydrogen and deuterium. Larger deuterium concentration was found in the bulk region. Neutrals present in the plasma beam could enhance the deuterium de-trapping through Langmuir-Henshelwood recombination at the surface.

Beside the inexplicable presence of deuterium within the reference *SPOT r* (in the context of lack od deuterium within the reference spots of other polished samples), specimen #2 shows an interesting dependence of deuterium concentration on loading sequence. Most deuterium is retained in *SPOT A*, while none is detected in *SPOT C*. Thermal transient pulses during the loading sequence c) could act as de-trapping triggers. Trace amounts of deuterium can be found in samples #3 and #6 within *SPOTS B*. Probably thanks to cracks formation, deuterium was retained in surface layer of sample #4.

Worth noticing is also the deuterium concentration within the *SPOTS B* of the unpolished samples. Previously shown results exhibited so far inexplicable tendencies in terms of crystalline size, microstrain etc. for increasing grain size in case of this pair of samples. Decreased concentration of hydrogen within the surface layer can be found in case of sample #7-u in comparison with specimen #3-u. However more interesting is the only detectable amount of retained hydrogen within the *SPOT B* corresponding to loading sequence b). It has been shown previously that decreased crack density appeared in case of these *SPOTS*, more pronounced in case of sample #7-u. In this section it is shown that deuterium got trapped within these areas.

Recapitulation of results

- Concentration of hydrogen in the surface layer was found to be inversely proportional to the surface roughness in case of polished surfaces.
- Appearance and role of stripes-like structures parallel to surface, observed in both unpolished samples and one polished sample is unclear. Relatively large concentration of retained deuterium is linked with those structures.
- Sample with the smallest grain size contains detectable amount of deuterium within ale three loaded *SPOTS*, as the only one of the samples set. Deuterium thus remains trapped even in the area loaded by sequence c). Sample differing solely by larger grain diameter, showed deuterium release from this area.

2.5.7 Evaluation of post-irradiation mechanical properties

Combination of all factors - plastic deformation accompanied by roughening, impurity (deuterium) content, recovery, recrystallization and enlargement of pores can be reflected in changed mechanical and thermal properties of the as-fabricated component. Hardness, as a representative mechanical property, was measured on selected set of samples both on the irradiated side and on the side of the sample that was not affected neither by D-plasma or laser pulses, in order to provide an absolute reference number. Two samples were selected - sample #1, with the smallest grains, since this specimen showed as the only one the absence of slip bands or cracks in the loaded areas (small cracks in *SPOT A* are neglected) and sample #5, sintered for 60 minutes (resulting in relatively large grains), but showing no content of tungsten carbide. Results are summarized in Tab. 2.11.

sample #	*SPOT*	HV0.1
1	no plasma	477 ± 6
	r	406 ± 5
	A	375 ± 6
	B	373 ± 8
	C	376 ± 7
5	no plasma	$\sim 1500 - 2000$
	r	400 ± 6
	C	389 ± 7

Table 2.11: Microhardness of samples #1 and #5. Results are reported in a standardized form given by Eq. 2.4.

Results show that due to recovery of as-prepared deformed grains under D-plasma loading, hardness of sample #1 was decreased by 15% within the *SPOT r*. Hardness was further decreased due to further lattice defect recovery and possibly grain growth accompanying recrystallization. In the end, hardness was decreased to $\sim$ 80% of the absolute, un-irradiated reference hardness. No difference in hardness can be recognised within the *SPOTS* differing by loading sequence.

Hardness of the reference *SPOT r* of the second sample #5 is within 1σ consistent with the reference of sample #1. However the mean value is decreased, reflecting the increased grain size in case of this sample. Change in hardness of area loaded by cyclic thermal shocks is not so large as in the case of sample #1. Hardness of completely unloaded area was found to be surprisingly high. Such values correspond to presence of very hard tungsten carbides. Those could be formed as a consequence of carbon diffusion through the volume of the sample during the long sintering time.

Recapitulation of results

- Hardness, as a representative mechanical property, was measured within a selected set of samples.
- Sample with smallest grain diameter showed a decrease in hardness by 15% in areas loaded by D-plasma and by 20% in areas loaded also by transient heat pulses.
- Due to possible presence of carbides in the unloaded part of the sample, no absolute reference in terms of hardness could be provided in case of specimen #5. Hardness was slightly decreased when loaded by transient thermal shocks in case of this sample.

2.6 Summary of the experimental campaign

Set of tungsten samples with variable grain size was successfully prepared by SPS. Since components prepared by this method might find their application in future fusion reactors, fabricated samples underwent loading by plasma particles and thermal shock pulses, simulating thus the conditions within the tokamak. Exposure was performed at FZ-J, at PSI-2 linear plasma device, equipped with Nd:YAG laser. Density and temperature of the deuterium plasma corresponded to edge plasma conditions within tokamak, heat pulses produced by the laser simulated, in terms of absorbed power and frequency, ELMs, transient events that occur in tokamak with plasma confined in H-mode. Absorbed power was set to a level to produce apparent damage of the tested samples. Three different loading sequences were realized during the exposure procedure in order to study synergistic effects of simultaneous loading of samples by plasma species and high-energy heat pulses. Part of the samples was polished prior to the exposure, part left in ground state in order to evaluate the influence of polishing on subsequent performance of samples during the irradiation. Post-mortem analysis of the irradiated samples consisted of usage of various analytical methods, that provided a complex picture about the mechanisms that took place during the specimens irradiation. Main outcomes of the analysis can be summarized as follows:

- It was clearly shown, through investigation of reference regions, that the as-fabricated areas were plastically deformed (through slip along GBs) and recovered during the loading by D-plasma. Size of crystallites, i.e. coherently diffracting domains was increased and microstrain, indicating lattice distortion, was decreased as a consequence of loading by plasma species. This

clearly indicates that originally deformed as-fabricated grains underwent the above mentioned processes. Recovery of lattice defects was reflected in decrease of as-fabricated hardness of the component.

- Polished regions loaded by transient heat pulses showed two distinct types of damage features. Irradiated areas were plastically deformed, which was reflected in increased roughness with respect to the reference surfaces. Stresses induced by thermal expansion of the grains were further relaxed either through enhanced slip along GBs, crack formation or formation of ridges-like structures within the grains.

- Ridges-like structures were probably formed through activation of slip systems within the individual grains. Analogy to deformation of polycrystals under tensile/compressive forces can be found. Typical notch structures, associated with the slip bands formation, served probably as nucleation sites for appearance of fatigue cracks. Extrusion and intrusions of approximately the same depth were found within the slip bands, indicating a possible point defect migration during the cyclic heat loading.

- Slip bands showed irregularities in their parallelism. ECCI revealed presence of in-grain defects that might be responsible for this violation.

- Dense crack network was developed within one of the polished samples due to presence of tungsten carbides. Those were formed during the sample fabrication process and led probably to embrittlement of the specimen and reduction of DBTT.

- The sample with smallest grains showed no crack or slip band formation. Stress relaxation was realized through enhanced slip along GBs, reflected in relatively large roughness of the loaded areas.

- Average size of coherent domains and level of microstrain show slight decreasing and increasing dependence on grain diameter, respectively.

- No molten structures were found on the surface of the samples, with an exception of few apparently molten structures. Those were probably formed during deposition of protective metal layer prior to one of the experimental investigation.

- Pores, residual structures of the sample fabrication, were found within the bulk of the samples. Their concentration depends on the fabrication parameters. Size of the pores was increased in the vicinity of the loaded surfaces, indicating enhanced diffusion of point defects. Those regions could serve as concentration sites for trapped deuterium, which might further increase their size.

- Grains were recovered up to depth of few tenths of micrometers.

- Unlike was the case of polished sample, cracks were developed in the unpolished specimen. Residual grooves must have served as plastic deformation inhibitors and crack nucleation sites.

- Unpolished reference surfaces showed large affinity to deuterium retention.
- Beside the crack formation, regions of small recovered areas were found in the near-surface layer in case of unpolished samples.
- Combined optical, SEM metallography both of loaded surfaces and cross-sectional regions and ERDA measurements revealed synergistic effects of the simultaneous loading by D-plasma and transient pulses.
- It seems that cyclic transient loading, leading to enhanced deuterium migration and repetitive deuterium de-trapping led to decrease of thermal conductivity within the bulk, resulting in enhanced grain growth in the surface layer.

Comparison of the here listed results with the previously tested ITER-grade tungsten samples (irradiated at FZ-J) can be made. At BT set to 400 °C no blisters, indicating hydrogen embrittlement, were found, no cracks were developed, no dependence on loading sequence was found, as is listed in Sec. 2.1. In case of here tested polished W-SPS samples, no major or minor cracks were formed (except for polished cracked sample that is excluded from the discussion because of the carbide content). However, submicrometer fatigue cracks were formed, following the in-grain slip system activation. Elongated shape of grains could suppress the slip band appearance, although the dimensions of grains was substantially larger than in here reported case. While in ITER-grade samples no synergistic effects were found at the above mentioned BT, those were reflected, probably in heat propagation within the bulk, during this experimental campaign. .

3. Next step experiments - study and online monitoring of erosion of W samples exposed to COMPASS-D tokamak plasma

With initiation of PSI experiments at COMPASS-D, necessity to provide suitable experimental set up arose. This will be described in the first section of the chapter. Description of the experiment will follow, including the parameters of the tested sample, characterization of a typical COMPASS-D discharge and the main outcomes of the post-mortem analysis performed on the irradiated samples. Results of data analysis concerning the spectra recorded during the experiment will be then presented. Finally, realization of erosive PSI experiments at COMPASS-D from a general point of view will be discussed at the end of the chapter.

3.1 PSI experiments at tokamak COMPASS-D

PSI studies were initiated at COMPASS-D during the year 2013 by installation of a sample manipulator, providing both support and positioning within the tokamak chamber of several specimens at once. In the following subsections, parameters both of the tokamak and manipulator will be introduced.

3.1.1 Parameters of the tokamak

COMPASS-D tokamak was initially operated in British Culham Science Centre, but during the year 2006 it was moved and installed at IPP CAS in Prague. This tokamak is rather small in comparison with other similar devices (with plasma volume just about ~ 0.5 m^{-3}). On the other hand, COMPASS-D is equipped with a D-shaped vacuum vessel (from here the '-D' in its name) and is able to produce diverted plasma and achieve the H-mode. In general, H-mode can be achieved within plasma heated solely by Ohmic heating or with the help of NBI heating [129]. Schematic overview of this device, together with its main parameters, can be found in Fig. 3.1. Tokamak COMPASS-D is equipped with a comprehensive set of diagnostics (such as fast visible cameras, interferometers, Langmuir probes, fast bolometers, spectrometers in various wavelength range and many others [128]) that monitors the required plasma parameters during the dedicated experimental campaigns with high temporal and spatial resolution. Various plasma shapes can be formed with the correct set up of the magnetics: circular, elongated or single null X-point (SND) [129]. The latest is characterised by the intersection of the magnetic field lines in the shape of a letter 'X' (clearly distinguishable in Fig. 1.13). Component of poloidal magnetic field equals zero at the X-point. Magnetic field lines forming X-point are the last ones that are closed (not intercepting the wall) and the magnetic surfaces formed by these particular lines form the so called magnetic separatrix [130].

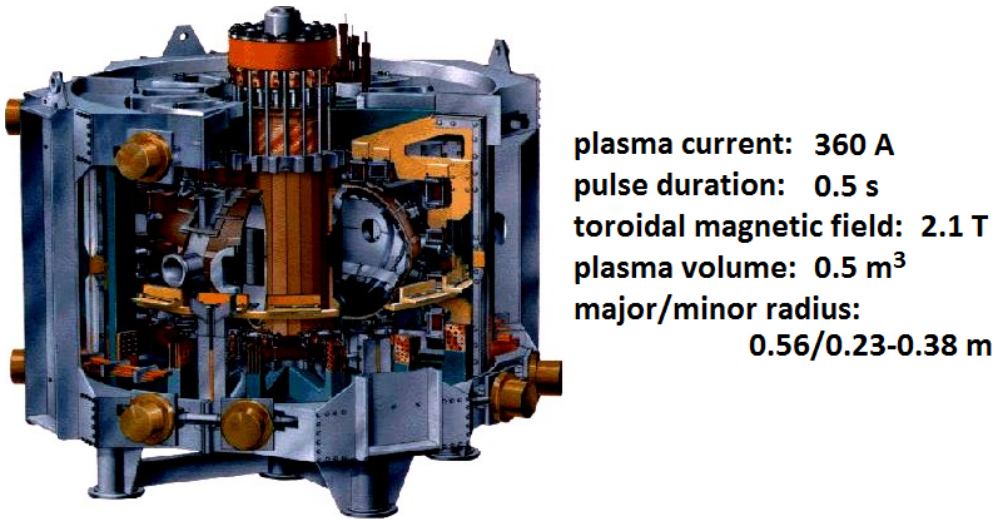

Figure 3.1: Schematic overview of tokamak COMPASS-D. Parameters of the device are given on the right side of the figure.

Divertor tiles of tokamak COMPASS-D are made of carbon. The vacuum vessel first wall material is a nickel-chromium alloy Inconel 625 (see the composition in Tab. 3.1). This particular alloy shows a superior strength and good resistance against corrosion [131].

Element	Ni	Cr	Fe	Mo	Nb + Ta	C	Mn
wt.%	> 58	20-23	< 5.0	8.0-10	3.2-4.2	< 0.10	< 0.50
Element	Si	F	S	Al	Ti	Co	
wt.%	< 0.50	< 0.015	< 0.015	< 0.40	< 0.40	< 1.0	

Table 3.1: Composition of Inconel 625 [131].

Beside the first wall material and graphite tiles, diagnostic ports/pins are physically present within the vacuum chamber. Those are often made of graphite, various ceramics of for example boron nitride. As working gases, hydrogen, deuterium and helium are typically used during the experiments in COMPASS-D.

3.1.2 PSI manipulator

For the purpose of PSI experiments, specimen manipulator, whose photograph can be found in Fig. 3.2 (right), was installed within the COMPASS-D vacuum chamber. Manipulator enters the chamber vertically from the bottom of the vessel. Its location is at the so called high-field side (HFS) of the vacuum chamber (referring to the fact that the intensity of toroidal magnetic field B scales as $B \sim 1/R$, where R is the spatial coordinate pointing from the central axis of the torus towards the outer side chamber). Specimens are fixed in place by a graphite holder that shall shield particle impact on sample sides. For the purpose of samples erosion studies, a vertical manipulator, carrying spectrometer viewing the specimens in the vertical direction, was installed in the upper part of the tokamak chamber. Tested specimens can be inserted within the chamber by a

movement along vertical z-axis, up to a complete insertion within the edge plasma. Schema of the sample positioning within the vessel (including the spectroscopic set up) is given in Fig. 3.2 (left).

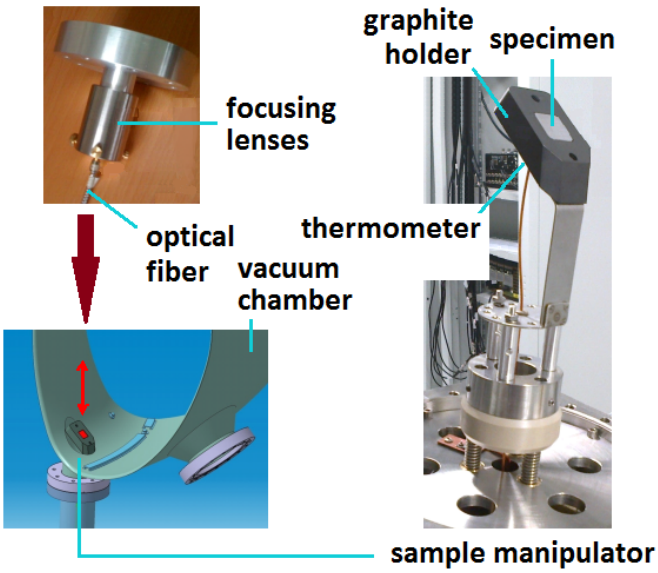

Figure 3.2: Sample manipulator set up. Spectrometer is viewing the sample vertically from the upper part of the vessel. With courtesy of Vladimír Weinzettl.

3.2 Description of the experiment

3.2.1 Experimental set up

For the purpose of erosion studies of possible candidate PFCs materials within the tokamak chamber of COMPASS-D, set of tungsten and steel P92 (see in Tab. 3.2) test specimens was prepared. Steel P92, might represent an alternative option as a plasma facing material due to its superior resistance against creep (thanks to content of tungsten and niobium). This steel found its application in power plants working with steam of high temperature and pressure [132].

Element	C	Mn	Si	S	P	Cr	Ni
wt.%	0.07-0.13	0.30-0.60	< 0.50	< 0.010	< 0.020	$<$ 8.5-9.5	< 0.40
Element	Mo	W	Nb	V	N	Al	B
wt.%	0.30-0.60	1.5-2.0	0.040-0.090	0.15-0.25	0.030-0.070	< 0.040	0.001-0.006

Table 3.2: Composition of steel P92 [132].

Carbon graphite R6710 [133] tiles, serving as a substrate for the tested materials, was shaped into a truncated pyramid (Fig. 3.3). Substrate tiles were covered by arc sputtering by tungsten layer of thickness 1.8 μm and by 2.6 μm layer of steel.

Samples were mounted on the manipulator and exposed to series of discharges in the tokamak chamber. Plasma parameters were tuned so that the plasma

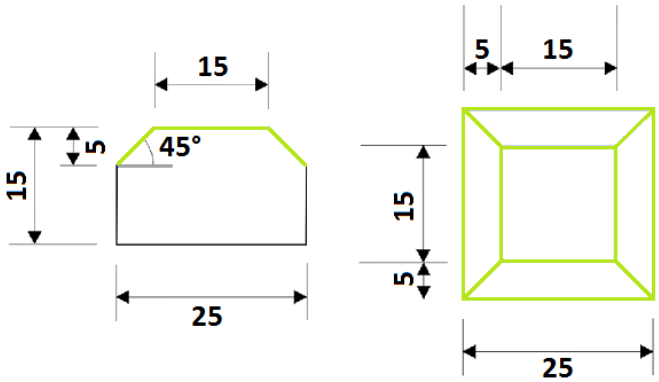

Figure 3.3: Side and top view on geometry of the tested samples. Surfaces covered by tungsten and steel are emphasized by green colour. With courtesy of Vladimír Weinzettl. Spatial unit of the scale is [mm].

would be preferably confined in the H-mode, accompanied by ELMs, producing thus bursts of heat and plasma impacting on the sample, causing the material to erode.

Experiments with the W specimen took place during the month of February 2014 (13/2 - 17/2). Sample was exposed to 27 discharges of pulse length $t_{pulse} >$ 50 ms. Parameters of the discharges (plasma current I_p, average particle density n and pulse length t_{pulse}) are listed in Tab. 3.3, together with some accompanying information concerning the discharge features. The above mentioned parameters are important in the context of the PSI. The amount of particles, causing the material loss through physical sputtering, is reflected in the density of the plasma species, larger plasma current affects the effective charge of the plasma etc. For simplicity, a simple proportionality in between the three parameters and level of sputtering can be assumed.

In all cases the plasma shape corresponded to the SND. Numbering of discharges (shots) corresponds to that used in the COMPASS-D tokamak department (counting shots from the beginning of the tokamak's operation).

Steel P92 was exposed to tokamak plasma during the December 2014, to 25 shots of $t_{pulse} >$ 50 ms, achieving the H-mode five times. Part of the H-modes were initiated by NBI heating.

shot #	I_p [kA]	$n \cdot 10^{19}$ [m^{-3}]	t_{pulse} [ms]	notes
6566	250	9.4	345	
6567	250	9.2	345	
6568	250	11.6	230	
6570	250	10.9	< 250	
6571	250	10.9	225	
6574	250	10.4	345	
6576	250	11.6	170	
6578	250	11.5	260	
6579	310	12.6	140	H-mode, 2 ELMs
6582	313	12.9	110	
6583	250	12.8	85	
6587	270	10.4	345	
6588	250	11.4	345	
6590	250	11.7	345	H-mode, no ELM
6592-3,5	250	11.7	345	
6596	250	11.8	230	
6598	326	11.9	110	
6601	230	7.6	70	
6602	360	10.2	250	H-mode, $>$ 40 ELMs
6603	350	10.9	180	H-mode, 7 ELMs
6604	306	11.4	260	H-mode, $>$ 50 ELMs
6605	306	11.6	270	
6607	307	11.6	140	H-mode, 3 ELMs
6608	250	11.6	230	H-mode, $>$ 30 ELMs
6610	306	13.5	255	

Table 3.3: List of COMPASS-D discharges during which the W sample was exposed to the tokamak plasma. Estimation of number of ELMs is possible thanks to drop in H_α intensity (see Fig.3.5).

3.2.2 Description of distinct phases of a COMPASS-D discharge

COMPASS-D discharges during which H-mode is achieved typically consist of several phases. As an example of a typical discharge, a time evolution of shot #6604 will be followed, Fig. 3.4. After evacuating the vacuum vessel to a sufficiently low level of vacuum, gas is puffed inside the chamber. After first plasma breakdown, induced by the transformer effect, working gas is practically fully ionized within just ~ 1 ms thanks to the avalanche effect. At the shot initiation,

plasma shape is circular, delimited by the so called limiters located at the central column (Fig. 3.4, upper left). Plasma is then elongated with the help of shaping coils to create a D-shaped plasma column (Fig. 3.4, upper right). Plasma is further shaped until the SND plasma with the X point is achieved ((Fig. 3.4, lower left, note the field lines intercepting the divertor tiles). When proper conditions are attained, plasma can pass to the high confinement mode. Shot #6604 was terminated by a disruption, last picture in the illustrative figure (Fig. 3.4, lower right), shows the plasma position just $\sim$ 2 ms before the discharge termination by disruption.

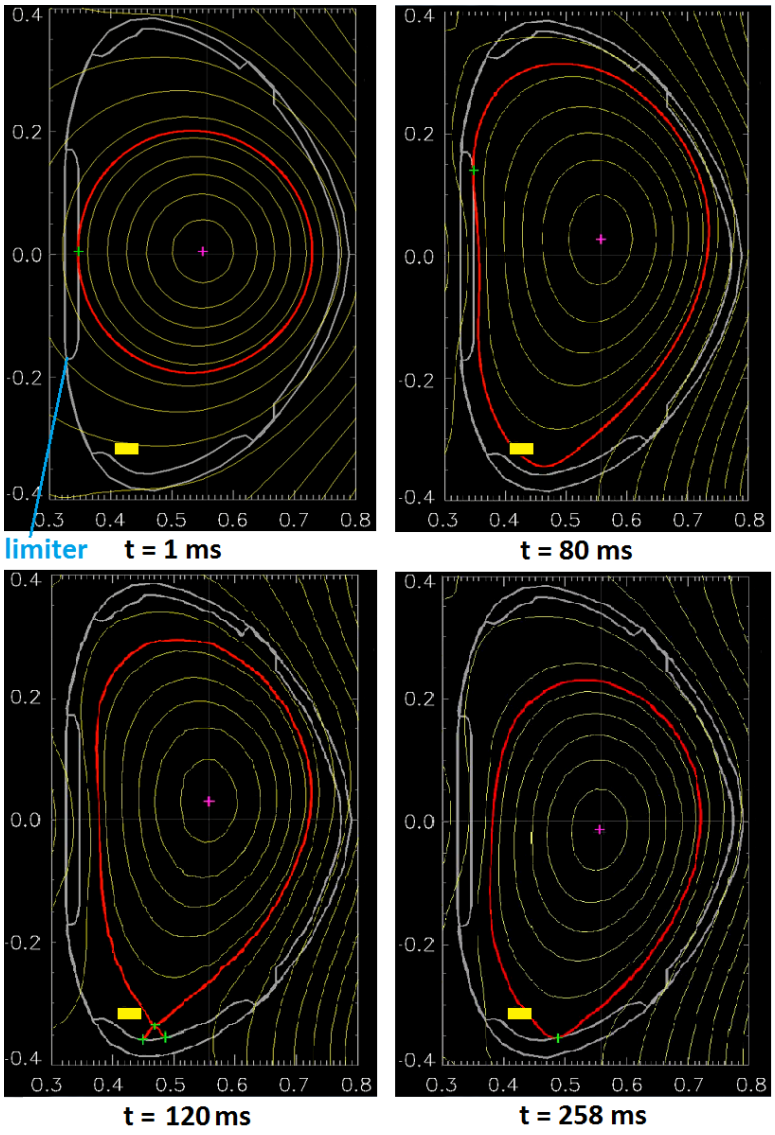

Figure 3.4: Time evolution of magnetic field lines configuration during the discharge #6604 [135], reconstructed by EFIT [134]. Separatrix is depicted by red line. Note the position of the tested sample (yellow rectangle). Full record of the reconstruction can be found in the Attachments, file DISCHARGE_6604.avi'.

Time evolution of plasma current and average plasma density during the representative shot #6604 are shown in Fig. 3.5. Full predefined plasma current is achieved after a ramp-up phase of typical duration of $\sim$ 100 ms. Transition to H-mode is most easily viewed through monitoring of H_α ($p = 3$ and $q = 2$, Eq. 1.11)

intensity thanks to the effect known as recycling [136], i.e. trapping and release of particles (fuel, impurities..) impinging on the chamber's first wall. Neutral hydrogen leaving the wall becomes excited in the edge region and emits light. Intensity of the emitted light is proportional to the released hydrogen. Drop in H_α intensity reflects that during H-mode plasma shows better confinement and impact of plasma species on the first wall is reduced. Exception are ELMs, during which bursts of heat and particles are released towards the vessel wall [129].

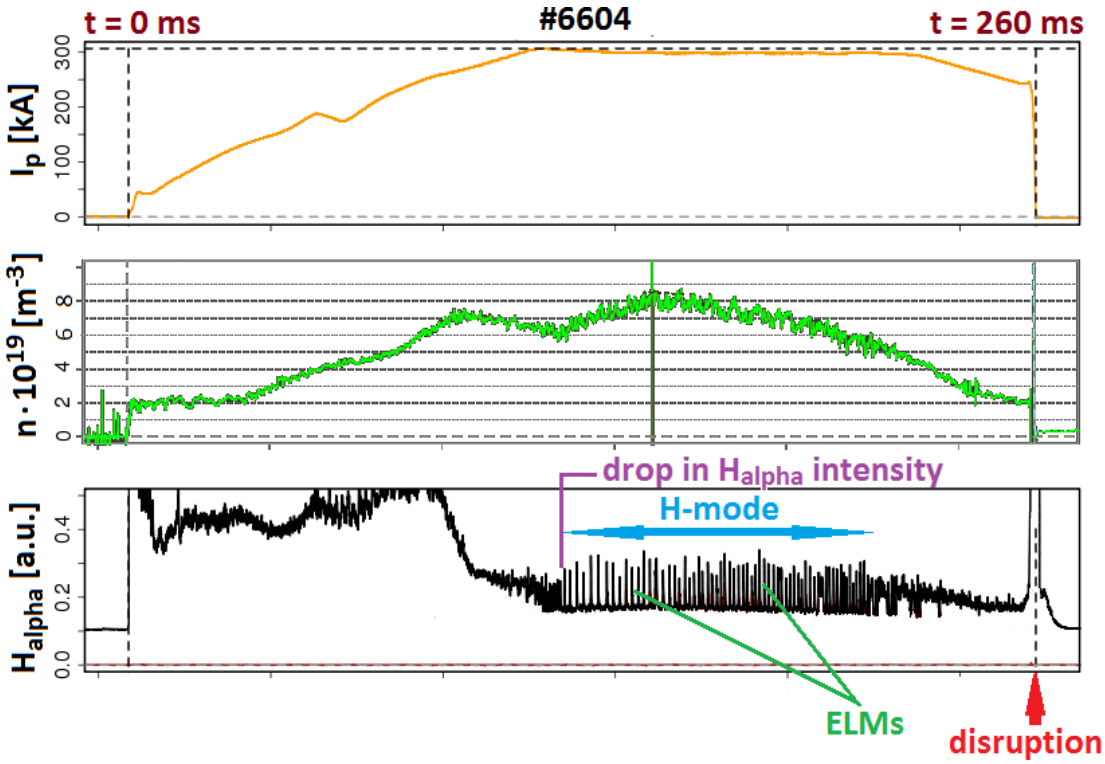

Figure 3.5: Time evolution of plasma current, average plasma density and H_α intensity during the shot #6604 [135]. Transition to H-mode is clearly distinguishable thanks to sudden drop in H_α intensity. ELMs are identified as sharp burst in the H_α emission.

Discharge #6604 was suddenly terminated by a disruption, just as majority of the other shots listed in Tab. 3.3. Disruptions, with the associated particle and energy release, could enhance thus the erosion of the tested sample.

Possible rise of sample temperature, as a consequence of exposure to tokamak discharge, was monitored by a thermomether that was in a direct contact with the sample, Fig. 3.2. However the rather long heating-up period (of the order of tenths of minutes) of the sample indicates a possible imperfect thermal contact with the samples. Temperature measurements are thus not included in the following discussion.

3.2.3 Results of the post-mortem analysis

Analysis following the samples removal from the tokamak chamber consisted of evaluation of post-mortem samples thickness by means of Rutherford back-scattering (RBS), observation of surface morphology by SEM and measurement of deuterium content by ERDA. Thickness of the exposed samples turned out not be significantly decreased, indicating rather low erosion of the material. Slightly

larger erosion was found on the truncated edges od the sample (where particles could impact on surface under higher angle). Steel sample was slightly more eroded than the tungsten specimen. However, material was found to be completely removed on few isolated spots, which is thought to be a consequence of the unipolar arcing ignition[1].

During the PSI experiments with the tungsten and P92 steel samples, erosion was aimed to be monitored through detection of the emission lines originating from the sputtered, excited and possibly ionized atoms. For this purpose, near UV spectrometer HR2000+ Ocean Optics [137] with a $247.6 - 472.0$ nm range of detection, time resolution of > 2 ms and optical resolution of ~ 0.1 nm was used. Spectrometer was calibrated absolutely prior to the experiment, allowing thus a possible determination of impurity concentration in the subsequent data analysis. Following section will present results of the analysis of spectroscopic measurements.

3.3 Analysis of spectroscopic data

3.3.1 Reference spectra

Large variety of elements (originating from the material of the vessel wall, diagnostic ports, impurities etc.) is present within the tokamak vessel, and all of them can be in principle excited (and/or ionized) during the discharge. Prior to the experiment, spectra were recorded during series of discharges without any inserted sample, with the port being closed. Those spectra served as reference spectra. Example of a reference spectrum is given in Fig. 3.6. Included in the plot is an emission spectrum of a Fe calibration lamp, recorded with the spectrometer prior to its installation in the tokamak. Background, determined prior to the experiment, was subtracted from the spectrum.

Identification of elements emitting the particular emission line is a rather complicated process. First of all, relative intensity of the emission lines depends in the particular conditions of tokamak plasma edge both on the density and temperature of the colliding species. Explanation of this statement is beyond the scope of this work, however a detailed introduction to the topic can be found for example in [139]. In general, many emission lines of various ionization degrees are present within the wavelength range of the used spectrometer and within its resolution limit typically several candidate emitting elements can be identified for a particular emission line. NIST database [138] contains an extensive set of information (theoretical and experimental) concerning the emission lines (upper/lower levels, transition probabilities etc.). Important in the context of this work, beside the identification of transition upper/lower levels (and determination of emitted photon energy), it provides the possibility of simulating relative intensities of emission lines. As an input for the simulation code, electron density and temperature (and, if different, ion temperature) shall be provided. Although the simulation counts with a different plasma condition than that of the tokamak

[1]Reference of the post-mortem analysis outcomes: Private communication with Jiří Matějíček.

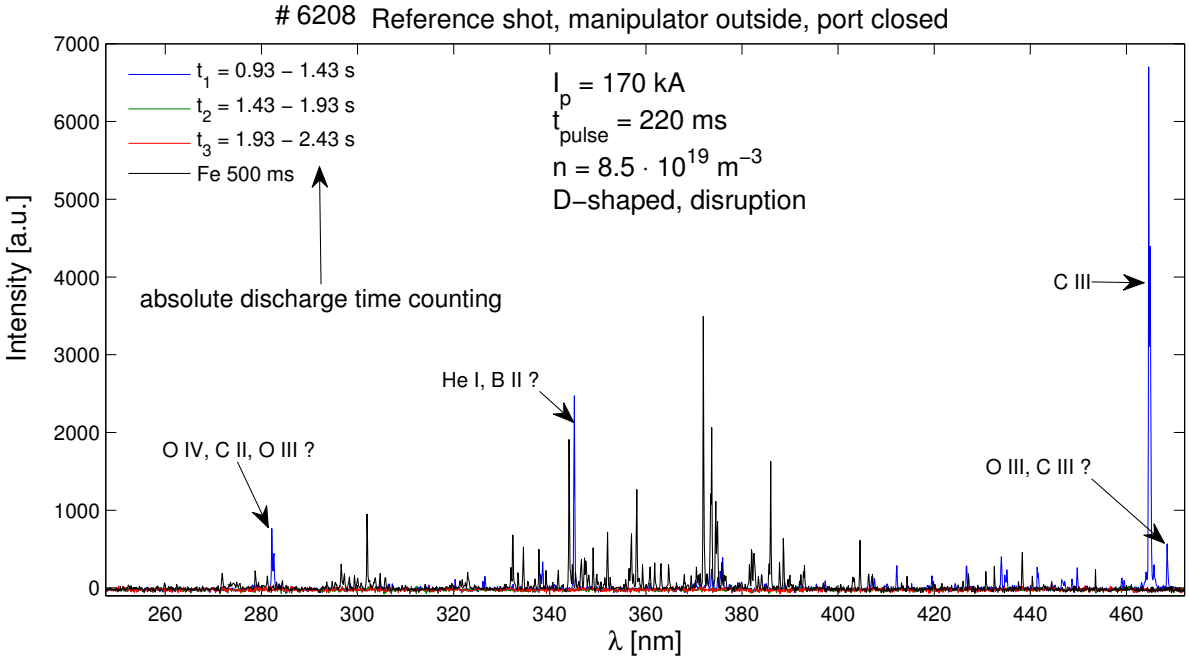

Figure 3.6: Example of reference spectrum, with no test PSI sample inserted within the vacuum chamber. Example of shot #6208. Some of the candidate emitting elements are included in the graphic.

plasma edge, the output of the simulation can serve as a certain support in the line identification process.

Following elements (and the corresponding ionization degrees) were identified within the reference spectra:

- D I, H I, O I-V, Hg I, C I-V, N I-V, B I-IV, He I-II, Ar I-II.

However, it is possible that eroded parts of the vacuum vessel wall could migrate in the line-of-sight of the spectrometer and contribute to the emission spectrum as well. Elements present in the Inconel 625 the shall be considered as candidate elements too.

3.3.2 Identification of tungsten emission lines

Since the here presented analysis is focused on erosion of the W sample, the emission spectra recorded with steel P92 sample inserted in the vacuum chamber serve as a reference point for the analysis as well, because the content of tungsten within this particular material is very low (just wt.%1.5-2.0, Tab. 3.2). Together with the reference spectra introduced in the previous subsection, the possible element candidate list became rather robust:

- D I, H I, O I-V, Hg I, C I-V, N I-V, B I-IV, He I-II, Ar I-II, Ni I-II, Cr I-II, Fe I-II, Mo I-II, Nb I-II, Ta I-II.

In case of metals, only neutral atoms and ions of ionization degree up to +1 were taken into account due to cold nature of the edge plasma.

During the analysis of reference and steel P92 spectra, some additional information concerning the COMPASS-D operation contributed to the clarification of

the origin of the emission lines. Wall conditioning procedures, such as DC glow discharge (GDC) and boronization, are routinely applied in order to improve the plasma confinement via reducing the impurity content within the plasma. The first relies on application of DC current (flowing between one or several anodes inserted into the chamber, and the vessel wall serving as a cathode [140]) leading to the formation of low-temperature plasma reducing carbon and oxygen content on the chamber wall. During the boronization, boron or carbon-boron hydrogenated films are deposited on the vessel wall in order to reduce the content of metallic impurities within the chamber. Moreover, carbon-boron layers serve as oxygen getter [141] and reduce carbon content within the vessel. COMPASS-D is typically boronized several times a year. Boronization took place 9/12/2014, during the steel P92 PSI campaign and the above mentioned advantageous aspects of reduction of impurity content within the vessel were taken into account during the analysis.

Finally, inspection of tungsten emission spectra yielded observation of a signal not present so far, that could in principle correspond to sputtered, excited atoms of the tested W sample. Wavelengths of the new lines were compared with the NIST database. In the end, 10 lines were identified as possibly originating from the tungsten sample, Tab. 3.4. However, it shall be emphasized here that in most of the cases other element could be present in the line-of-sight of the spectrometer during the discharge and emit the emission line as well.

candidate emission line	λ [nm]	discharge #
W I, Fe II	255.0	6604
W I, Fe II	258.9	6583
W I, Fe II	270.0	6604
W I	277.4	6574
W I, O IV	281.8	6578
W I, Fe I, O III	321.7	6578, 6582, 6598
W I, Mo I	326.3	6571, 6574, 6583
W I, Fe I, Mo I	334.6	6574
W I, Mo I	346.9	6571
W I, O II	417.0	6567

Table 3.4: Candidate tungsten emission lines. Corresponding discharges, in which the line appeared, are listed in the last column.

As the most promising candidate for the tungsten emission line appears that at $\lambda = 277.4$ [nm] (Fig. 3.7). Discharge #6574 contains in total 3 candidate tungsten emission lines. Nevertheless, it shall be stressed out that the result is not completely unambiguous. Other elements than those listed in the previous section could be present in the chamber (in form of a dust from the outside environment of the tokamak etc.)

Full list of the observed 487 emission lines can be found in the Attachments. Since identification of spectral lines is not completely reliable, it is thus ineffective (or even misleading) to use the absolute calibration data to calculate tungsten

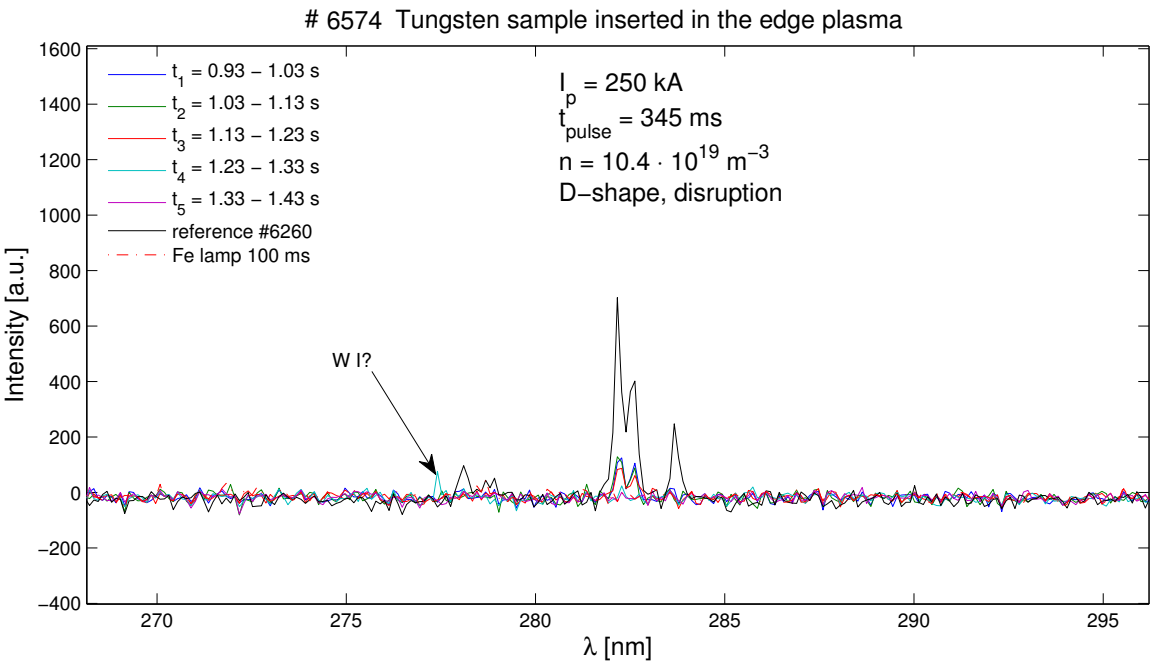

Figure 3.7: Candidate tungsten emission line at $\lambda = 277.4$ [nm]. Spectrum is compared with a reference spectrum #6260 (acquired prior to the PSI experiment) and the spectrum of Fe calibration lamp. Note that four consecutive spectra were recorded during the shot, offering the possibility to resolve distinct phases of the discharge. Blue line corresponds to phase of the end of the discharge, accompanied by a disruption.

concentration and make a decisive statement concerning the amount of material sputtered during the discharge.

3.4 Discussion of the results

No strong, unambiguously identifiable set of emission lines, originating from the tested sample, was found. In principle this might indicate that the spectra acquisition time was too short or that the spectrometer is of rather low sensibility. However, it shall be recalled that no extensive erosion (except of the localised spots of complete coating removal) of the deposited tungsten layer was found during the post-mortem analysis. This might therefore question the intensity of heat and particle fluxes during the COMPASS-D operation. One can recall the results of the experimental campaign presented in the previous section in which it was shown that a sample surface can be damaged after 100 heat pulses of power density equal to 0.76 GW/m^2. Tungsten sample investigated during the here reported experiment underwent 7 discharges in H-mode accompanied by more than $>$ 130 ELMs. It is possible to estimate heat fluxes to which the divertor region is exposed within the COMPASS-D with the help of a set of 39 poloidally aligned graphite Langmuir probes located in the bottom of the vessel, within the divertor tiles. It is not possible to measure the flux during the ELMs, because of the saturation of the signal, however heat fluxes in between the ELMs were determined during another set of PSI experiments (with the so called 'fuzzy',

nano-scale fibrous tungsten sample mounted on the manipulator and inserted in the plasma). It showed that the heat fluxes do not typically exceed values of $\sim 0.02 - 0.5$ MW/m^2 in between the ELMs (Fig. 3.8) [142].

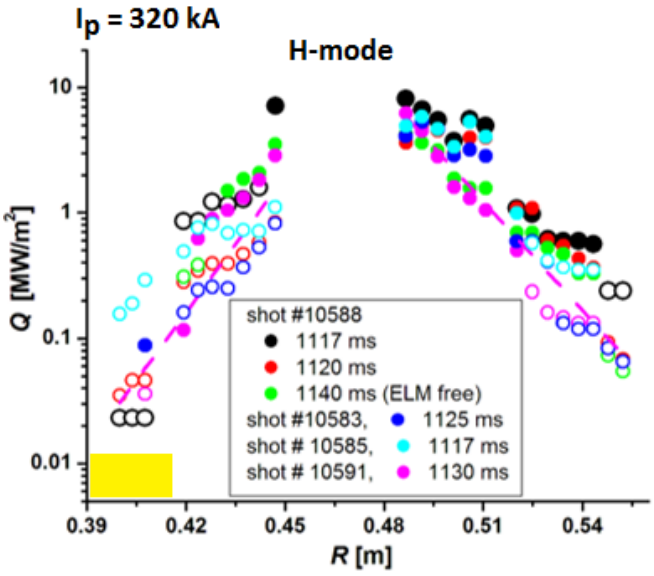

Figure 3.8: Example of heat flux radial distribution, measured by Langmuir probes during a discharge #10583, similar to those of the here presented experiment (in terms of plasma current and density). Heat flux is measured in H-mode, in between ELMs. Profiles are compared to a ELM-free discharge #10588. Radial position of the sample within the chamber is depicted by the yellow rectangle. With courtesy of Miglena Dimitrova.

3.5 Summary of the experiment

COMPASS-D operation showed to be compatible with insertion of test samples in the vacuum chamber for the purposes of PSI experiments, with a successful achievement of H-mode. For the purpose of erosion monitoring, full set up (manipulator at the bottom of the vessel, spectrometer viewing it from the top) was optimized to maximise the possible gain of information concerning the sample sputtering during the discharges.

Tungsten and steel P92 samples underwent series of tokamak shots, both samples were exposed to $>$ 120 ELMs during the PSI experimental campaign. Post-mortem analysis revealed no significant reduction of thickness of irradiated coatings, deposited prior to the experiment.

In case of analysis of spectra acquired during the W PSI campaign, spectroscopic measurements of steel P92 erosion served as reference point for the analysis, together with the absolute referential spectra, recorded with no sample present in the experimental chamber. No tungsten emission line was unambiguously identified during the data analysis.

Determination of heat flux in the divertor region of COMPASS-D during discharges similar to those presented in the scope of this experiment (in terms of plasma current and density) indicate that the heat fluxes during normal (and

probably also transient) events is possibly below the damage threshold limit, deduced for the tungsten grades.

Concluding remarks

Tungsten nowadays represents the most promising material in the context of development of PFCs of the fusion devices. As so, fusion material-oriented research is focused on selection of suitable fabrication techniques of the tungsten components. Various coating and bulk manufacturing methods are nowadays optimized in order to provide the best properties of the specimens in terms of their resistance to damage when exposed to the tokamak-like heat and particle loads. Special attention is paid to determination of thresholds for irreversible damage, since such damage leads to the necessity of component replacement during the maintenance phase.

Fabrication of components by means of SPS represents an attractive option in this context since both grain size and density (crucial parameters influencing the materials mechanical and thermal properties) of the manufactured element can be controlled by just tuning the sintering parameters.

Set of samples was prepared by SPS with the use of *commercially available* powders (including that of the smallest grain size). This means that the preparation of the samples set was rather simple, no pre-treatment of the as-received tungsten powder was performed.

Resistance of the samples to damage induced by steady-state loading by deuterium plasma particles and ELMs-like heat pulses was evaluated. Trends in the measured parameters were, if possible, correlated with the grain size, which represented the variable within the parameter scan. However, it seems that the dependence of the deduced quantities on the grain size is relatively weak. Rather than the grain size, *fabrication parameters* influence the subsequent sample performance under the heat/particle loading. As a representative example supporting this statement, the case of sample in which cracks appeared, unexpectedly in the context of the grain diameter scan, can be noted. It was only with the help of advanced analytical techniques that the presence of carbide was revealed within this sample. It appears clear that, beside the advantageous aspects of SPS, certain precautions that should be taken in consideration in future preparation of the samples. For example, a protective metallic layer could be installed between the graphite foil and tungsten powder within the graphite die, limiting thus the carbon diffusion in the fabricated specimen.

On the other hand, it seems that exception in the context of independence of deduced parameters on the grain size represents the activation of slip systems within the grains. Critically resolved shear stress is inversely proportional to the area on which the force is applied (2.17). In the context of this fact it can be deduced that the threshold value of grain diameter for the slip system activation, for transient loading by heat fluxes of 0.76 GW/m^2, is between the grain diameters of the two limiting cases, i.e. samples #1 and #2, $\sim 5.5 - 6.6$ μm.

Heat flux factor of the exposure was set to such a level that in principle no melting of the material should take place and no molten structures were observed on the irradiated surfaces. This fact indicates that the material was well densified during its manufacture, resulting in good thermal conductivity within the bulk. However, extrusions represent areas potentially more vulnerable to melting

because of reduced heat transfer towards the bulk volume. Appearance of those structures represent thus an unacceptable damage feature in the context of the tokamak PFCs.

It is generally considered that the dominant damage of the tested components is because of loading by high heat/particle fluxes. It is, of course, true. However here presented results show that the impact of moderate (in terms of density and energy) stream of deuterium atoms can lead to plastic deformation, accompanied by grain recovery, resulting in reduction of the hardness of as-prepared material. Caution shall be made in future when neglecting the impact of loading of the components by plasma species.

This experimental campaign showed the necessity of applying the polishing treatments on the as-prepared SPS components. In the context of tokamak PFCs, cracks of depth of several micrometers might enhance the fuel retention within the first-wall materials. Dust could be potentially released from the cracks. Large-scale manufacture of the samples will be thus necessarily prolonged by the polishing.

It is a general fact that the finer the grain diameter, the larger the hardness and strength of the material is. In principle this shall imply that the best resistance against damage induced by heat loads should be observed in case of the sample with the smallest grains. No slip bands or cracks were found in case of this sample, indicating the application and correctness of the assumption concerning the fine grain size and its impact on the material mechanical properties. Nevertheless, as was stated above, the set of here tested W-SPS sample was prepared, beside others, with the use of the smallest commercially available powder size. Improving thus further the SPS components properties will necessarily imply a pre-fabrication treatment of the tungsten powder (in terms of powder milling, for example), or addition of grain growth inhibitors, prolonging and complicating thus the time of the sample manufacture.

Combination of results of several experimental techniques showed that synergistic effects of simultaneous loading by deuterium plasma and high energy heat pulses are important for SPS specimens even at the base temperature set to 400 °C, reducing thus the well known effect of hydrogen embrittlement. Proven reduction of heat propagation within the bulk during such loading represents an important outcome of this work.

In order to fulfil the ITER-grade specifications, SPS specimens could be in principle further machined to achieve the elongated grain geometry.

Simulation of tokamak-like conditions in plasma generator devices can never meet the extremely complex environment within the tokamak. Combination of magnetic and electric fields, flow of currents, impact of both fuel and impurity particles etc. can simply never be fully simulated outside of the fusion device. Test of perspective samples within the tokamaks represent thus a next step in the development of the materials for PFCs.

First erosive PSI experiments performed at COMPASS-D showed that the heat and particle fluxes within this device are probably too low to induce pronounced sputtering over large area. However, localised spots of removed coating indicate that unipolar arcing was ignited within this device.

Bibliography

[1] The Colorado River Comission of Nevada *World Fossil Fuel Reserves and Projected Depletion,* http://crc.nv.gov/docs/world/20fossil/20reserves.pdf [Online; accessed 10-May-2015].

[2] IEA *Key World Energy Statistics 2014,* https://www.iea.org/publications/freepublications/publication/KeyWorld2014.pdf [Online; accessed 11-May-2015].

[3] Boman, M. *Liquid Drop Model and the Semiempirical Mass Formula,* http://people.ifm.liu.se/boman/kvantfysik_larare/Liquid.pdf [Online; accessed 12-May-2015].

[4] NPL *Nuclear Fission and Fusion, and Neutron Interactions,* http://www.kayelaby.npl.co.uk/atomic_and_nuclear_physics/4_7/4_7_4a.html [Online; accessed 14-May-2015].

[5] Teller, E. *Fusion Part A: Magnetic Confinement* UK: Academic Press, Inc, 1981, 1.

[6] Farrell, M. *Tokamak: Future of Nuclear Power,* http://new.math.uiuc.edu/math198/MA198-2009/farrell1/ [Online; accessed 25-May-2015].

[7] ITER Physics Expert Group on Energetic Particles, Heating and Current Drive *Plasma auxiliary heating and current drive.* Nuclear Fusion, 39(12), 2495-2539, 1999.

[8] Wagner, F. et al. *Development of an Edge Transport Barrier at the H-Mode Transition of ASDEX.* Physical Review Letters, 53(15), 1453-1456, 1984.

[9] Wesson, J. *Tokamaks* USA: Oxford University Press, Inc., 2011.

[10] Sips, A.C.C. et al. *Progress in Preparing Scenarios for Operation of the International Thermonuclear Experimental Reactor.* Physics of Plasmas, 22(2), 2015.

[11] ITER Organization https://www.iter.org/gallery/com_image_download#411 [Online; accessed 11-August-2015].

[12] Shimomura, Y. *ITER and Plasma Surface Interaction Issues in a Fusion Reactor.* Journal of Nuclear Materials, 363-365, 467-475, 2007.

[13] Jacquinot, J. *JET Relevance to ITER, New Trends and Initial Results.* Fusion Engineering and Design, 30, 67-84, 1995.

[14] Linke, J.M. et al. *Performance of PFC Materials in Tokamaks and Stellarators.* Fusion Science and Technology, 46, 142-151, 2004.

[15] Pitts, R.A. et al. *Physics Basis and Design of the ITER Plasma-Facing Components.* Journal of Nuclear Materials, 415, 957-964, 2011.

[16] Loarte, A. et al. *Power and Particle Control.* Nuclear Fusion, 47, S203–S263 (Chapter 4), 2007.

[17] Wirtz, M. et al. *Impact of Combined Hydrogen Plasma and Transient Heat Loads on Performance of Tungsten as Plasma Facing Material.* Nuclear Fusion, 55, 123017, 2015.

[18] Bolt, H. et al. *Plasma Facing and High Heat Flux Materials – Needs for ITER and Beyond.* Journal of Nuclear Materials, 307-311, 43–52 (Section 2), 2002.

[19] Matejicek, J. et al. *Thermal Spray Coatings for Fusion Applications - Review.* Journal of Thermal Spray Technology, 16, 64-83, 2007.

[20] Scaffidi-Argentina, F. et al. *The Status of Beryllium Technology for Fusion.* Journal of Nuclear Materials, 283, 43-51, 2000.

[21] Wikipedia contributors `https://en.wikipedia.org/wiki/Carbon` [Online; accessed 15-December-2015].

[22] Fusion Power Associates `http://fpa.ucsd.edu/ARC12/fpn12-52.shtml` [Online; accessed 21-November-2015].

[23] Scaffidi-Argentina, F. et al. *Neutron Irradiation Effects on the Thermal Conductivity and Dimensional Stability of Carbon Fiber Composites at Divertor Conditions.* Journal of Nuclear Materials, 228, 155-161, 1996.

[24] Phillips, V. *Tungsten as Material for Plasma-facing Components in Fusion Devices.* Journal of Nuclear Materials, 415, S2-S9, 2011.

[25] Andrew, P. et al. *Tritium Recycling and Retention in JET.* Journal of Nuclear Materials, 266-269, 153-159, 1999.

[26] Franzen, P. et al. *Hydrogen Isotope Inventory in the Graphite Divertor Tiles of ASDEX Upgrade as Measured by Thermal Desorption Spectroscopy.* Nuclear Fusion, 37, 10, 1997.

[27] Fujita, I. et al. *Surface Analysis of JT-60 Graphite Divertor Tiles.* Journal of Nuclear Materials, 196-198, 168-173, 1992.

[28] Pitts, R. A. et al. *A Full Tungsten Divertor for ITER: Physics Issues and Design Status.* Journal of Nuclear Materials, 438, 48, 2013.

[29] Lassner, E., Schubert W.-D. *Tungsten: Properties, Chemistry, Technology of the Element, Alloys, and Chemical Compounds.* Springer Science & Business Media, US, 2012.

[30] Slattery, K.T. et al. *Development and Fabrication of ITER Divertor Cassette Body.* Fusion Engineering, 17th IEEE/NPSS Symposium, Volume 2, 1997.

[31] Hirai, T. et al. *ITER Tungsten Divertor Design Development and Qualification Program.* Fusion Engineering and Design, 88, 1798-1801, 2013.

[32] Merola, M. et al. *Overview and Status of ITER Internal Components.* Fusion Engineering and Design, 89, 890-895, 2014.

[33] Rodig, M. et al. *High Heat Flux Testing of Different Armour.* Presented at the International HHFC Workshop on Readiness to Proceed from Near Term Fusion Systems to Power Plants, San Diego, 2008.

[34] Loewenhoff, Th. et al. *ITER-W Monoblocks Under High Pulse Number Transient Heat Loads at High Temperature.* Journal of Nuclear Materials, 463, 202-205, 2015.

[35] Kaufmann, M. *Tungsten as First Wall Material in Fusion Devices.* Presented at the Symposium on Fusion Technologies, Warsaw, 2006.

[36] Coad, J.P. et al. *Testing of Tungsten Coatings in JET for the ITER-like Wall.* Proceedings of the 18th Plasma Surface Interactions in Controlled Fusion Devices, Toledo, 2008.

[37] Riccardi, B. et al. *Development of Tungsten Coatings for ITER Divertor Components.* Fusion Engineering, 17th IEEE/NPSS Symposium, Volume 2, 1997.

[38] Rusinov, A. et al. *Deuterium Trapping in Rolled Polycrystalline Tungsten Exposed to Low Energy Plasma.* Plasma and Fusion Research, 7, 1405105, 2012.

[39] A&A Coatings `http://www.thermalspray.com/` [Online; accessed 26-November-2015].

[40] Klevarová, V. *Interaction of tokamak plasma with selected fusion materials.* Bachelor thesis, Charles University in Prague, 2012.

[41] Matějíček, J. et al. *The Influence of Interface Characteristics on the Adhesion/Cohesion of Plasma Sprayed Tungsten Coatings.* Coatings, 3, 108-125, 2013.

[42] Huang, J. et al. *Transient High Heat Load Tests on Tungsten Coating by High-intensity Current Pulsed Electron Beam.* Journal of Nuclear Materials, 455, 412-415, 2014.

[43] Kuang, Z.Q. et al. *Study of Thick Tungsten Coatings Deposited on the Different Substrates.* Proceedings of the 2007 International Thermal Spray Conference, Beijing, 2007.

[44] Matějíček, J. *Vliv Neutronového Záření na Fúzní Materiály (s Přihlédnutím k Plazmovým Nástřikům).* Výzkumná Zpráva ÚFP, 1, 2008.

[45] Song, J. *Development of CVD-W coatings on CuCrZr and graphite substrates with a PVD intermediate layer.* Journal of Nuclear Materials, 455, 531-536, 2014.

[46] Zhu, D. *Thermal Stress Analysis on Chemical Vapor Deposition Tungsten Coating as Plasma Facing Material for EAST.* Journal of Nuclear Materials, 455, 185-188, 2014.

[47] Lian, Y. *Thermal Shock Performance of CVD Tungsten Coating at Elevated Temperature.* Journal of Nuclear Materials, 455, 371-375, 2014.

[48] Murphy, J.D. et al. *The Mechanical Properties of Tungsten Grown by Chemical Vapour Deposition.* Journal of Nuclear Materials, 386-388, 583-586, 2009.

[49] Ren, X-N. et al. *Proposal and Research on Using Tungsten Carbonyl-CVD Process for Making W-coating PFMs and W-tubes.* Journal of Nuclear Materials, 455, 582-585, 2014.

[50] Maier, H. et al. *Properties of Tungsten Coatings onto Fine Grain Graphite by Different Methods.* Surface and Coating Technologies, 142-144, 733-737, 2001.

[51] Philipps, V. et al. *Overview of the ITER-like Wall Project.* Fusion Engineering and Design, 85, 1581-1586, 2010.

[52] Ruset, C. et al. *Development of W Coatings for Fusion Application.* Fusion Engineering and Design, 86, 1677-1680, 2011.

[53] Hauzer TECHNO COATING `http://www.hauzertechnocoating.com/en/plasma-coating-explained/magnetron-sputtering/` [Online; accessed 29-November-2015].

[54] Ruset, C. et al. *Industrial Scale 10 um W Coating of CFC Tiles for ITER-like Wall Project at JET.* Fusion Engineering and Design, 84, 1662-1665, 2009.

[55] Garkusha, I.E. et al. *Performance of Deformed Tungsten under ELM-like Plasma Exposures in QSPA Kh-50.* Journal of Nuclear Materials, 415, S65-S69, 2011.

[56] Hirai, T. et al. *Cracking Failure Study of ITER-reference Tungsten Grade Under Single Pulse Thermal Shock Loads at Elevated Temperatures.* Journal of Nuclear Materials, 390-391, 751-754, 2009.

[57] Plansee Group `http://www.thermalspray.com/` [Online; accessed 29-November-2015].

[58] Lemahieu, N. *Performance of Yttrium Doped Tungsten Under ITER Relevant Transient Thermal Loads.* Master thesis, University of Ghent, 2012.

[59] Garkusha, I.E. et al. *High Power Plasma Interaction with Tungsten Grades in ITER-relevant Conditions.* Journal of Physics: Conference Series, 591, 012030, 2015.

[60] Garkusha, I.E. et al. *Tungsten Erosion Under Plasma Heat Loads Typical for ITER type I ELMs and Disruptions.* Journal of Nuclear Materials, 337-339, 707-711, 2005.

[61] Institute of Plasma Physics CAS, Department of Materials Engineering *Spark Plasma Sintering.* 2010.

[62] Matějíček, J. et al. *Mechanical and Thermal Properties of Individual Phases Formed in Sintered Tungsten-Steel Composites.* Acta Physica Polonica A, 128, 4, 2015.

[63] Liu, X. et al. *Tungsten Joining with Copper Alloy and its High Heat Load Performance.* Journal of Nuclear Materials, 455, 382-386, 2014.

[64] Merola, M. et al. *Overview on Fabrication and Joining of Plasma Facing and High Heat Flux Materials for ITER.* Journal of Nuclear Materials, 307-311, 1524-1532, 2002.

[65] Gavila, P. et al. *High Heat Flux Testing on EU tungsten Monoblock Mock-ups for the ITER Divertor.* Fusion Engineering and Design, 98-99, 1305-1309, 2015.

[66] Coenen, J.W. et al. *Tungsten Melt Layer Motion and Splashing on Castellated Tungsten Surfaces at the Tokamak TEXTOR.* Journal of Nuclear Materials, 415, S78-S82, 2011.

[67] Bazylev, B. et al. *Experimental and Theoretical Investigation of Droplet Emission from Tungsten Melt Layer.* Fusion Engineering and Design, 84, 441-445, 2009.

[68] Stephanie Terrade `http://hmf.enseeiht.fr/travaux/CD0001/travaux/optmfn/hi/01pa/hyb72/kh/kh_theo.htm` [Online; accessed 3-December-2015].

[69] Yuan, Y. et al. *Melt Layer Erosion of Pure and Lanthanum Doped Tungsten under VDE-like High Heat Flux Loads.* Journal of Nuclear Materials, 4381, S229-S232, 2013.

[70] Kim, H. et al. *Recrystallization of Bulk and Plasma-coated Tungsten with Accumulated Thermal Energy Relevant to Type-I ELM H-mode Operation.* Journal of Nuclear Materials, 463, 215-218, 2015.

[71] Rooij, G.J. et al. *Tungsten Divertor Erosion in All Metal Devices: Lessons form the ITER Like Wall of JET.* Proceedings of the 20th International Conference on Plasma Surface Interactions, Aachen, 2012.

[72] Barnard, H.S. et al. *A Study of Tungsten Migration in the Alcator C-Mod Divertor.* Journal of Nuclear Materials, 415, S301-S304, 2011.

[73] Maier, H. et al. *Erosion and Deposition in the ASDEX Upgrade Tungsten Divertor Experiment.* Journal of Nuclear Materials, 266-269, 1003-1008, 1999.

[74] Herrmann, A. et al. *Arcing in ASDEC Upgrade with a Tungsten First Wall.* Journal of Nuclear Materials, 390-391, 747-750, 2009.

[75] Kajita, S. et al. *Tungsten Blow-off in Response to the Ignition of Arcing: Revival of Arcing Issue in Future Fusion Devices.* Journal of Nuclear Materials, 415, S42-S45, 2011.

[76] Reichle, R. *Review of the ITER Diagnostics Suite for Erosion, Deposition, Dust and Tritium Measurements.* Journal of Nuclear Materials, 463, 180-184, 2015.

[77] Gauthier, E. *Progress in Diagnostics for Characterization of Plasma Wall Interaction in Tokamaks.* Journal of Nuclear Materials, 390-391, 1059-1065, 2009.

[78] Bethe, H.A. and Salpeter, E.E. *Quantum Mechanics of One- and Two-Electron Atoms.* USA: Dover Publications, Inc., 2008.

[79] Neri, C. *The Laser in Vessel Viewing System (IVVS) for Iter: Test Results on First Wall and Divertor Samples and New Developments.* Fusion Engineering and Design, 82, 2021-2028, 2007.

[80] Gauthier, E. *Real-time Erosion Monitoring in ITER by Means of Speckle Interferometry.* Journal of Nuclear Materials, 415, S1182-S1186, 2011.

[81] Roth, J. et al. *Tritium Inventory in ITER Plasma-facing Materials and Tritium Removal Procedures.* Plasma Physics and Controlled Fusion, 50, 103001, 2008.

[82] Loarer, T. et al. *Comparison of Fuel Retention in JET Between Carbon and the ITER-Like Wall.* Proceedings on 20th International Conference on Plasma Surface Interactions, Aachen, 2012.

[83] Markelj, S. et al. *Studying Process of Hydrogen Interaction with Metallic Surfaces in situ and in Real-time by ERDA.* Nuclear Instruments nad Methods in Physics Research, B 259, 989-996, 2007.

[84] Roth, J. and Schmid, K. *Hydrogen in Tungsten as Plasma-facing Material.* Physics Scripta, T-145, 014031, 2011.

[85] Markelj, S. et al. *In situ NRA Study of Hydrogen Isotope Exchange in Self-ion Damaged Tungsten Exposed to Neutral Atoms.* Journal of Nuclear Materials, in press, doi: 10.1016/j.jnucmat.2015.11.039.

[86] Markelj, S. et al. *Deuterium Retention and Isotope Exchange Studies in Self-ion Damaged Tungsten Exposed to Neutral Atoms.* Presented at IAEA CRP meeting, Seoul, 2015.

[87] El-Kharbachi, A. et al. *Tritium Absorption/desorption in ITER-like Tungsten Particles.* International Journal of Hydrogen Energy, 39, 10525-10536, 2014.

[88] Grisolia, C. et al. *Tritium Absorption and Desorption in ITER Relevant Materials: Comparative Study of Tungsten Dust and Massive Samples.* Journal of Nuclear Materials, 463, 885-888, 2015.

[89] Huber, A. et al. *Combined Impact of Transient Heat Loads and Steady-State Plasma Exposure on Tungsten.* Fusion Engineering and Design, 98-99, 1328-1332, 2015.

[90] Huber, A. et al. *Impact on the Deuterium Retention on Simultaneous Exposure of Tungsten to a Steady State Plasma and Transient Heat Cyclic Loads.* EUROfusion Preprints, Reports and Conference Papers, 2015.

[91] Global Tungsten & Powders http://www.globaltungsten.com/ [Online; accessed 7-December-2015].

[92] Thermal Technology LLC http://www.thermaltechnology.com/ [Online; accessed 7-December-2015].

[93] NPL Report MATC(A) 149 http://publications.npl.co.uk/npl_web/pdf/matc149.pdf [Online; accessed 14-December-2015].

[94] Waldmann, O. et al. *Anomalous Diffusion in a Linear Plasma Generator.* Contributions to Plasma Physics, 47, 1691-702, 2007.

[95] Huber, A. et al. *Linear Plasma Device PSI-2 for Plasma-Material Interaction Studies.* Fusion Science and Technology, 68, 8-14, 2014.

[96] Klevarová, V. *High-resolution Doppler Spectroscopy at Linear Plasma Device.* Master thesis, University of Ghent, 2015.

[97] Meyer, H. et al. *Plasma Rotation in a Plasma Generator.* Physical Review E, 61, 4, 2000.

[98] Kreter, A. et al. *Linear Plasma Device PSI-2 for Plasma-material Interaction Studies.* Fusion Science and Technology, 68, 8-14, 2015.

[99] Olympus Microscopy Resource Center http://www.olympusmicro.com/primer/techniques/dic/dichome.html [Online; accessed 11-December-2015].

[100] Englich, J. *Úvod do praktické fyziky I: Zpracování výsledků měření.* Czech republic: Matfyzpress, 2006.

[101] Goldstein, G.I. et al. *Scanning Electron Microscopy and X-ray Microanalysis* USA: Plenum Press, 1975.

[102] University of Glasgow http://www.gla.ac.uk/schools/ges/research/researchfacilities/isaac/services/scanningelectronmicroscopy/ [Online; accessed 13-December-2015].

[103] Zaefferer, S. and Elhami, N-N. *Theory and Application of Electron Channelling Contrast Imaging Under Controlled Diffraction Conditions.* Acta Materialia, 75, 20-50, 2014.

[104] Maitland, T. and Sitzman, S. *Electron Backscatter Diffraction (EBSD) Technique and Materials Characterization Examples* USA: Springer, 2006.

[105] Cullity, B.D. and Stock, S.R. *Elements of X-ray Diffraction.* USA: Prentice Hall, 2001.

[106] University of Cambridge http://www.doitpoms.ac.uk/tlplib/xray-diffraction/production.php [Online; accessed 15-December-2015].

[107] Monshi, A. et al. *Modified Scherrer Equation to Estimate More Accurately Nano-Crystallite Size Using XRD.* World Journal of Nano Science and Engineering, 2, 154-160, 2012.

[108] MIT Center for Materials Science and Engineering http://prism.mit.edu/xray/ [Online; accessed 15-December-2015].

[109] Balzar, D. *Voigt-function Model in Diffraction Line-broadening Analysis* University of Colorado, 1999.

[110] Veselý, J. https://linda.karlov.mff.cuni.cz/~jove/thesis/html/AFM.html [Online; accessed 16-December-2015].

[111] Bruker AFM Probes http://www.brukerafmprobes.com/p-3381-otespa.aspx [Online; accessed 16-December-2015].

[112] Giannuzzi, L.A. *Introduction to Focused Ion Beams: Instrumentation, Theory, Techniques and Practice.* USA: Springer Science & Business Media, 2006.

[113] Zygo Corporation *NewView 7200 & 7300 Operating Manual.* USA: OMP-0536, Rev. E, 2011.

[114] Wikipedia contributors https://en.wikipedia.org/wiki/Vickers_hardness_test [Online; accessed 17-December-2015].

[115] Kelemen, M. *Deuterium Depth Profiling with D-3He-p-alpha Nuclear Reaction.* University of Ljubljana, 2013.

[116] Bočan, J. *The Development of Time-of-flight Telescope for Elastic Recoil Detection Analysis.* Master thesis, Czech Technical University in Prague, 2007.

[117] NPI CAS http://vakspol.cz/lsvt07/mackova.pdf [Online; accessed 19-December-2015].

[118] Center of Accelerators and Nuclear Analytical Methods Nuclear Physics Institute of the ASCR http://canam.ujf.cas.cz/en/laboratory-of-tandetron-lt [Online; accessed 18-December-2015].

[119] Kellock, A.J. and Baglin, J.E.E. *Absolute Cross Section for D-4He-D-4He Forward Scattering.* Nuclear Instruments and Methods in Physics Research B, 47, 493-497, 1993.

[120] All-Foils, Inc. http://www.allfoils.com/single-product/metalized-polyester-mylar/ [Online; accessed 19-December-2015].

[121] Blott, S.J. and Pye, K. *Gradistat: A Grain Size Distribution and Statistics Package for the Analysis of Unconsolidated Sediments.* Eart Surface Processes and Landforms, 26, 1237-1248, 2001.

[122] WebElements http://www.webelements.com/tungsten/crystal_structure.html [Online; accessed 29-December-2015].

[123] Polák, J. et al. *AFM Evidence of Surface Relief Formation and Models of Fatigue Crack Nucleation.* International Journal of Fatigue, 25, 1027-1036, 2003.

[124] Pablo G. Careces http://academic.uprm.edu/pcaceres/Courses/MechMet/MET-3A.pdf [Online; accessed 29-December-2015].

[125] Polák, J. *On the Role of Point Defects in Fatigue Crack Initiation.* Materials Science and Engineering: A, 92, 71-80, 1987.

[126] Essmann, U. et al. *Model of Extrusions and Intrusions in Fatigued Metals I. Point Defect Production and Growth of Extrusions.* Philosophical Magazine A, 44, 405-426, 1981.

[127] Lampman, S.R. (technical editor) *Weld Integrity and Performance.* USA: ASM International, 1997.

[128] Řípa, M. et al. *Instalace tokamaku COMPASS v Praze.* Československý Časopis pro Fyziku, 58, 200-207, 2008.

[129] Pánek, R. et al. *Status of the COMPASS Tokamak and Characterization of the First H-mode.* Plasma Physics and Controlled Fusion, 58, 014015, 2015.

[130] Abdullaev, S. *Construction of Mappings for Hamiltonian Systems and Their Applications.* Germany: Springer, 2006.

[131] Special Metals Corporation http://www.specialmetals.com/ [Online; accessed 07-January-2016].

[132] Zhang, Z. et al. *Properties of T/P92 Steel Weld Metals for Ultra Super Critical (USC) Power Plant.* Weld in the World, 52, 455, 2008.

[133] Great Carbon Co., Ltd. http://www.gcarbon.com.tw/ [Online; accessed 08-January-2016].

[134] Institute of Plasma Physcis of the Czech Academy of Science. http://ufp.avcr.cz/vedecka_struktura_ufp/tokamak/tokamak_compass/diagnostics/magneticka-diagnostika/ [Online; accessed 08-January-2016].

[135] COMPASS-D discharge database. http://logbook.tok.ipp.cas.cz/shot_data/6602_all_print.png [Online; accessed 08-January-2016].

[136] Jin-Ming, G. et al. *Properties of Plasma Radiation during Discharges with Improved Confinement on HL-2A Tokamak.* Chinese Physics B, 19, 115201, 2010.

[137] Ocean Optics. http://oceanoptics.com/product/hr2000-custom/ [Online; accessed 08-January-2016].

[138] NIST Atomic Spectra Database. http://www.nist.gov/pml/data/asd.cfm [Online; accessed 08-January-2016].

[139] Griem, H. *Plasma Spectroscopy.* USA: McGraw-Hill Book Company, 1964.

[140] Hagelaar, G.J. et al. *Modelling of Tokamak Glow Discharge Cleaning I: Physical Principles.* Plasma Physics and Controlled Fusion, 57, 25008-25021, 2.

[141] Tafalla, D. and Tabarés, F.L. *First Boronization of the TJ-II Stellarator.* Vacuum, 67, 393-397, 2002.

[142] Dimitrova, M. et al. *Power Flux Density in the Divertor Region of the COMPASS Tokamak in Ohmic ELMy H-modes.* In compilation phase.

Attachments

Attachments can be found on the CD provided together with the hardcopy od this document. Content of the CD consists of one single folder, entitled ATTACHMENTS (Master thesis, VK), in which the following files can be found:

- POST-IRRADIATION_GRAIN_SIZE.pdf (Sec. 2.5.1)
- OPTICAL_METALLOGRAPHY.pdf (Sec. 2.5.2)
- SEM_METALLOGRAPHY.pdf (Sec. 2.5.2)
- FIB_6-A.avi (Sec. 2.5.3)
- FIB_6-B.avi (Sec. 2.5.3)
- LATTICE_DEFECTS.pdf (Sec. 2.5.4)
- CROSS-SECTIONAL_METALLOGRAPHY.pdf (Sec. 2.5.5)
- DISCHARGE_6604.avi (Sec. 3.3.2)